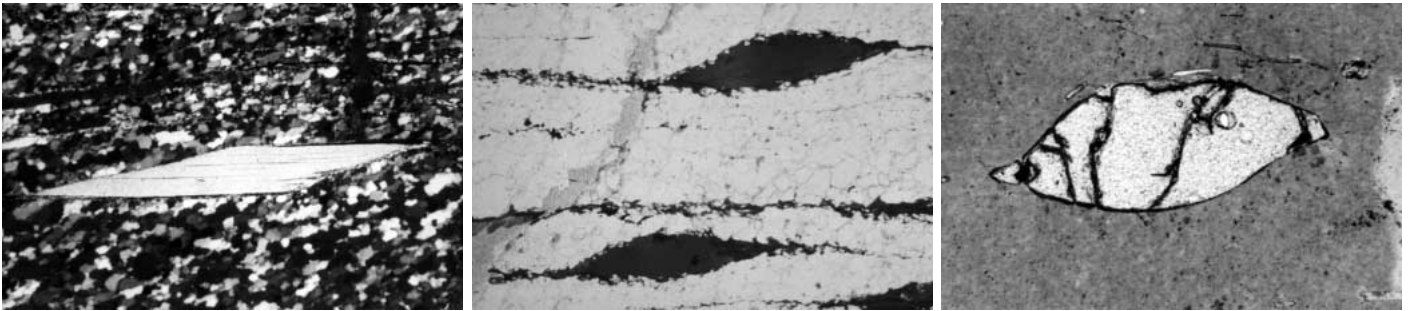


# Mica fish in mylonites

deformation mechanisms and implications for rheology



Saskia ten Grotenhuis



# **Mica fish in mylonites**

## **deformation mechanisms and implications for rheology**

Dissertation zur Erlangung des Grades  
"Doktor der Naturwissenschaften"

am Fachbereich Geowissenschaften  
der Johannes Gutenberg-Universität in Mainz

Saskia Martine ten Grotenhuis  
geboren in Warnsveld

Mainz, Dezember 2000

Erklärung:

Ich versichere hiermit die vorliegende Arbeit selbstständig und nur unter der Verwendung der angegebenen Quellen und Hilfsmittel verfaßt zu haben.

Mainz, Dezember 2000

Jahr der Prüfung: 2001



'De problemen, ..., scholen niet in wat er gebeurde,  
want dat was eenvoudig wat er gebeurde,  
maar hoe datgene wat er gebeurde denkbaar was.'

Uit: De ontdekking van de hemel, Harry Mulisch.

Voor Quintijn



## Abstract

Mylonites are foliated and usually also lineated rocks, that show evidence for strong ductile deformation. The deformation of mylonitic rocks with mica fish is investigated in this thesis. Mica fish are lenticular or parallelogram-shaped single mica crystals, that are often used as shear sense indicators. Tools for establishment of the shear sense are the stair-stepping of tails of the mica fish, their asymmetrical shape, and their orientation with respect to the mylonitic foliation. The aim of this thesis is to determine the mechanisms responsible for the development of mica fish and related structures, and to investigate what these structures indicate about strain distribution and rheology of mylonitic rocks.

The microstructures of natural mica fish in thin sections are described in Chapter 2. Possible mechanisms for the evolution of these mica fish are determined from the microstructures. The mica fish are also compared with other minerals showing similar structures. Possible mechanisms for the evolution of mica- and other 'mineral' fish are divided into two groups: mechanisms changing the shape of a single crystal and mechanisms to split a crystal into several parts. The first group of mechanisms include intracrystalline deformation, rigid body rotation, bending and folding, dynamic recrystallisation at the rim of the crystal, and pressure solution accompanied by local growth of the crystal. The mechanisms responsible for the shape of a mineral fish depend on the physical properties of the mineral. For some minerals the fish-shape seems to be developed during a certain stage of their evolution, before the crystal is destroyed by one of the grain size reducing mechanisms. Splitting the crystal into smaller parts is possible where a microfault is developed parallel to the basal planes of the fish, followed by sliding of the parts past each other, or when a mica fish is folded, and broken apart along the fold hinge, again followed by sliding of the two parts past each other. These mechanisms are based on inhomogeneous strain distribution in the matrix. A mica fragment can only be transported along a host clast if a micro-shear zone is developed along its grain boundary. The fish-shaped structures in the different minerals have their asymmetrical shape and their orientation with respect to the foliation in common. These characteristics make them all excellent shear sense indicators.

A new apparatus for deformation of rock analogues is presented in Chapter 3. Different flow types, varying from pure shear to simple shear and everything between them can be modelled with this apparatus. Suitable materials for deformation are so-called rock analogues. These materials have similar characteristics as rocks at high temperature and pressure, but are softer. This means that experiments can be performed in a relatively short time. Polymers are an example of a commonly used rock analogue. The rheology of polymers, which can be used in combination with the deformation apparatus in Chapter 3, is described in Chapter 4. The use of polymers as rock analogues is also discussed.

Analogue experiments to study the preferred orientation of the mica fish, using the apparatus described in Chapter 3, are presented in Chapter 5. Two different matrix materials are used: PDMS, a homogeneous Newtonian viscous polymer, and tapioca pearls, a granular material with low cohesion and a Mohr-Coulomb rheology. Rigid fish-shaped objects are used. The rotation of the objects in PDMS is similar to theoretical rotation of ellipsoids with a similar aspect ratio in a Newtonian viscous fluid. The objects obtain a stable orientation in a matrix of tapioca pearls. The stable orientations of the objects in simple shear experiments with tapioca pearls are similar to the orientation of mica fish in natural mylonitic rocks. Deformation in tapioca pearls is not homogeneously distributed, but concentrated in discrete shear bands. These results suggest that strain is localised in mylonites.

Numerical experiments with the finite difference code FLAC are performed to study the effect of matrix rheology and of inhomogeneous matrix properties on strain distribution and rotation of rigid objects in simple shear. These experiments show that homogeneous power-law rheology cannot explain the preferred orientation of the mica fish. The stable orientation of mica fish is probably the result of strain localisation around the object and anisotropy in the matrix.

General conclusions, following from the results presented in this thesis, are given in Chapter 7. This chapter also contains suggestions for future research related to the subjects presented in this thesis.

# Contents

<b>Abstract</b>	<b>7</b>
<b>Chapter 1</b>	
<b>General introduction</b>	<b>11</b>
1.1 Introduction	11
1.2 Previous work	13
1.3 Remaining problems	18
1.4 Aims and methods	19
1.5 Published parts	20
<b>Chapter 2</b>	
<b>Evolution of mica fish in mylonitic rocks</b>	<b>21</b>
2.1 Introduction	21
2.2 Morphology of mica fish	22
2.3 Evolution of mica fish	25
2.4 Comparison to other minerals	30
2.5 Discussion and Conclusions	35
<b>Chapter 3</b>	
<b>A new apparatus for controlled general flow modeling of analog materials</b>	<b>37</b>
3.1 Introduction	37
3.2 Description of the apparatus	39
3.3 Experimental materials	42
3.4 Types of flow modeled by new apparatus	43
3.5 Flow tests and boundary conditions	45
3.6 Pilot experiments: rotation of mica fish in plane strain	48
3.7 Conclusions	51
<b>Chapter 4</b>	
<b>Are polymers suitable rock-analogs?</b>	<b>53</b>
4.1 Introduction	53
4.2 Structure and deformation of polymeric liquids	54
4.3 Rheological measurements	61
4.4 Implications for the use of polymers and related materials as rock analogs	68
4.5 Conclusions	68

**Chapter 5****The influence of strain localisation on the rotation behaviour of rigid objects in experimental shear zones**

5.1	Introduction	71
5.2	Measurements of natural samples	73
5.3	Experimental method	75
5.4	Results of the experiments	78
5.5	Discussion	85
5.6	Conclusions	87
5.7	Appendix A	87

**Chapter 6****Numerical modelling of simple shear flow around rigid objects in different matrix materials**

6.1	Introduction	89
6.2	Experimental method	91
6.3	Experimental results	94
6.4	Discussion	106
6.5	Conclusions	107

**Chapter 7****General conclusions and suggestions for future research**

7.1	General conclusions	109
7.2	Suggestions for future research	111

**Appendix: Deformation apparatus**

A1	General Introduction	113
A2	User Manual	115
A3	Technical specifications	118
A4	Used set-up for experiments	119

References	121
Zusammenfassung	127
Samenvatting	129
Acknowledgements	131
Curriculum vitae	133

# Chapter 1

## General introduction

### 1.1 Introduction

Mylonites are foliated and usually lineated rocks that show evidence for strong ductile deformation (Hobbs et al. 1976, Passchier and Trouw 1996). Mylonites develop in zones of intense non-coaxial deformation, called mylonite zones or shear zones. Deformation of the earth's crust is largely localised in faults and shear zones (White et al. 1980, Ramsay 1980, Passchier and Trouw 1996). Shear zones range from micrometer- to kilometre-scale, where they accommodate relative movement of tectonic units in orogenic belts. Shear zones are weaker than the surrounding rock and crustal deformation is believed to be largely determined by the rheology of shear zones (Sibson 1997, White et al. 1980, Holdsworth et al. 1997). Rocks in shear zones in the crust range from brittle fault gouges and cataclasites at shallow depths to ductile mylonites at deeper levels (Passchier and Trouw 1996).

Mylonites normally contain fabric elements with monoclinic shape symmetry, attributed to the monoclinic geometry of flow in ductile shear zones (Bell and Etheridge 1973, Hobbs et al. 1976, White et al. 1980, Hanmer and Passchier 1991, Passchier and Trouw 1996). A large range of microstructures can be preserved in these deformed rocks that can potentially be used to reconstruct parts of the deformation history of the rock. Porphyroclasts, remnants of resistant mineral grains, which are at least an order of magnitude larger than grains in the matrix, are common microstructures in mylonitic rocks. They can be important to determine shear sense in a mylonite zone, because of their usually asymmetric shape and stair-stepping, difference in elevation of wings or tails, on both sides of the porphyroclast (Passchier and Simpson 1986). The asymmetric shape of porphyroclasts can be determined by their own shape or by the shape of recrystallised mantles or strain shadows. Porphyroclasts develop because of a difference in rheology between the clast and the matrix material. Minerals forming porphyroclasts are relatively 'hard' compared to the minerals forming the matrix.

Mica fish, a special type of porphyroclasts, are single crystals of mica with a lenticular or parallelogram shape (Fig 1.1). They are common in mylonites derived from micaceous quartzites and granitoid rocks. Mica fish are frequently used to determine the sense of shear in a mylonite zone (Eisbacher 1970, Lister and Snoke 1984). The stair stepping of the trails of small mica fragments, which extend into the matrix from the tips of the fish, the orientation of the fish with respect to foliation and the shape of the mica fish have all been used as empirically reliable shear sense indicators (Fig. 1.2, Lister and Snoke 1984, Passchier and Trouw 1996). Nevertheless, little work has been done investigating how mica fish actually form, and which factors influence their development.

Once it is understood how a microstructure develops, the observed microstructure in a rock sample can be used as a source of information on deformation mechanisms, deformation regime and deformation history. Mica fish and related structures are a potential source of such information on deformation mechanisms active during mylonitisation, the rheological beha-

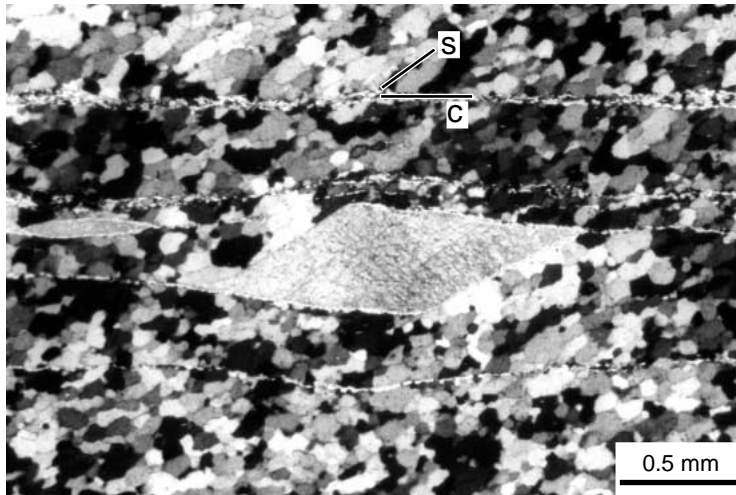


Figure 1.1. Photograph of mica fish from shear zone near Conceição do Rio Verde, Brazil, with crossed polarised light. Sense of shear is dextral. S and C indicate S-planes, defined by oblique foliation, and C-planes, defined by mica trails, according to Lister and Snoke (1984).

viour of the mylonitic rock and on the geometry of ductile flow. In this thesis mylonitic rocks containing mica fish and similar structures in other minerals are investigated in order to improve our understanding of this microstructure. The formation of mica fish and related structures, the strain distribution in the matrix around mica fish, and the preferred orientation of mica fish have been studied with field observations, analogue experiments, and numerical modelling, and results are presented in this thesis.

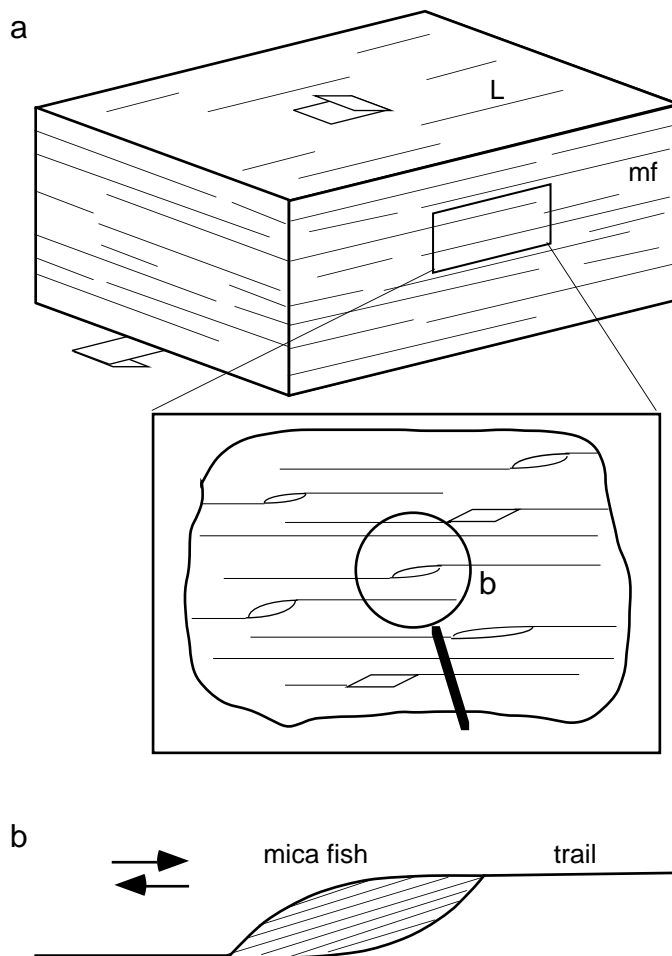


Figure 1.2. (a) Schematic diagram showing the geometry of a mylonite zone and how thin sections are cut to observe shear sense indicators; mf = mylonitic foliation, L = lineation. (b) Schematic drawing of mica fish with trails.



## 1.2 Previous work

### 1.2.1 Previous work on mica fish

Although frequently used as kinematic indicators, the development of mica fish and related structures has been relatively unexplored. Eisbacher (1970) was the first to describe mica fish and has shown that the shape of lenticular muscovite crystals and the orientation of their cleavage planes with respect to the foliation can be used to deduce the shear sense in mylonitic rocks. Lister and Snoke (1984) described mylonites containing mica fish and classified these rocks as a special type of S-C mylonite (Berthé et al. 1979). The C-surfaces, shear zone parallel displacement discontinuities or zones of relatively high shear strain, are defined by trails of fine grained mica between mica fish (Fig. 1.1). The S-surfaces are defined by oblique foliations in the adjacent quartz aggregates, formed as a result of dynamic recrystallisation (Law et al. 1984, Lister and Snoke 1984). According to Lister and Snoke (1984) mica fish form as a result of boudinage of pre-existing large mica grains by a combination of brittle and crystal-plastic processes. Recrystallisation processes initiated at the boundaries of the fish are also considered important for the formation of mica fish. According to Passchier and Trouw (1996) possible deformation mechanisms for mica fish are slip on the basal plane, rigid body rotation, boudinage, and recrystallisation at the edges. They also report that other minerals, such as kyanite and feldspar, can show similar fish-shaped structures. Asymmetrical fish shapes are also described for garnet (Ji and Martingole 1994, Azor et al. 1997), aggregates of fine-grained leucoxene (Oliver and Goodge 1996) and quartz in a calcite matrix (Bestmann 1999).

### 1.2.2 Analytical work on porphyroclasts in non-coaxial flow

Porphyroclasts develop because they are relatively hard compared to the matrix in which they are embedded. The matrix material of mylonitic rocks is usually considered to be an isotropic material deforming plastically, according to a 'power-law' flow law with an exponent between 1 and 3 (Poirier 1985). Therefore, the work on flow kinematics of mylonitic rocks and analysis of rigid body rotation of porphyroclasts in a deforming continuum follows the viscous fluid mechanics studies of flow behaviour of fluids around obstacles. Jeffery (1922) analysed the motion of rigid ellipsoidal particles immersed in a viscous shearing fluid with infinitely low Reynolds number in simple shear. His results show that the rotation rate of a particle is a function of the shape and orientation of the particle, and the shear strain rate of the fluid. Solutions for pure shear flow and plane strain general flow are given by Gay (1968) and Ghosh and Ramberg (1976), respectively. The angular velocity ( $\dot{\phi}$ ) of an object in plane strain general flow is given by:

$$\dot{\phi} = \frac{\dot{\gamma}(R^2 \sin^2 \phi + \cos^2 \phi) + \frac{1}{2} \sqrt{\frac{1}{W_k^2} - 1} (R^2 - 1) \sin 2\phi}{R^2 + 1} \quad (1.1)$$

(after Ghosh and Ramberg 1976), where  $\dot{\gamma}$  is strain rate,  $R$  is the aspect ratio of the object in the plane of deformation,  $\phi$  is orientation of the object, and using  $W_k$ , the vorticity number of flow (Means et al. 1980). According to this equation for the motion of rigid bodies, all objects, except lines and planes, are continuously rotating in simple shear flow. Objects rotate clockwise in dextral flow (Fig 1.3a). The angular velocity (in rad/s) of a sphere or cylinder is equal to half the shear strain rate in simple shear flow. Elongated objects have a pulsating rotation

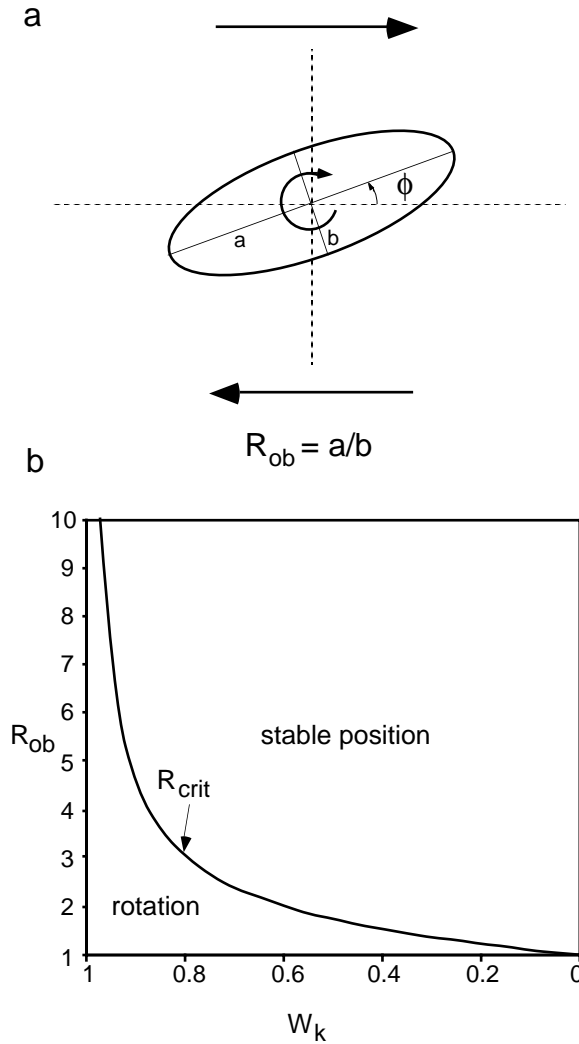


Figure 1.3. (a) Drawing showing the rotation direction of a rigid object in dextral simple shear and the sign convention for the orientation of the object used in this thesis. (b) Critical object aspect ratio ( $R_{crit}$ ) as a function of the vorticity number ( $W_k$ ) of flow. The plot indicates which objects will continuously rotate and which will go towards a stable orientation during progressive deformation.

rate under these conditions. All objects rotate towards a stable orientation during ongoing deformation in pure shear. In plane strain general flow, ( $0 < W_k < 1$ ) the combination of flow type and aspect ratio of the particle determine whether an object will keep rotating or reaches a stable position. Ghosh and Ramberg (1976) defined a critical aspect ratio ( $R_{crit}$ ):

$$R_{crit} = \sqrt{(1 + W_k)/(1 - W_k)} \quad (1.2)$$

This is the smallest possible aspect ratio for an object that will reach a stable orientation during continuous deformation with a given vorticity number ( $W_k$ ) (Fig 1.3b). For example, in flow with  $W_k = 0.8$  all objects with an aspect ratio  $\geq 3$  will eventually reach a stable orientation.

The work of Jeffery (1922) also includes equations that describe the surrounding velocity field in the matrix. Bretherton (1962) defined a two dimensional stream function that describes the flow field in shear flow around a cylinder. His solutions are based on the first inner expansion of the Stokes equation. This stream function is also applicable to cylinders that rotate with an arbitrary angular velocity. Robertson and Acrivos (1970), using the approach of Bretherton (1962) showed that the flow pattern around a cylinder is a function of the rotation rate of the cylinder. A free floating cylinder gives rise to a 'eye-shaped' flow geometry, and a small externally imposed reduction of the rotation rate results in a 'bow-tie-shaped' flow pattern (Passchier

et al. 1993, Fig. 1.4). Chwang and Wu (1975) used the singularity method, based on single point disturbances to find solutions for the Stokes equation. This method can be used to solve problems with difficult geometries in three dimensions. For a cylinder in shear flow the solutions of Bretherton (1962) and Chwang and Wu (1975) are equivalent. Jezek et al. (1999) found an efficient way to compute the equations of Jeffery (1922) that describe the velocity field around an object. They used these equations to develop a computer program, which shows the velocity field around rotating porphyroclasts and also around growing porphyroblasts in any homogeneous flow that can be described by the velocity gradient tensor.

The analytical solutions are used by several workers to analyse the vorticity and finite strain in rocks by using the orientation of porphyroclasts. Passchier (1987) used the critical aspect ratio described above to determine the vorticity number of flow by studying the orientation of porphyroclasts with different aspect ratios. Wallis (1995) and Beam and Fischer (1999) used the absolute rotation of porphyroblasts to determine the vorticity number and finite strain in shear zones. Masuda et al. (1995) produced distribution plots of porphyroclast aspect ratio versus orientation of initially random orientated objects based on the analytical solution for different flow regimes and different amounts of strain. These plots were compared with plots orientation versus aspect ratio of porphyroclasts from natural examples to determine vorticity and amount of strain of these samples.

### 1.2.3 Analogue experiments related to porphyroclasts.

In analogue experiments with rigid particles different materials have been used as analogue for the matrix, such as: silicon putty (e.g. Ghosh and Ramberg 1976, Ildefonse et al. 1992), honey with titanium oxide (Fernandez et al. 1983), paraffin wax (Ildefonse and Mancktelow 1993) and OCP, polyacrylamide (pAA) solution and glycerine (ten Brink 1996). Either pure or simple shear was usually modelled in these experiments and rectangular objects were used. The results from these experiments for single objects in a deforming matrix are mostly very similar and closely resemble behaviour predicted for elliptical particles by the analytical solutions mentioned above, indicating that the non-ellipticity of the object has only minor influence on the rotation rate. Experimental work on elongated objects with a non-coherent boundary between particle and matrix (Ildefonse and Mancktelow 1993) and with a non-Newtonian anisotropic viscous matrix material (pAA solution, ten Brink 1996) shows results that differ from the analytical solutions. Decoupled objects rotate slower in simple shear and faster in pure shear, compared to analytical solutions. Experiments by ten Brink (1996) with pAA solution

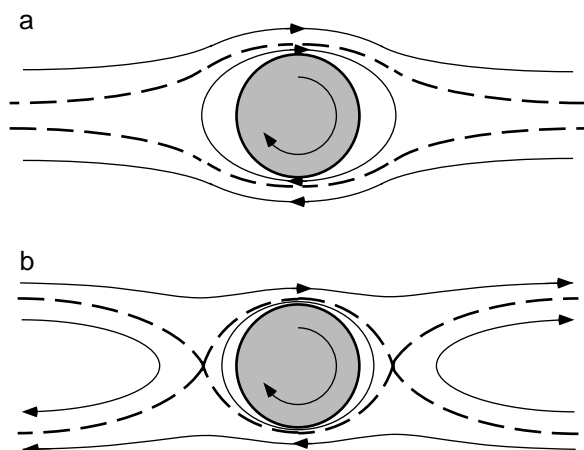


Figure 1.4. Schematic representation of (a) an 'eye-shaped', and (b) a 'bow-tie-shaped' flow geometry. Grey circle represents a rigid object, dashed lines separatrices, and continuous lines stream lines.

also show lower rotation rates in simple shear compared to experiments with a Newtonian matrix material. Experiments with interacting objects (Ildefonse et al. 1992, Ildefonse and Mancktelow, 1993) show that the rotation of individual objects is influenced if the distance between the objects is less than one particle length.

#### *1.2.4 Numerical modelling of flow around rigid objects*

Flow around rigid circular particles and the development of inclusion patterns have also been considered in numerical modelling. The development of inclusion patterns in porphyroblasts depending on initial orientation of the foliation with respect to the flow plane was studied by Masuda & Mochizuki (1989) with a hydrodynamical model. Ten Brink (1996) and Bons et al. (1997) investigated the flow perturbation around rigid objects under different boundary conditions and in different matrix materials with finite element modelling. Ten Brink (1996) also studied the effect of a slow or not rotating object on the flow pattern. Pennachioni et al. (2000) studied the effect of an incoherent particle matrix boundary with finite element modelling. These numerical models show that depending on the conditions during deformation a 'eye-shaped' or 'bow-tie-shaped' flow pattern develops around a rigid circular object. An 'eye-shaped' flow pattern only develops when simple shear boundary conditions are imposed at infinity from the object. Rigid boundaries of the model, reduced rotation of the object, or an incoherent particle matrix boundary lead to a 'bow-tie-shaped' flow pattern. The use of these models is mainly to interpret inclusion patterns in porphyroblasts and winged structures, such as sigma and delta clasts in deformed rocks.

#### *1.2.5 Strain partitioning and rotation of objects*

A contrasting theory on the behaviour of rigid objects in a shear zone is presented by Bell (1985). According to this theory non-coaxial deformation involving a component of bulk shortening does not deform homogeneously, but partitions into zones of nearly coaxial progressive deformation and zones of generally non-coaxial progressive shearing. Simple shear flow partitions into zones without deformation and zones of non-coaxial progressive shearing (Fig 1.5). Porphyroblasts or other rigid objects will be situated in the zones with coaxial deformation or without deformation and do not rotate during progressive deformation (e.g. Bell et al. 1992) with respect to the flow plane. This theory is based on strain field diagrams that duplicate geometries observed in and around porphyroblasts (Ramsay 1962, Bell 1981, 1985, Bell et al. 1992).

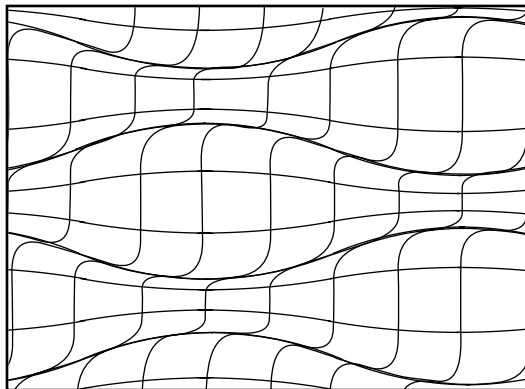


*Figure 1.5. Model for simple shear deformation in a shear zone after Bell (1985). Deformation is partitioned into zones with high strain and zones without strain.*

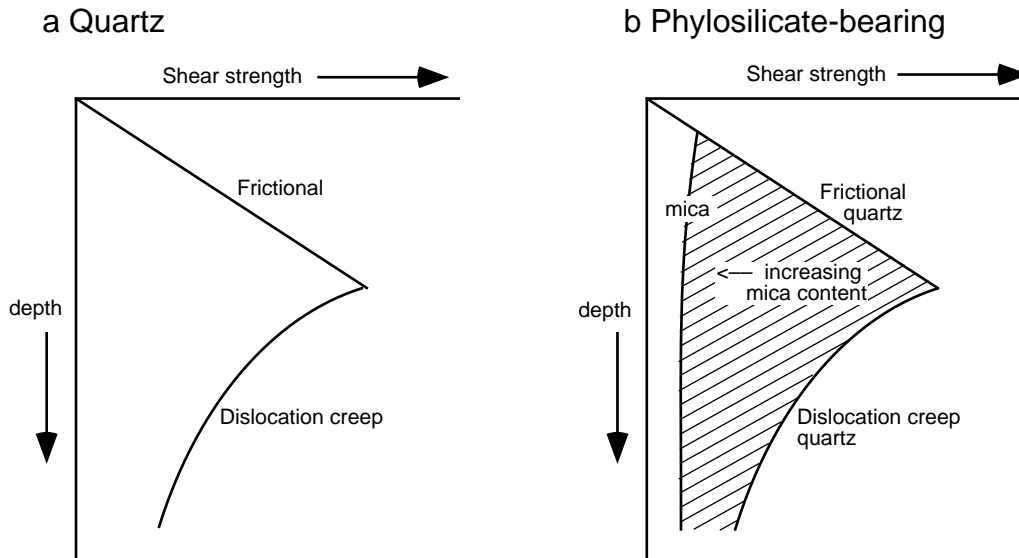


Figure 1.6. Crustal strength as a function of depth, for (a) quartzo-feldspatic crust, at shallow depths the strength is determined by brittle or frictional behaviour, at deeper levels by dislocation creep, and for (b) phyllosilicate bearing rocks; upper boundary same as in (a), lower boundary extrapolated from deformation of a single muscovite crystal (Mares and Kronenberg 1993). Figure after Imber et al. (1997)

### 1.2.6 Rheology of mylonites

The results from analogue and numerical modelling related to the behaviour of porphyroclasts in mylonites indicate that the rotation behaviour of the clast and the flow patterns around it depend on the behaviour of the matrix material. The dominant behaviour of fault rocks in the crust changes from brittle or frictional behaviour at shallow depths, less than 10 to 20 kilometres, to dislocation creep or ductile behaviour at deeper levels. This transition is illustrated with a crustal strength profile (Fig 1.6a). Ductile deformation in mylonites is usually described with viscous flow laws based on data from experimental rock deformation (Poirier 1985, Kirby and Kronenberg 1987). The data from experiments can be used to determine which mechanisms are expected to be dominant under particular conditions. For polymineralic mylonites it is more difficult to describe their rheological behaviour. Different models based on the rheology of the components, their volume fractions and their geometrical distribution have been proposed (Jordan 1988, Bons 1993, Handy et al. 1999). Imber et al. (1997) presented a crustal strength profile for phyllosilicate bearing rocks, where the upper limit is determined by frictional behaviour and dislocation creep of phyllosilicate free rocks and the lower boundary by the extrapolated data for deformation of a single muscovite crystal, oriented favourably for slip (Fig 1.6b). In these two-phase models a small fraction of a second phase, which is usually the case for mica in a mylonitic quartzite with mica fish, does not have a significant influence on the bulk rheological behaviour.

### 1.3 Remaining problems

A couple of problems related to porphyroclasts in mylonitic rocks are remaining. For example only few experiments in 3D or in a crystalline material are performed, and the effect of non-homogeneous flow on the rotation of porphyroclasts is not known.

Mica fish are a special type of porphyroclasts with a specific shape and orientation. The problems studied in this thesis are related to: (1) formation of mica fish and related structures, (2) strain distribution in matrix around mica fish, and (3) the preferred orientation of mica fish.

The mechanisms responsible for the formation of mica fish have been discussed by Lister and Snoke (1984) and Passchier and Trouw (1996). Lister and Snoke (1984) give boudinage of pre-existing large mica grains by a combination of brittle and crystal-plastic processes and recrystallisation processes as major mechanisms. According to Passchier and Trouw (1996) mica fish are formed by slip on the basal plane, rigid body rotation, boudinage, and recrystallisation at the edges. The importance of each mechanism is not discussed. A comparison between mica fish and fish-shaped structures formed by other minerals and the mechanisms responsible for the formation of these structures is lacking. The reliability of mica fish as shear sense indicators has been discussed (Eisbacher 1970, Lister and Snoke 1984, Passchier and Trouw, 1996), but it is not known if the other minerals with a lenticular or parallelogram shape also form reliable shear sense indicators.

The trails of mica between boudinaged mica fish may indicate strain localisation on these trails, as suggested by Lister and Snoke (1984). However, the quartz in the matrix does not show a change in crystallographic or shape preferred orientation, or in grain size towards these trails, which would indicate a gradient in finite strain in the matrix. In fact, the matrix fabric is homogeneous and suggests homogeneous flow.

The preferred orientation of the mica fish seems to be contradicting with the studies of the behaviour of rigid object in simple shear viscous flow, where all objects except lines or planes are continuously rotating. Rigid objects can have a stable orientation in a viscous fluid in general flow, but their orientation is different than the orientation found for mica fish (Section 1.2, Fig. 1.7). Analytical, analogue and numerical models show that several factors are influencing the rotational behaviour of rigid objects, such as the vorticity number of flow, the shape of the object, the rheology of the matrix and coherence between object and matrix. The factors determining the preferred orientation of the mica fish are not clear.

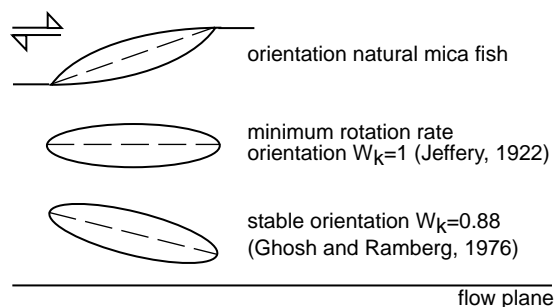


*Figure 1.7. Comparison between orientation of mica fish in mylonites and rigid ellipsoidal objects in simple shear and general flow, according to the analytical solutions for the motion of rigid objects in a viscous fluid (Jeffery 1922, Ghosh and Ramberg 1976).*

## 1.4 Aims and methods

In this thesis the evolution of mica fish and related structures in mylonitic rocks is investigated in order to determine which processes contributed to the development of these structures and what these structures tell us about the flow kinematics, deformation mechanisms and rheology of the rock. The aims of this thesis are: (a) to determine the mechanisms responsible for evolution of mica fish and similar structures, (b) to investigate which factors influence the orientation of these structures, and (c) to discuss the implications of the results for rheology of mylonitic rocks.

To achieve this, the following methods were used: investigation of natural mylonitic rocks with mica fish and related structures, analogue modelling on the behaviour of fish-shaped rigid objects in experimental shear zones and numerical experiments on the behaviour of relatively rigid objects in different matrix materials.

Field examples of mica fish and other minerals with similar structures were studied in thin sections (Chapter 2). The morphology of the structures and their orientation with respect to the mylonitic foliation is described and possible mechanisms that were active during deformation were determined. Similarly shaped structures in other minerals were compared with the mica fish in order to determine whether the same or different mechanisms play a role. Also the reliability of these structures as kinematic indicators is discussed.

Information deduced from thin sections is limited, because small scale structures can be interpreted in different ways and evidence for deformation mechanisms may be destroyed by progressive deformation and recrystallisation. Therefore, fish-shaped structures were studied in analogue experiments, where the evolution of structures during progressive deformation was followed. A new apparatus to model general flow of analogue materials, developed together with Sandra Piazzolo, is presented in Chapter 3. This apparatus can model homogeneous deformation in general flow regimes, i.e. combinations of pure and simple shear. In Chapter 4 the deformation behaviour of polymers is explained. A thorough knowledge of the rheologic properties of the materials used in experiments is necessary for the correct interpretation of the experimental results. Among the possible materials are several polymeric liquids. Properties of several polymers and polymer mixtures, which can be used with the apparatus described in Chapter 3, were investigated and subsequently described in detail. The use of polymers as rock-analogues is also discussed. Chapter 3 and 4 have been written in close collaboration with Sandra Piazzolo (University of Mainz) and T. Pakula (Max Planck institute for polymer research, Mainz) is a co-author on Chapter 4.

Analogue experiments with fish-shaped structures in two different matrix materials are described in Chapter 5. The first matrix material was PDMS, a homogeneous Newtonian viscous material, and the second was tapioca pearls, a granular material with a Mohr-Coulomb rheology. Rigid objects made of India rubber were used as an analogue for the mica fish. The results of these experiments were compared with the results from the thin sections study.

In Chapter 6 numerical experiments with the computer code FLAC are presented. With these experiments, the effect of matrix rheology on strain distribution and rotation of a rigid object in the matrix was studied in more detail. Not only the matrix rheology, but also the effect of inhomogeneous matrix properties, of the boundary conditions and of slip along the object matrix boundary on strain distribution and rotation of the object were studied.

The results of the study of the thin sections, the analogue modelling and the numerical modelling are discussed together in Chapter 7. Implications of the results for crustal rheology are given as are suggestions for further work related to this subject.

### 1.5 Published parts

Parts of this thesis have been prepared for publication and are either in press or review. These parts have been included in this thesis unaltered, with the exception that the layout and figure numbers have been brought in line with the rest of the thesis. Published parts are:

Piazolo, S., Ten Grotenhuis, S.M. and Passchier, C.W. 2000 (in press). A New Apparatus for controlled General Flow Modeling of Analog Materials. In: *Tectonic Modeling: A Volume in Honor of Hans Ramberg*, by Hemin A. Koyi, Neil S. Mancktelow, eds. Geological Society of America Memoir 193. (chapter 3)

Ten Grotenhuis, S.M., Piazolo, S., Pakula, T. Passchier, C.W. and Bons, P.D. (in review) Are polymers suitable rock-analogs? *Journal of Geophysical Research, Solid Earth*. (chapter 4)

Ten Grotenhuis, S.M., Passchier, C.W. and Bons, P.D. (in review). The influence of strain localisation on the rotation behaviour of rigid objects in experimental shear zones. *Journal of Structural Geology* (chapter 5)

Parts of this research have been presented at international conferences. Abstracts of these presentations are:

S.M. ten Grotenhuis, R.A.J. Trouw and C.W. Passchier. 2000. Evolution of mica fish in mylonitic rocks. Swiss Tectonic Studies Group Meeting 2000, Zuerich.

S. M. ten Grotenhuis and C. W. Passchier. 2000. Rotational behaviour of rigid objects in homogeneous monoclinic flow. *Geoscience 2000*, Manchester.

S.M. ten Grotenhuis, R.A.J. Trouw and C.W. Passchier. 2000. Evolution of "mica fish" and similar structures in other minerals in mylonitic rocks. 31<sup>st</sup> IGC, Rio de Janeiro.

Saskia M. ten Grotenhuis and Cees W. Passchier, 1999, Mica Fish and Other Fish-shaped Shear Sense Indicators. *EUG 10*, Strasbourg. *Journal of Conference Abstracts. Terra abstracts EUG 10* p 828.

Saskia M. ten Grotenhuis and Cees W. Passchier 1999 Analogue experiments of "mineral-fish". *Deformation Mechanisms, Rheology, Microstructures*, Neustadt.



## Chapter 2

# Evolution of mica fish in mylonitic rocks

### Abstract

Mica fish are asymmetric microstructures in mylonites which can be used as shear sense indicators. This chapter presents a morphological subdivision of mica fish, based on shape and internal cleavage orientation. Using this subdivision and other morphological aspects the relative importance of the following possible formation mechanisms is estimated: intracrystalline deformation, rigid body rotation, grain size reduction either by recrystallisation or by peeling off of fragments from larger grains, and pressure solution accompanied by local growth. Although microboudinage seems a likely process for the break down of large fish into smaller ones, evidence in the form of microfolds and kinks indicates that many fish suffer shortening rather than extension along their long axes. Evidence is presented for an alternative process in which tips of mica fish are isoclinally folded and then break off along the hinge. Mica fish-like structures also occur in other minerals, including tourmaline, feldspar, garnet, hypersthene and quartz. For each of these minerals the relative importance of the formation mechanisms mentioned above is evaluated based on morphological aspects.

### 2.1 Introduction

Mylonites are rocks that develop dominantly by strong ductile deformation, usually in zones of intense non-coaxial flow known as mylonite zones (Bell and Etheridge 1973). Many mylonites contain porphyroclasts with a larger grain size than the matrix material. Porphyroclasts develop because they are more resistant to deformation and dynamic recrystallisation than the matrix. During deformation these porphyroclasts can develop into sense-of-shear markers, such as sigma and delta clasts (Hanmer 1984; Passchier and Simpson 1986) and mica fish (Eisbacher 1970; Lister and Snoke 1984). Mica fish are lozenge- or lens-shaped mica crystals usually accompanied by trails consisting of small mica fragments. Frequently, these trails show stair-stepping; they are parallel to each other, but offset across the mica fish. Mica fish are relatively common in mylonitised gneisses and in mylonites derived from micaceous quartzites (Eisbacher 1970; Lister and Snoke 1984). According to Lister and Snoke (1984), quartzites with mica fish are a special type of S-C mylonite, a structural setting in which two foliations are developed; C-surfaces related to displacement discontinuities and S-surfaces related to the accumulation of finite strain (Berthe et al. 1979). In quartz-mica rocks, Lister and Snoke (1984) define the C-surfaces as trails of mica fragments forming the mylonitic foliation; each C-plane is believed to be the result of microscopically thin displacement discontinuities. The S-surface is defined by oblique foliation of quartz in the matrix, characterised by the grain shape preferred orientation. This oblique foliation is formed when the matrix is dynamically

recrystallised during deformation (Means 1981). According to Lister and Snoke (1984), the mica fish in these rocks result from micro-boudinage of pre-existing large (white) mica grains by brittle and crystal-plastic processes. Mica fish have shown empirically to be reliable shear sense indicators, because of their asymmetrical shape and stair stepping of the trails. Although the importance of mica fish has been widely recognised (e.g. Eisbacher 1970, Simpson and Schmid 1983, Lister and Snoke 1984, Passchier and Trouw 1996), their genesis and kinematic significance have remained relatively unexplored, with the exception of the work of Lister and Snoke (1984).

Although the mechanism of mica-fish development as proposed by Lister and Snoke (1984) is possible, we decided to study a different dataset to see if it is the only possible solution. The shape of approximately 1500 muscovite fish was established in 28 thin sections from a single outcrop. It is thought that in this large number of samples it will be possible to see intermediate stages of active processes in the development of mica fish. Mapping of these intermediate stages can help to determine to what extent each process was active. Fish-shaped structures are most common for white mica, but have also been described for some other minerals, e.g. asymmetrical aggregates of fine-grained leucosene (Oliver and Goodge 1996), garnets with asymmetrical shapes (Azor et al. 1997) and asymmetric quartz grains in a calcite matrix (Bestmann 1999). We found that several other minerals can have a fish-shape including biotite, feldspars, quartz, garnet, hypersthene and tourmaline. In this chapter these structures are described and compared to the structures observed in white mica fish. Seventy-five thin sections from other locations with fish-shaped structures in other minerals were studied. The morphological characteristics of muscovite fish are compared to the fish-shaped structures in these minerals, in order to determine whether the deformation processes, like intracrystalline deformation, rigid body rotation, recrystallisation and pressure solution, that contributed to the development of these structures, acted in similar proportions or not. Finally, the reliability of all fish-shaped structures as kinematic indicators is discussed. In this chapter we attempt to relate deformation mechanisms to the observed microstructures, although this is obviously interpretative. Experimental work related to the development of mica fish, to control some of the mechanisms suggested here, is in progress.

## **2.2 Morphology of mica fish**

The studied samples of muscovite fish come from an outcrop along the highway that links the cities of Caxambu and Cambuquira, approximately 5 km south of Conceição do Rio Verde, Southern Minas Gerais State, Brazil (Fig. 2.1). The quartzites containing the mica fish belong to the lower unit of the Neoproterozoic Andrelândia Depositional Sequence (Trouw et al. 1983, Paciullo et al. 1993, Ribeiro et al. 1995) that consists of banded gneisses with intercalated quartzites and schists. The outcrop is situated in an ENE trending subvertical dextral shear zone of about 500 m thickness. The metamorphic grade during deformation is estimated as upper greenschist facies, according to the metamorphic mineral association biotite + chlorite + garnet + muscovite + quartz, apparently stable during mylonitisation.

The mica fish usually have a flake or disc-shape in three dimensions, in some cases bent or folded (Fig. 2.2). In the plane parallel to the foliation they are only slightly elongated in the direction of the stretching lineation. The length of the longest axis of mica fish is up to 4 mm.

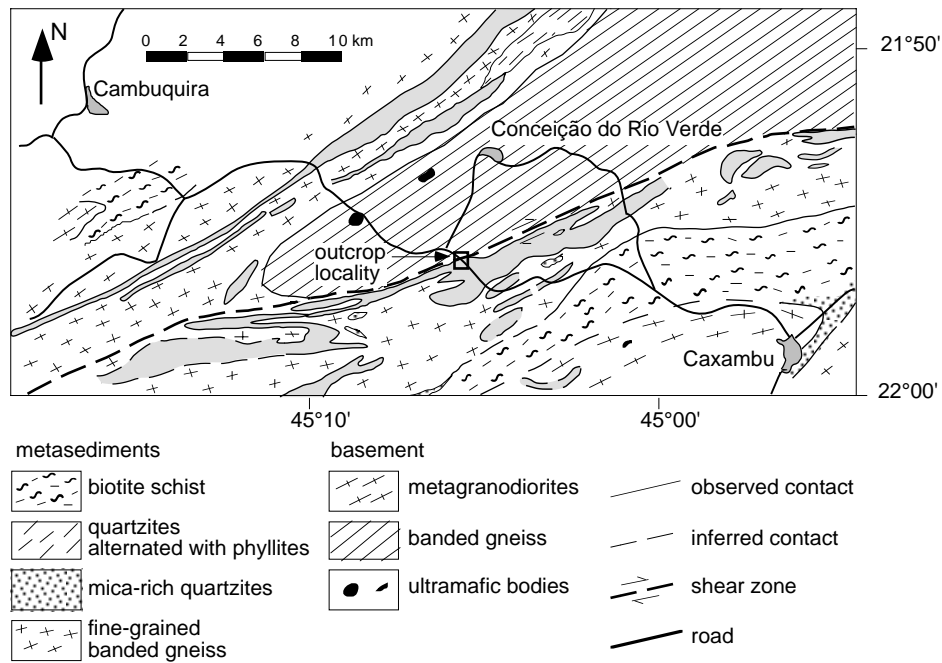


Figure 2.1. Geological map of the region between Cambuquira and Caxambu, Minas Gerais, Brazil, modified after Trouw et al. (1983). Locality of the outcrop of the studied mica fish is indicated on the map

In the plane parallel to the stretching lineation and perpendicular to the foliation the mica fish are elongated and the average aspect ratio of 400 measured mica fish is 5.7. The matrix surrounding the mica fish consists of fine-grained quartz with an oblique foliation, which makes an average angle of  $34^\circ$  with the mylonitic foliation. Trails of very small mica fragments extend from the tips of the mica fish into the matrix (Fig. 2.2). These 10-100  $\mu\text{m}$  wide trails define the mylonitic foliation. They usually show very clear 'stair-stepping' (Lister and Snoke 1984, Passchier et al. 1993, Passchier and Trouw 1996) over each mica fish. Mica fish are inclined to the mylonitic foliation in the same direction as the oblique foliation. The angle between the long axes of 400 measured mica fish and the mylonitic foliation has a mean value of  $13^\circ$  (Fig. 2.3a), whereas the angle between the basal plane (001) and the mylonitic foliation has a mean value of  $11^\circ$  (Fig. 2.3b).

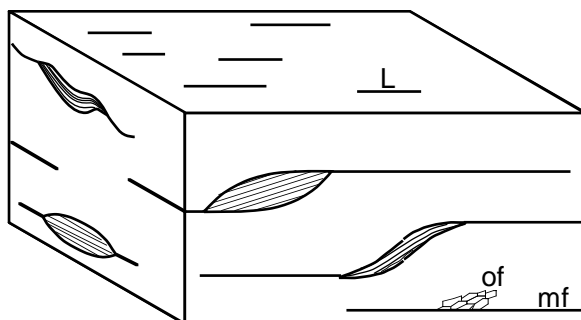


Figure 2.2. Schematic drawing of mica fish in relationship with mylonitic foliation (mf), oblique foliation (of) and stretching lineation (L).

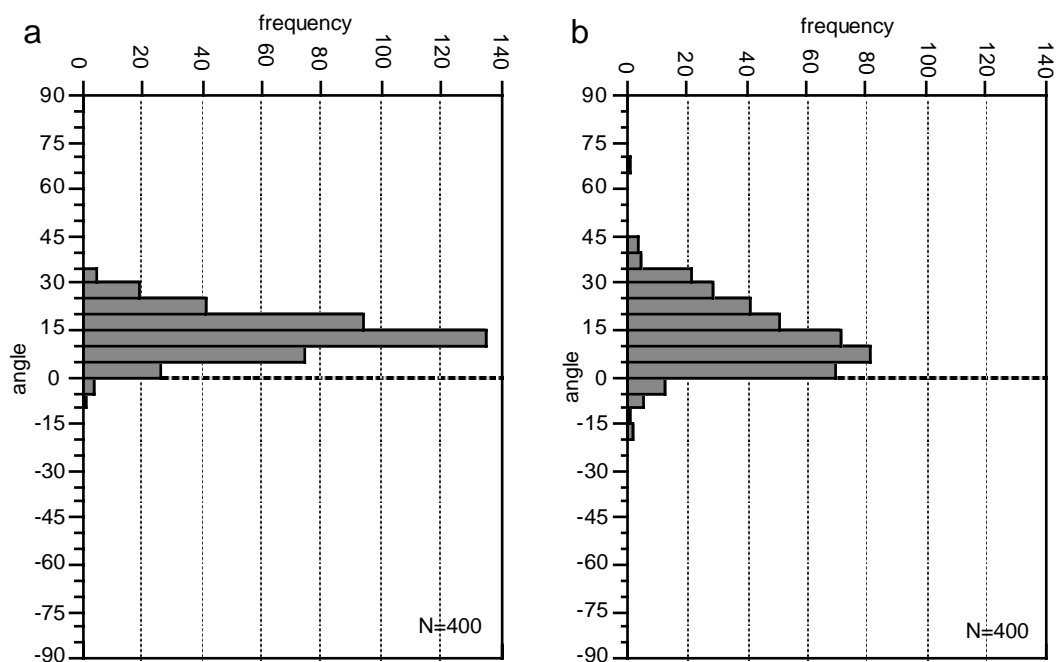


Figure 2.3. Orientation of the long axes (a) and (001) planes (b) with respect to the mylonitic foliation of 400 mica fish.

The morphology of mica fish as seen in thin sections cut parallel to the lineation and perpendicular to the foliation permits a subdivision into several groups based on their shape and the orientation of the lattice planes. Most common is a lenticular shape (Fig. 2.4a, 2.5a) with curved sides, usually ending in sharp tips: 33% of the mica fish belong to this group. The orientation of the lattice planes is usually parallel or at a small angle to the long axes of these fish. In some of the lenticular shaped fish the lattice planes converge on an internal discontinuity at one or both tips (Fig. 2.4b, 2.5b). Also common are mica fish with their tips bent over in the direction of the mylonitic foliation (19%, Fig. 2.4c). The lattice planes of these fish are typically curved at the tips. Fish with a parallelogram shape form another group, sides of these fish are straight compared to the lenticular ones. The longest side of this type of fish is typically subparallel to the mylonitic foliation. Lattice planes are usually parallel to this side (25%, Fig. 2.4d, 5c). Less common are mica fish with a parallelogram shape in which lattice planes are parallel to the short side (8%, Fig. 2.4e, 2.5d). The corners forming the tips of these fish are sharp, whereas the other corners are usually rounded. The next group, representing 5% of the mica fish, are thick lenses (Fig. 2.4f, 2.5e). The orientation of the lattice planes is usually steeper than the long axes of the fish in this group. The sides of the mica fish of this type are typically smoothly curved. The difference between this group and the lenticular mica fish is that the trails of fine-grained mica are not on the same line as the upper and lower parts of the central mica fish, but curved towards the points (Fig. 2.4f). The last group, representing 5% of the mica fish, consists of elongate thin micas. The average aspect ratio of this type is 9.7. They are usually orientated with their long axes parallel or at a small angle to the mylonitic foliation,

but with their lattice planes dipping in the opposite direction to the oblique foliation of quartz, and sometimes also a slight stair-stepping in the opposite direction. Therefore, these thin micas, if considered separately, could lead to an erroneous shear sense determination (Fig. 2.4g, 2.5f). Lattice planes make a small angle with the long axes of these fish. Most of the mica fish can be placed in one of these groups, but transitions between the different shapes are also observed and some fish shapes (about 5%) do not fit in any of the groups.

### 2.3 Evolution of mica fish

Mica fish are porphyroclasts and, as such, are derived from pre-existing grains by some deformation mechanism. We consider the main mechanisms to play a role during the formation of mica fish the following: internal deformation, especially shear on (001) basal planes; rigid body rotation; bending and folding of mica grains; grain size reduction either by dynamic recrystallisation at the rims or the peeling off of small fragments; and pressure solution accompanied by local growth.

Mares and Kronenberg (1993) carried out experiments on shortening of single mica grains.

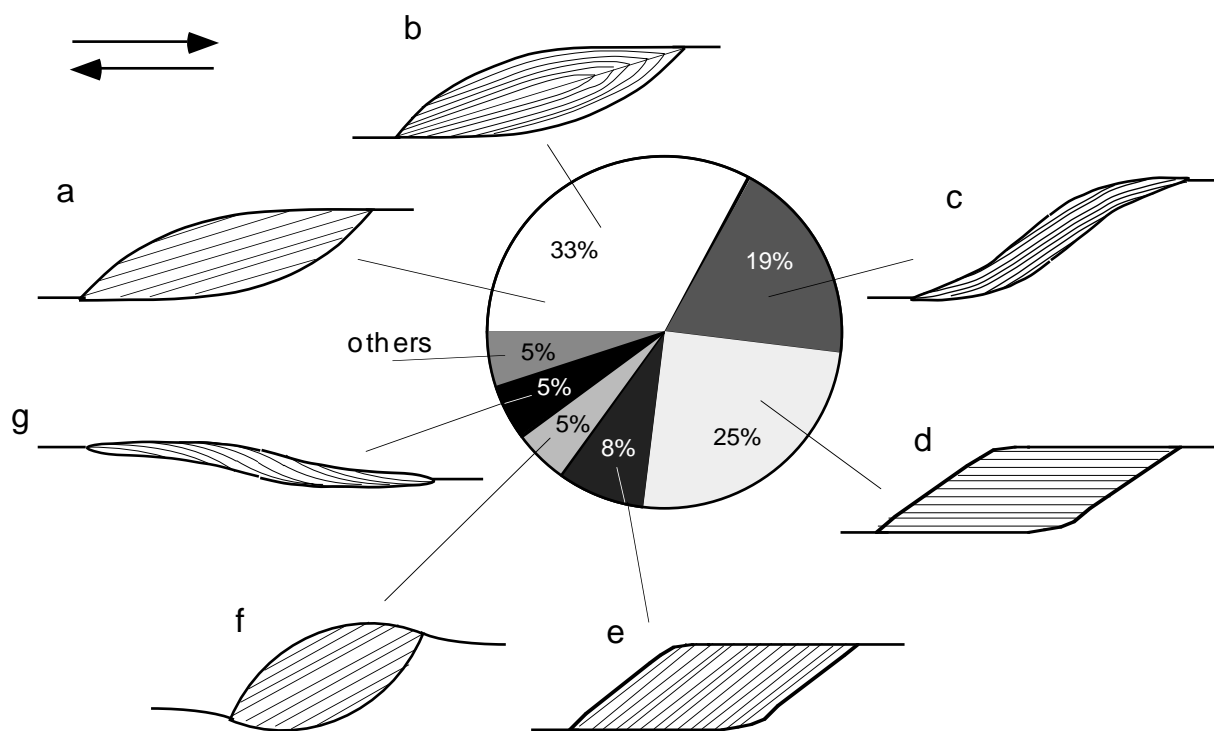
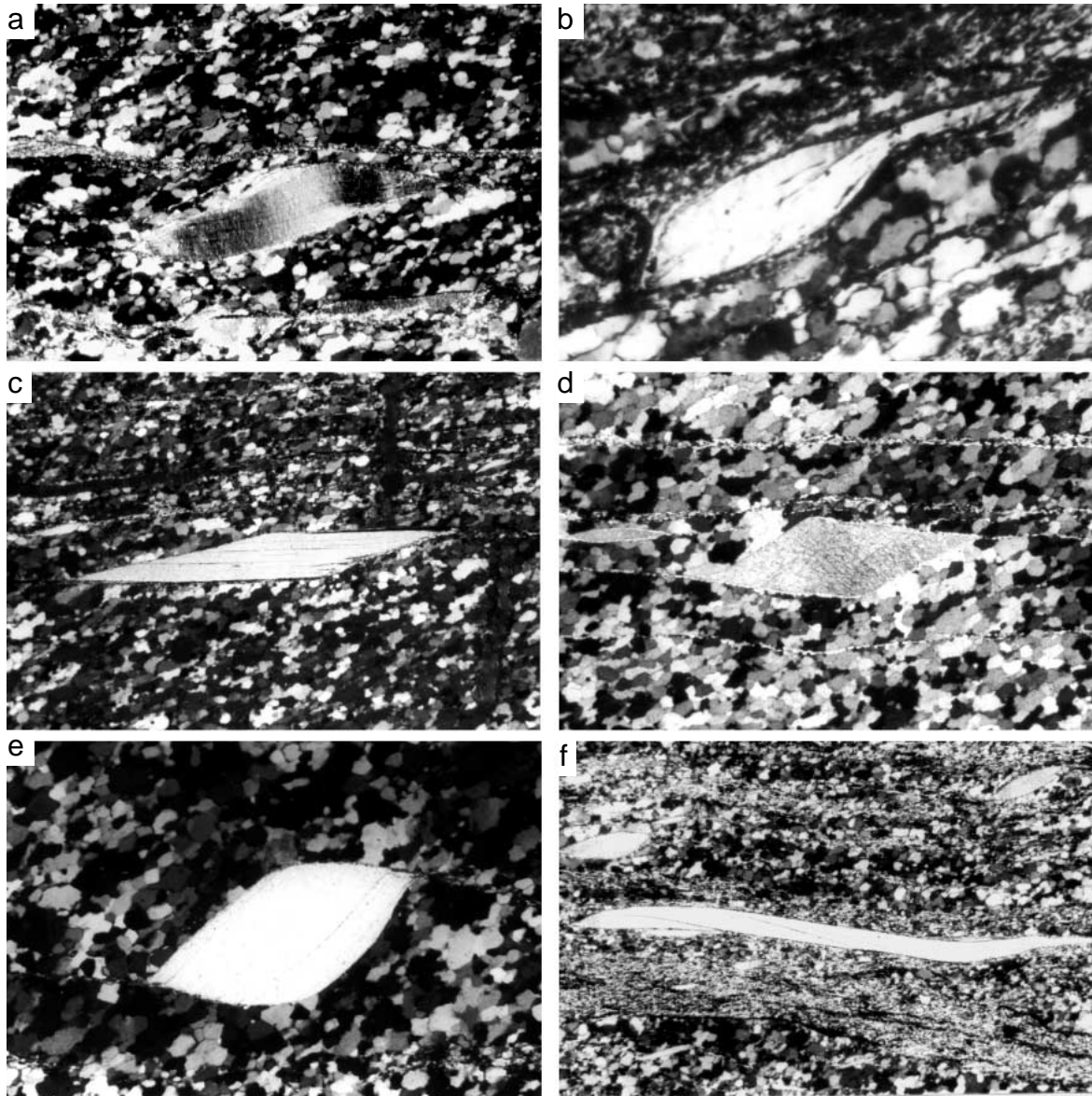


Figure 2.4. Schematic drawings of the different morphological types of mica fish. (a) Lenticular mica fish; (b) lenticular fish with internal fault plane where part of the mica is dissolved; (c) lenticular fish with points inclined in the direction of the foliation; (d) parallelogram shaped fish with (001) parallel to longest side of the fish; (e) parallelogram shaped fish with (001) parallel to the shortest side of the fish; (f) fish with small aspect ratio and curved tails; (g) mica fish with high aspect ratio and inverted stair stepping; if considered out of their context, this structure could lead to an erroneous shear sense determination.

They have shown that due to their mechanical anisotropy, muscovite single crystals deform by several mechanisms depending on the orientation of the cleavage planes. In their experiments the deformation was either accomplished by dislocation glide, where the crystals were shortened at  $45^\circ$  to (001), by kinkbands where shortening was parallel to (001) or by fracturing where the crystals were shortened at  $90^\circ$  to (001). Shear on (001) by dislocation glide is apparently an important deformation mechanism in muscovite, but the effect of this mechanism



*Figure 2.5. Photographs of different types of mica fish. (a) lenticular mica fish with slightly inclined tips showing undulose extinction. (b) lenticular fish with internal fault plane in the right tip of the fish. (c) parallelogram shaped fish with (001) parallel to longest side of the fish, (d) parallelogram shaped fish with (001) parallel to the shortest side of the fish, (e) fish with small aspect ratio (f) mica fish with high aspect ratio. Samples are from Conceição do Rio Verde, Brazil. Shear sense in all photographs is dextral. Width of view (a) 3 mm, (b) 0.75 mm, (c), (d) and (e) 3 mm, (f) 6 mm. Crossed polars.*

depends on the orientation of the cleavage planes with respect to the shortening direction and on the critical resolved shear stress. In non-coaxial flow, the sense of movement can be antithetic or synthetic. This phenomenon has been described for grains transected by microfaults (Etchecopar 1977; Simpson and Schmid 1983; Passchier and Trouw 1996) and may work in the same way for shear on (001) in mica crystals. In mica fish with cleavage planes parallel to the mylonitic foliation (Fig. 2.4d) shear strain on (001) is synthetic and for mica fish with cleavage planes at a high angle to the foliation (Fig. 2.4e) the shear strain may be antithetic. For mica fish with cleavage planes at small to moderate angles to the foliation this mechanism will have minor or no influence on the shape of the mica fish, because the critical resolved shear stress is not likely to be exceeded. The relative importance of this mechanism in our studied material is therefore estimated to be approximately proportional to the percentage of parallelogram shaped fish (Fig. 2.4d, e) which is 33%.

The relative importance of the second mechanism, rigid body rotation can be estimated from their orientation. All mica fish are orientated with their long axes between  $-8$  and  $32^\circ$  with the mylonitic foliation (Fig. 2.3a). Similar orientations are observed for mica fish from other localities (Eisbacher 1970, Lister and Snoke 1984). Analytical studies of rotating elliptical rigid objects in a homogeneous Newtonian viscous matrix do not predict a stable position for particles in progressive simple shear (Jeffery 1922, Ghosh and Ramberg 1976). Masuda et al. (1995) studied distribution patterns of the longest axes of initially randomly distributed elliptical particles in general plane strain flow according to the equations given by Ghosh and Ramberg (1976). These patterns show that in simple shear there is a concentration of the orientation of the long axes, depending on the amount of strain. However, none of the patterns given for simple shear or combinations of pure and simple shear as given by Masuda et al. (1995) is similar to the distribution pattern of the measured mica fish. We therefore suggest that this small variety in the orientation of the mica fish indicates that this orientation represents a stable or semi-stable position in the process of progressive non-coaxial flow. It is likely that the mica fish are rotated towards their current position during the first stages of the deformation history. After that the rotation rate is apparently decreased to such an extent that most fish remain in approximately the same position for the remainder of the deformation history. Explanations for the stable or semi-stable position of the mica fish in natural examples could be that the matrix does not behave as a Newtonian viscous material, or that strain is not distributed homogeneously through the matrix. Another possibility is that the mica fish cannot be regarded as relatively rigid objects and internal deformation of the fish influences their orientation.

The importance of bending and folding of mica fish (Lister and Snoke 1984, their Fig. 5i,j) can be judged from their common undulatory extinction (Fig. 2.5a). One out of five mica fish is of the type with bent tips (Fig. 2.4c) and mica fish with isoclinally folded tips are relatively common (5%). Kink folds were observed in some mica fish with their lattice planes orientated sub-parallel to the mylonitic foliation. These structures indicative of shortening are probably generated when the basal planes of the fish rotate locally into the compressional quadrant of the flow.

The importance of grain size reduction can be estimated from the large number of small mica grains that are formed by dynamic recrystallisation at the tips and sides of the mica fish. Recrystallisation of muscovite is the result of rotation of small parts at the boundary of the fish. Growth of these parts results in small new mica grains (Lister and Snoke 1984). These new

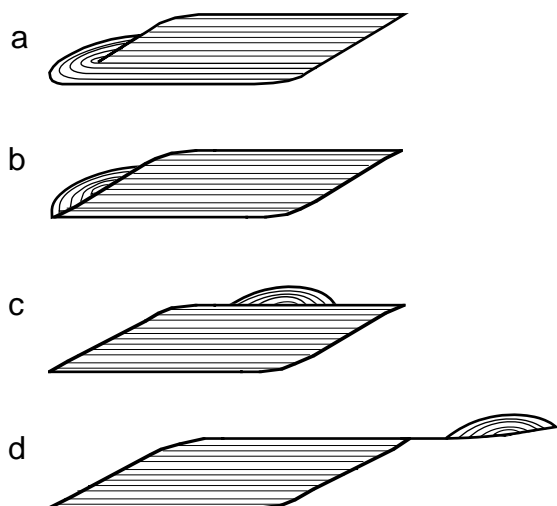


Figure 2.6. Schematic drawing of mica fish illustrating a proposed process in which a crystal is divided into two parts. (a) The point of the crystal is folded; (b) the fold becomes very tight and the fish breaks apart along the fold hinge; (c) the smaller part is transported along the side of the bigger part, (d) two separate mica fish have formed.

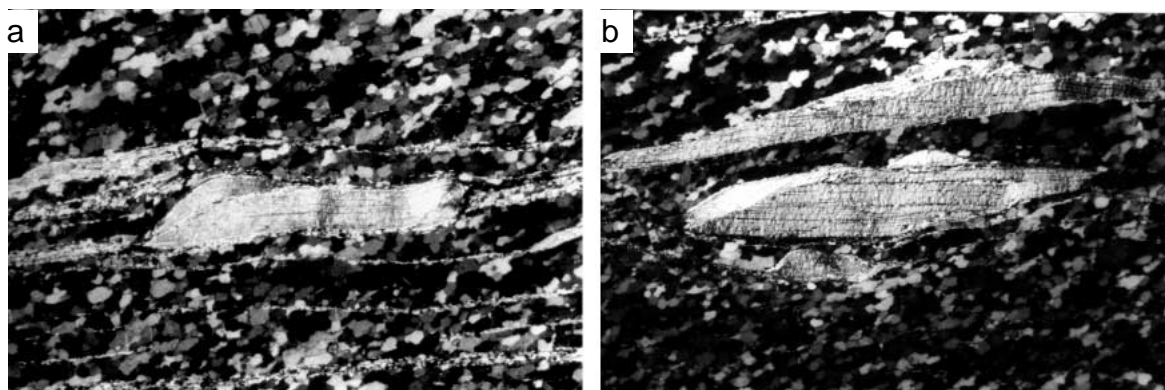


Figure 2.7. Photographs showing different stages of the process proposed in Figure 5. (a) Iso-clinal folds both on the right and left-hand side of this mica fish show the first stage of the process. (b) Lower mica fish shows isoclinal fold with tight fold hinge on the left-hand side; on top of the mica fish is a small mica grain, which can be interpreted as a fragment broken off from the tip and now being transported along the grain. Samples are from Conceição do Rio Verde, Brazil. Shear sense in both photographs is dextral. Width of view (a) and (b) 3 mm. Crossed polars.

grains are subsequently torn into the matrix by intense ductile deformation to form the trails that define the mylonitic foliation. The amount of small recrystallised grains is high at the sides of the mica fish that have a significant angle with the (001) planes (Fig. 2.5c) indicating that this grain size reduction mechanism is most intense at these sides. This mechanism can also contribute to the development of the fish shape of the mica grains by rounding the corners of the crystal. According to Lister and Snoke (1984) the convergence of lattice planes on a discontinuity in the tips of some mica fish (Fig. 2.4b, 2.5b) is also due to a recrystallisation mechanism. They suggest that rotation of the cleavage planes towards parallelism with the boundary, followed by migration recrystallisation, leads to the formation of a recrystallisation front, which is observed as a discontinuity in the crystal. An attempt was made to detect possible cut-off effects by erosion of zoned grains, with the help of microprobe analysis. However,



all analysed mica fish proved extremely homogeneous in composition, not showing any zoning pattern. The relative importance of pressure solution accompanied by local growth in the formation of mica fish could not be assessed for the same reason.

Apart from the one-to-one formation of mica fish from isolated crystals there is also microstructural evidence for mechanisms where one big crystal is divided into several smaller ones. Lister and Snoke (1984) drew attention to several microstructures related to the peeling off of smaller fish from large ones. At first sight boudinage seems to be the most logical mechanism to explain these structures, because the majority of the mica fish lie with their long axes in the extensional quadrant of the deformation. Direct evidence of boudinage in the form of two pieces that can be linked together does occur, but is not common in our samples. An alternative mechanism for the peeling off of smaller mica fish is demonstrated in Figure 2.6. In this process the tips of the fish are folded and separated from the parent crystal along tightly bent fold hinges, following the axial plane. The small separated part is subsequently thrust over the larger part. Structures that can be interpreted to represent several stages of this process occur

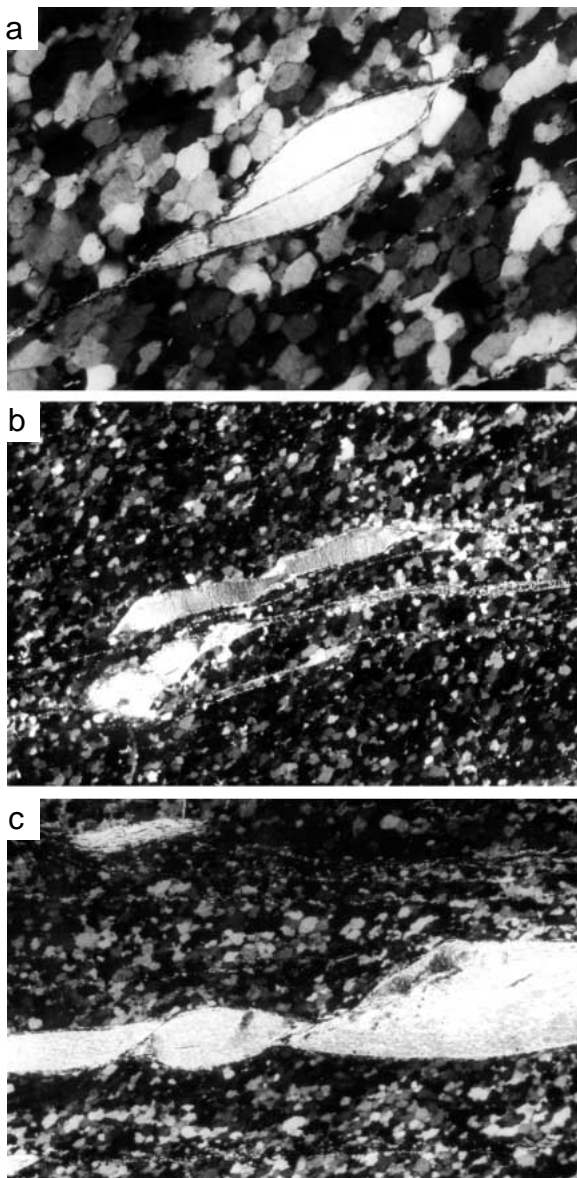


*Figure 2.8. Photographs of micro-faults separating mica fish in two or more smaller parts. (a) and (b) different stages of a process in which a mica fish is divided in two parts along basal planes with synthetic sense of movement. (c) Micro-faults through a mica fish at a high angle to the basal planes, showing antithetic movement. All samples are from Conceição do Rio Verde, Brazil. Shear sense in all photographs is dextral. Width of view (a) 1.5 mm, (b) 6 mm, (c) 3 mm. Crossed polars.*

with considerable frequency in our studied material (Fig. 2.7). Another mechanism to split a mica fish in two parts presented by Lister and Snoke (1984) is the development of fractures parallel to the basal plane of mica (Fig. 2.8). This process is similar to the earlier described shear along the cleavage planes, except that shear strain is now accommodated by brittle behaviour resulting in movement along a fracture. Depending on the orientation of the cleavage planes in the mica grain this may result in antithetic or synthetic micro-faults. Indications for this mechanism are also commonly observed in our material, especially in fish with basal planes subparallel to the mylonitic foliation. Micro-faults through the mica fish both at low and high angles to the basal planes were also occasionally observed, showing synthetic or antithetic movement depending on the orientation of the fault (Fig. 2.8c). Evidence for a mechanism explained by Lister and Snoke (1984) where a smaller fish is separated from his parent by an antithetic listric fault (their Fig. 7) was not observed in our material.

It can be concluded that mica fish form by rigid body rotation, principally in the early stages, accompanied by shear on basal planes, some bending and folding, and 'tectonic erosion' along the rims mainly due to recrystallisation and possibly pressure solution and local growth. The relative importance of each mechanism in a single crystal depends on its shape and orientation with respect to the foliation and on metamorphic grade, fluid pressure and composition, and strain rate.

## **2.4 Comparison to other minerals showing similar shapes**

Fish-shaped structures, comparable to the structures described for white mica, are also found in a number of other minerals. Previously studied minerals with an asymmetrical fish shape are: garnet (Ji and Martignole 1994; Azor et al. 1997), aggregates of fine-grained leucoxene (Oliver and Goodge 1996), and quartz in a calcite matrix (Bestmann 1999). The development of fish-shaped garnet will be described below, together with new observations of garnet fish. The leucoxene fish described by Oliver and Goodge (1996) are an alteration product of primary detrital constituents, rutile, ilmenite or titanite, in a siliciclastic protolith. Deformation of the initially equidimensional aggregates which are described as passive features in the quartz matrix results in an ellipsoid, whose long axis rotates towards the mylonitic foliation with increasing strain. The quartz grains described by Bestmann (1999) are detrital quartz grains surrounded by a calcite matrix. The evolution of the asymmetrical shape of these distortion-free quartz grains is explained by lattice diffusion creep.

We found that a fish shape is also developed in biotite, quartz, K-feldspar, garnet, hypersthene, and tourmaline. The most significant differences between the fish structures in these minerals as compared to muscovite fish, and the possible mechanisms by which they are formed are discussed below.

### *2.4.1 Biotite*

In our experience biotite fish are much less common than muscovite fish. The studied samples are mylonitized granodiorites from Palm canyon, Santa Rosa mylonite zone, California. The studied samples consist of quartz and biotite and minor amounts of plagioclase, K-feldspar and muscovite. The muscovite in these samples also shows fish-shapes. The samples are deformed under middle amphibolite conditions (Wenk and Pannetier, 1990, Goodwin and Wenk 1995). The biotite and muscovite fish from this location are lenticular in cross-sections parallel to the

stretching lineation and perpendicular to the foliation (Fig. 2.9a), similar to the lenticular white mica fish described above (Fig. 2.4a). Measurements of the angle between the long axes of 69 biotite fish and the mylonitic foliation give a mean value of  $12^\circ$  (Fig 2.10a) and measurements of 31 muscovite fish give a mean angle of  $15^\circ$ . Both angles are very similar to the median angle for white mica fish from Minas Gerais. Their morphology suggests that biotite fish are formed by the same mechanisms as suggested above for the muscovite fish: a combination of dislocation glide, dynamic recrystallisation at the rims and rigid body rotation. Compared to muscovite, biotite is more resistant to shear on (001) at experimental conditions (Mares and Kronenberg 1993). The recrystallisation mechanism in biotite and in muscovite is the same. Rotation of part of the fish leads to high angle boundaries and new grains (Etheridge and Hobbs 1974). The muscovite fish in the studied thin sections are surrounded by very small amounts of recrystallised material, compared to the amount of recrystallised material around the biotite fish. So, apparently, under similar circumstances, biotite recrystallises more readily than muscovite (Passchier 1985). This relative facility to recrystallise may account for the less frequent occurrence of biotite fish, as compared to muscovite fish.

#### 2.4.2 Tourmaline

Tourmaline fish were found in the Andrelândia Depositional Sequence (Paciullo et al., 1993; Ribeiro et al., 1995), near Lambari, Minas Gerais, Brazil. The metamorphic grade during deformation of these samples is middle amphibolite facies. The tourmaline fish usually have a parallelogram shape with straight sides and typically an angle of about  $50\text{--}55^\circ$  between the sides (Fig. 2.9b). They are orientated with their long side parallel to the mylonitic foliation. The long axes of 56 tourmaline fish were measured and give a median value of  $16^\circ$  (Fig 2.10b),

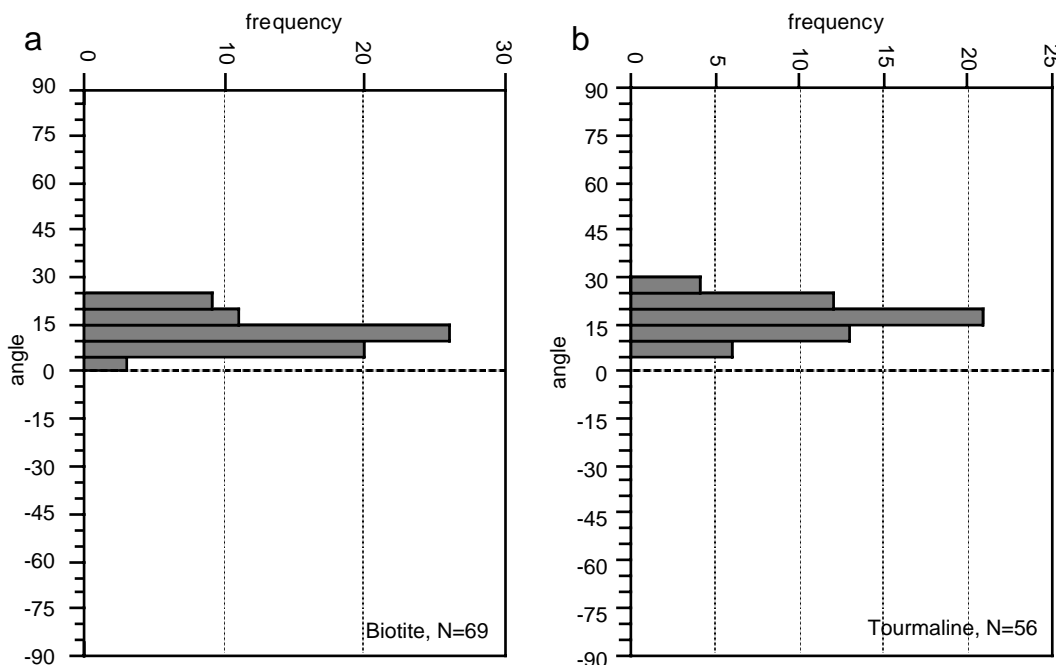


Figure 2.10. Orientation of the long axes with respect to the mylonitic foliation of (a) 69 biotite fish from the Santa Rosa mylonite zone, California and (b) 56 tourmaline fish from Lambari, Minas Gerais, Brazil.

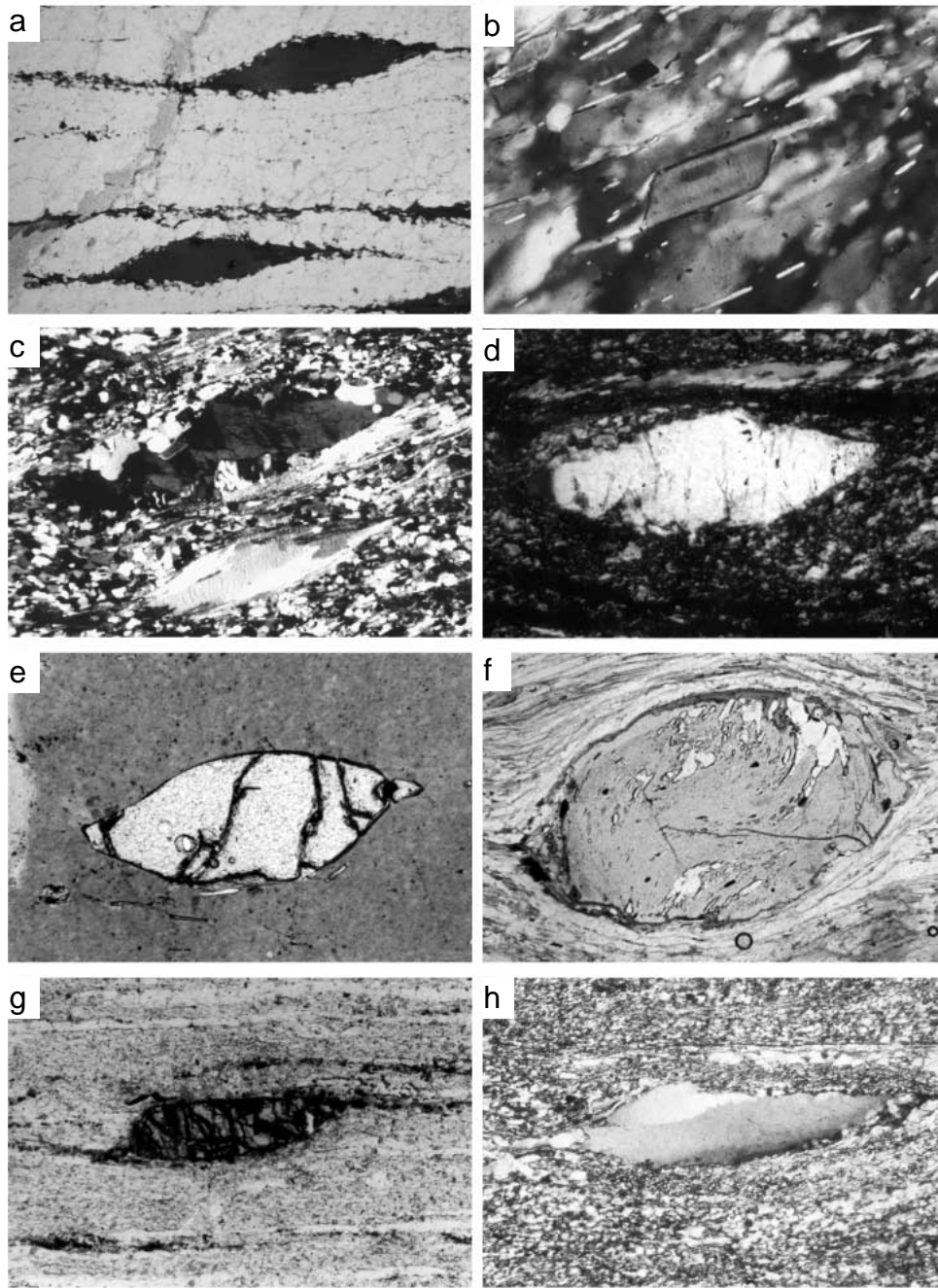
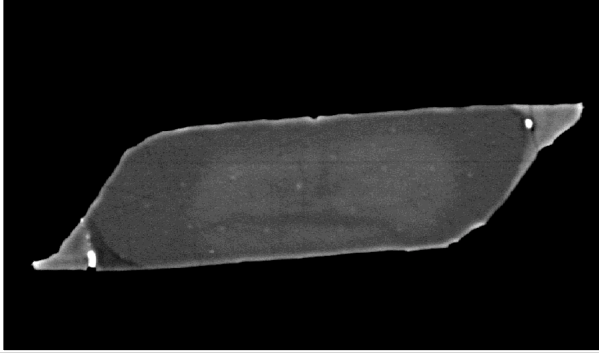


Figure 2.9. Photographs of different minerals showing fish shapes similar to mica fish. (a) Biotite fish with small recrystallised biotite grains along the rims from Santa Rosa Mylonite zone, California. (b) Small tourmaline fish showing parallelogram shape from Lambari, Brazil. Crossed polars. (c) K-feldspar fish with myrmekite along the high stress sides of the fish. Below the K-feldspar fish is a recrystallised mica fish. Sample from Espinhaço belt, Brazil. Crossed polars. (d) K-feldspar fish with subgrains along the rim from Roraima, Brazil. Crossed polars. (e) Garnet fish in static recrystallised quartz matrix from Morro Cara de Cão, Brazil. (f) Garnet fish in quartz-mica matrix with chlorite concentrated along upper and lower rims from Santana do Garambeu, Brazil. At the right-hand side of the fish straight crystal faces are preserved. (g) Hypersthene fish with trails of recrystallised material from Caparaó, Brazil. (h) Quartz fish in fine-grained matrix composed of quartz and mica with elongated subgrains from Serra do Espinhaço, Brazil. Crossed polars. Shear sense in all photographs is dextral. Width of view (a) 6 mm, (b) 1.5 mm, (c) 6 mm, (d) and (e) 1.5 mm, (f), (g) and (h) 3 mm.



*Figure 2.11. BSE image of tourmaline fish from Lambari, Brazil, showing zoning in the centre and indicating new growth of tourmaline at the tips of the fish. Width of view 140  $\mu\text{m}$ .*

which is similar to the median value for the measured muscovite and biotite fish. The studied tourmaline fish do not show evidence for internal deformation. Back scatter electron (BSE) images of the tourmaline fish show zoning in the tourmaline fish, which is often cut-off at the edges in the shortening quarters. The tips of the fish are usually a lot brighter, indicating a different composition than the remainder of the fish (Fig. 2.11). This suggests that the shape of the tourmaline fish is the result of dissolution at the edges in the shortening quarters of the fish and precipitation of tourmaline at the tips of the fish.

#### *2.4.3 K-feldspar*

Lenticular shaped K-feldspars have been described by Simpson and Wintsch (1989) from a S-C mylonite. The tips of these K-feldspar grains are recrystallised and quartz-plagioclase symplectite (myrmekite) is observed in shortening quarters in the rims of the crystals. The reaction from K-feldspar to plagioclase and quartz is favoured at sites of high normal stress, because it involves a volume decrease (Simpson and Wintsch 1989). K-feldspar fish used in this study come from Roraima, Brazil, and from the Espinhaço Belt, Diamantina, Minas Gerais, Brazil. The studied samples are deformed under lower amphibolite facies (Roraima) and upper greenschist (Espinhaço Belt) conditions. The K-feldspar fish from both localities usually have a disc-shape with subgrains and recrystallised new grains concentrated in the rim of the fish (Fig. 2.9c,d). Concentration of mica at the sides of the clasts suggests that pressure solution also played a role in the development of these fish. In the samples from the Espinhaço Belt the fish have myrmekite in shortening quarters in the rim of the crystal (Fig. 2.9c). It can be concluded that the mechanisms that contributed to the formation of K-feldspar fish are principally recovery and recrystallisation along the rims, accompanied by rigid body rotation and in some cases myrmekite formation. Internal deformation by dislocation glide is certainly less important as compared to the white micas, but dissolution may be more significant. These structures are more common in high grade mylonites, since the mechanisms for the formation of K-feldspar fish are enhanced at relatively high metamorphic temperatures.

#### *2.4.4 Garnet*

Fish-shaped garnets from a middle amphibolite shear zone were reported by Azor et al. (1997). Compositional X-ray maps of their samples show that the growth zoning is truncated along the borders of the garnets. Based on this fact they claim selective dissolution as the main mechanism responsible for the final shape of the garnets in their samples. Ji and Martignole (1994) studied elongated garnets in high grade rocks and suggested dislocation slip and recovery as

deformation mechanisms for their garnets, although Den Brok and Kruhl (1996) argued that these structures could also have been formed by grain boundary diffusional creep. The garnet fish studied here are from two high-grade, mylonitised pelitic metasediments, a granulite facies mylonite from Varginha, Minas Gerais, Brazil, and a high amphibolite-granulite mylonite from Morro Cara de Cão, Rio de Janeiro, Brazil (Fig. 2.9e). A third set of samples with garnet fish (Fig. 2.9f) is from a middle amphibolite facies garnet-staurolite schist from Santana do Garambeu, Minas Gerais, Brazil, with much white mica and biotite in the matrix. The garnet fish from the two high-grade mylonites have very similar structures, lenticular shapes, with pointed corners (Fig. 2.9e). In our samples the deformation mechanism in the garnets may involve internal deformation, selective dissolution or diffusional creep. The quartz matrix in these samples is statically recrystallised, so sense of shear cannot be determined from the matrix. The garnet fish are the only kinematic indicators in these rocks.

The garnet fish deformed under middle amphibolite facies conditions may initially have had ideomorphic crystal shapes, since in some garnet fish straight faces were found at the undeformed sides, with the appearance of crystal faces (Fig. 2.9f). The fish-shape of these grains is probably the result of a grain size reducing mechanism enhanced at sides of the crystal perpendicular to the principal shortening direction, combined with rigid body rotation of the fish-shaped structure towards a semi-stable position. The reduction of the grain size could be the result of a retrograde reaction, suggested by the concentration of chlorite at the rim of the garnet crystals in the shortening quarters.

#### 2.4.5 *Hypersthene*

Hypersthene fish were found in a granulite facies mylonite zone near Caparaó, Minas Gerais, Brazil. They typically show a disc-like shape with very clear stair stepping (Fig. 2.9g). Evidence for dynamic recrystallisation is found mainly at the rim of the crystal in the form of small fragments of hypersthene around the crystal and in trails extending from the tips of the fish into the matrix. Microprobe analysis proved the hypersthene to be very homogeneous in composition, without any detected zoning. The fish shape is probably developed by recrystallisation or mechanical erosion at the rim of the crystal, acting preferentially at the sides perpendicular to the shortening direction, combined with rigid body rotation.

#### 2.4.6 *Quartz*

Quartz fish are uncommon in mylonitic rocks, since quartz tends to constitute the matrix rather than porphyroclasts in most mylonites. The studied quartz fish are formed in low greenschist facies rocks of volcanic origin from Serra do Espinhaço, Minas Gerais, Brazil. The quartz phenocrysts in this sample are embedded in a fine-grained matrix consisting of mica and quartz. The quartz fish are elongated grains with undulose extinction and irregular boundaries (Fig. 2.9h). Elongated subgrains are observed and also domains with small recrystallised grains, mainly in the tips of the fish. Some domains of small recrystallised grains are subparallel to the long axes of the fish, separating them in two parts in a similar way as the microfaults in the white mica fish. The combination of large subgrains and domains of small recrystallised grains is a typical fabric of dynamic recrystallisation due to internal deformation in quartz. The undulose extinction indicates that the quartz grains are deformed by dislocation glide and climb. Recrystallisation in the tips of the fish tends to destroy the fish shape. The concentration of mica at the sides perpendicular to the shortening direction indicates that pressure solution also played a role in the formation of the fish shape.

## 2.5 Discussion and Conclusions

As shown above, fish-shaped structures develop in a number of different minerals in mylonitic rocks. Apart from the minerals discussed, fish-shapes were also observed in staurolite, amphibole, diopside, apatite, rutile, hematite, plagioclase and prehnite. Minerals showing fish-shapes have different crystal structures and a wide range of physical properties. All fish structures have in common that they are formed as porphyroclasts embedded in a matrix that underwent non-coaxial flow. All mineral fish can be used to infer the sense of shear in a zone of non-coaxial flow. Their asymmetrical, lenticular or parallelogram shape and the inclination of their long axes with respect to the mylonitic foliation makes them reliable kinematic indicators, which can be used even in samples where the matrix is statically recrystallised.

Detailed observations of the fish-shaped structures in different minerals indicate that different mechanisms predominated during the deformation of each mineral. Most minerals have in common that they are embedded in a matrix rich in quartz. The studied minerals are probably stronger than the quartz-rich matrix. At least for some of the minerals it seems that the fish-shape represents only a short stage in their evolution, before the grain is completely recrystallised (e.g. in the case of biotite), or destroyed by other grain size reducing mechanisms.

The ideas presented here and by Lister and Snoke (1984) about the separation of parts of mica fish are all based on inhomogeneous flow around these structures. The proposed transport of separated parts of the fish along the grain boundary of the host clast is only possible if there is a micro-shear zone along this boundary. With such micro-shear zones it is also possible to transport little recrystallised fragments of the fish far into the matrix, as observed for muscovite, biotite and hypersthene. The observed orientation distributions for muscovite, biotite and tourmaline fish indicate that they cannot have formed in homogeneous Newtonian flow. These observations imply that in rocks containing such structures the shear strain is partly accommodated in narrow zones. The fabric of mica fish with trails of fine grained mica extending from the tips of the fish into the matrix combined with the oblique foliation of the quartz in the matrix, show resemblance to mylonites with an S-C fabric as suggested by Lister and Snoke (1984). However, in the studied samples with fish-shaped structures in other minerals, in some cases the oblique foliation is destroyed by static recrystallisation (e.g. Fig. 2.9e), or the mylonitic foliation is not well developed (e.g. Fig. 2.9g). The fish-shape is very similar in all cases. Therefore, we believe that it is not useful to consider mylonites with fish-shaped structures as a type of S-C mylonite. Suggested mechanisms for the formation of mica fish and fish-shaped structures in other minerals are intracrystalline deformation, rigid body rotation, bending and folding, grain size reduction either by dynamic recrystallisation or by peeling off of small fragments, and pressure solution accompanied by local growth. The proportion in which each mechanism contributes to the microstructure is different for each mineral. A remaining problem is that the relative importance of these mechanisms cannot always be deduced from the microstructure.





## Chapter 3

# A new apparatus for controlled general flow modeling of analog materials

### Abstract

We present a new deformation apparatus to model homogeneous deformation in general flow regimes, in which all combinations of simple shear parallel to the xy-plane and pure shear parallel to the x-, y- and z-axes can be realized. With this apparatus it is possible to control the kinematic vorticity number of monoclinic flow during progressive deformation. The user defines the type of deformation by a set of parameters such as kinematic vorticity number, strain rate, and duration of the experiment. The apparatus consists of a set of mobile pistons on a low friction sole and is open at the top. All pistons are flexible to ensure homogeneity of deformation in a major part of the sample. The corners of the box are connected to four sliding carriages, which themselves are sliding on another set of four carriages positioned at right angles to the first set. This set-up and the controlled movement of the sliding carriages allow the user to model any type of monoclinic trans-tension and transpression. A computer program controls six stepping motors used to move the different carriages simultaneously and accurately. In the apparatus materials with a viscosity range of  $10^3$  to  $10^6$  Pa s can be used. A set of pilot experiments investigating the rotation of mica fish in different general regimes is presented as an example for the use of this apparatus.

### 3.1 Introduction

Research in recent years has shown that many shear zones cannot be explained with a simple shear model but that combinations of simple and pure shear are likely to represent the true character of flow in natural shear zones. Therefore, noncoaxial monoclinic and/or triclinic shear zones have been the focus of recent work including both analytical and numerical studies (e.g. Ghosh and Ramberg 1976, Sanderson and Marchini 1984, Weijermars 1991, 1993, 1997, Jezek et al. 1994, Robin and Cruden 1994, Jezek et al. 1996, Dewey et al. 1998 and reference therein, Fossen and Tikoff 1998, Passchier 1998), field studies (e. g. Druguet et al. 1997, Tikoff and Greene 1997, Krabbendam and Dewey 1998) and analog modeling (e.g. Giesekus 1962, Weijermars 1998, Cruden and Robin 1999, Griera and Carreras 1999). However, the effect of different flow geometries on the development of structural elements within and at the boundaries of shear zones is still unclear. Data from the field and field-derived samples are the most important source of information on shear zones. Nevertheless, small-scale structures in shear

zones can only be correctly interpreted if their development is modeled under controlled conditions. An important complementary tool to field data and analytical work is experimental rock deformation (e.g. Price and Torok 1989, Tullis and Yund 1991) and analog modeling using paraffin wax (e.g. Abbassi and Mancktelow 1990, Grujic 1993), modeling clay and bouncing putties (e.g. Ramberg 1955, Ghosh and Ramberg 1976) and crystalline materials (e.g. Bons and Urai 1995). Analog modeling using viscous materials such as polymers and bouncing putties offers the opportunity to investigate the development of structural elements such as folds, shear sense indicators, and stretching lineations in three dimensions during progressive deformation up to relatively high finite strain.

Several deformation machines have been designed to model flow in shear zones using analog materials; these are used to model simple shear flow (e.g. Robertson and Acrivos 1970, Price and Torok 1989), “circular” simple shear or Couette flow (e.g. Passchier and Sokoutis 1993) and general flow i.e. combinations of pure and simple shear (e.g. Giesekus 1962, Weijermars 1998, Cruden and Robin 1999, Griera and Carreras 1999). We designed an apparatus in which flow is homogeneous over a large part of the sample. In this apparatus it is possible to control strain rates along three perpendicular directions, and therefore all types of shear zones in monoclinic flow such as transpression and transtension (Fig. 3.1) can be modeled. Extending and contracting flexible walls of the deformation box are used to obtain homogeneous deformation. The described apparatus, therefore, offers the possibility to perform progressive homogeneous deformation at a chosen constant or changing strain rate and kinematic vorticity number  $W_n$  (Means et al. 1980) during progressive deformation in monoclinic flow. A large number of con-

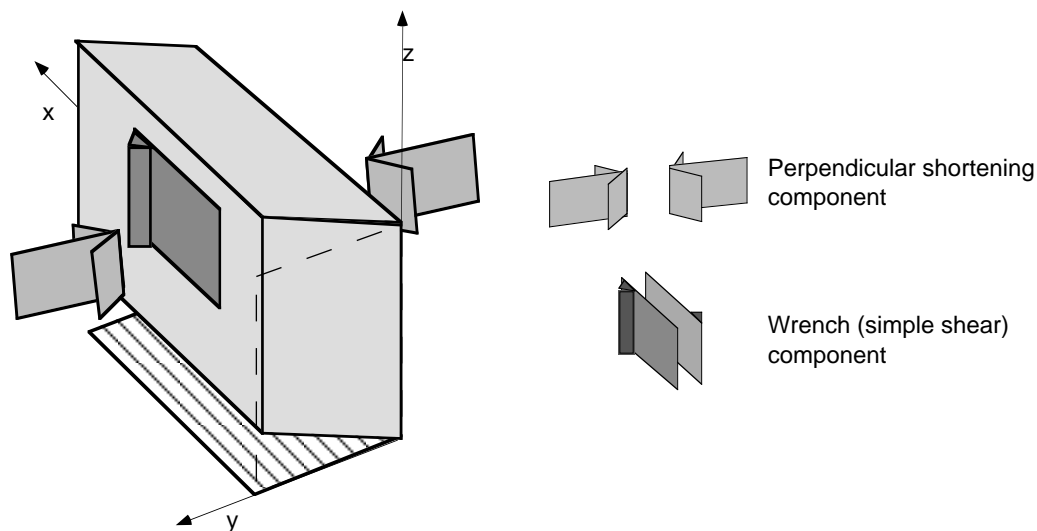


Figure 3.1. Illustration of homogeneous transpression (Sanderson and Marchini 1984) as combination of simple shear (wrench) component and simultaneous coaxial shortening component perpendicular to vertical shear plane. Example here is in plane strain (modified from Sanderson and Marchini 1984).

trolled inhomogeneous flow types and histories can also be modeled. A general description of the new apparatus, its possibilities and limitations, suitable materials, and experimental procedure is presented here. A set of pilot experiments is described to illustrate the scope of the apparatus.

### 3.2 Description of the apparatus

The apparatus assembly consists of four main parts: the deformation apparatus, a computer, a power driver subsystem, and a camera placed 50 cm above the deformation apparatus (Figs. 3.2 and 3.3).

The deformation apparatus consists of a four-sided deformation box that contains the sample and that we describe in an x-y-z reference frame (Fig. 3.2A). Two opposing sides are always parallel to the x-direction and the two other sides can rotate about the z-axis. The walls of the box are constructed from 1 cm  $\times$  12 cm Plexiglas segments (30 on the sides parallel to the x-direction, 20 on the other two sides), which are connected with flexible plastic to corrugated deformable pistons. Every second Plexiglas piece is connected at its back (side facing away from inner part of the box) to two metal springs. This construction ensures homogeneous contraction and extension of the walls. The range of the length of the sides parallel to the x-direction is between 15 and 30 cm and of the other two sides is between 5 and 20 cm. The springs are connected to four aluminum plates at the corners of the deformation box. A sheet made of 0.35 mm thick elastic latex forms the bottom of the deformation box. Its corners are fixed to the four aluminum plates. This construction results in a deformation box that slides with low friction on the basal plate and that is open at the top. Each one of the four aluminum plates (P) is attached to a sliding carriage (C1). These four sliding carriages are arranged two by two at each long side of the box, parallel to the x-direction. The sliding carriages sit on two PVC boards (B1) that are parallel to the long side of the box and attached to another set of four sliding carriages (C2) oriented parallel to the y-direction. These sliding carriages (C2) are attached to a 1 m  $\times$  1 m basal plate (B2). The contraction or extension of the flexible sides of the deformation box is controlled by six stepping motors (M). Four motors drive the movement of the corners of the box (P) in the x-direction via shafts and are fixed to the two PVC boards (B1). Two other motors are attached with shafts to the basal plate (B2) and control movement in the y-direction.

This configuration of motors and sliding carriages is chosen to meet two requirements: (1) the center of the deformation box has to remain in one place so that objects of interest in the deforming sample do not move with respect to the camera (Fig. 3.3); (2) all possible monoclinic flow types should be attainable. For simple shear, motors M1, M2, M3, and M4 move the corners of the deformation box at the same constant velocity but in different directions; M1 and M4 in the one direction and M2 and M3 in the opposite (Fig. 3.4). For pure shear M1 and M3 drive their corners of the deformation box in the x-direction and M2 and M4 move their corners in the y-direction. M5 and M6 control movement in the y-direction, and their velocity is determined by the velocity of the other 4 motors (Fig. 3.4) if flow is to be plane strain. Deformation in monoclinic flow at a constant kinematic vorticity number requires movement to be transmitted by all motors and recalculation of the velocity generated by the six motors for

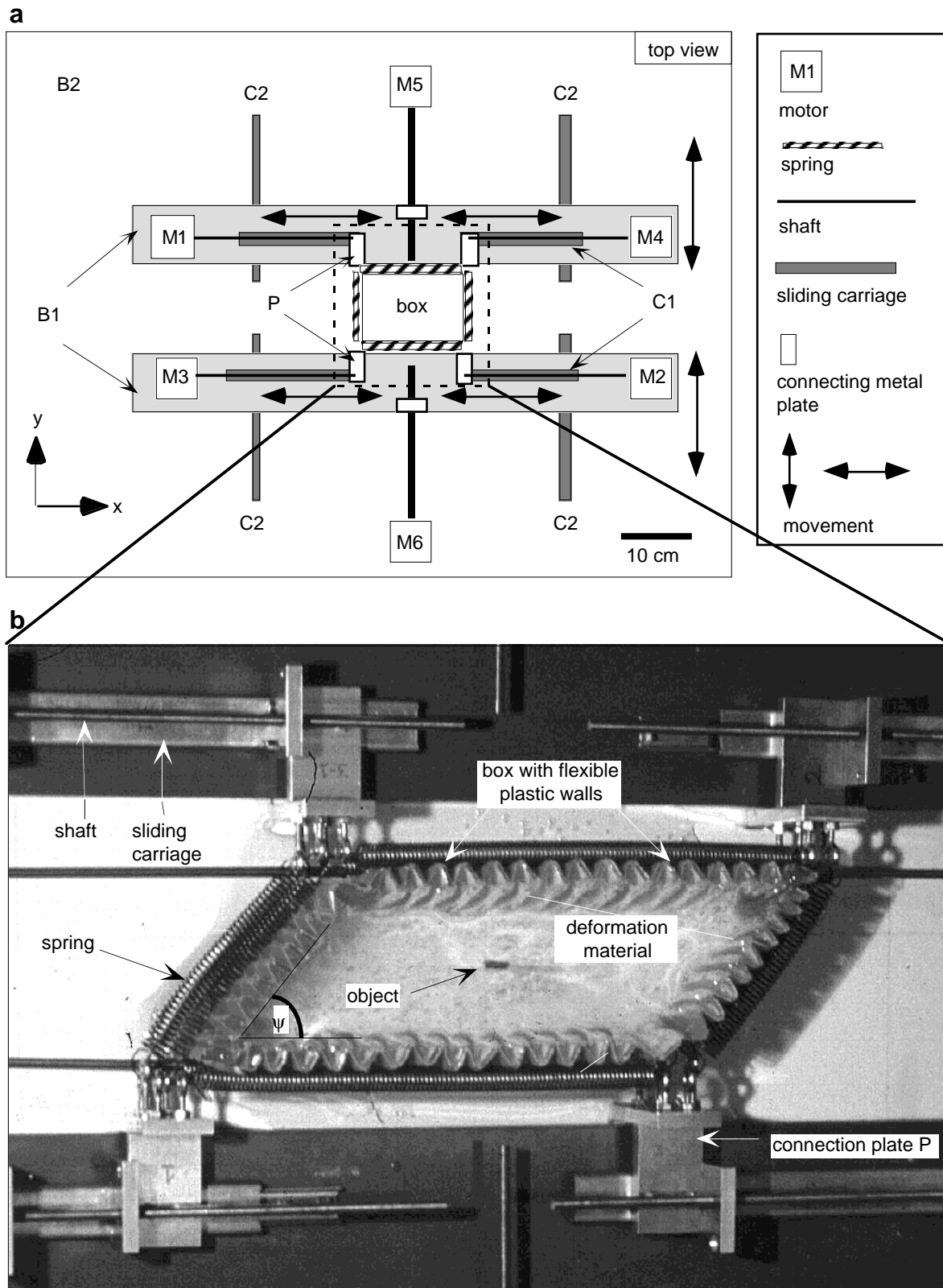


Figure 3.2. (a) Schematic drawing of deformation apparatus (view from top) where  $x$  and  $y$  are along symmetry axes of apparatus. B1 are PVC boards, B2 is base plate, C1 is set of 4 sliding carriages parallel to  $x$ -direction, C2 is set of 4 sliding carriages parallel to  $y$ -direction, P is connecting aluminum plates and M1 - M6 are motors. (b) Close-up of deformation box with flexible walls (view from top). Angle  $\psi$  is angle between sides of deformation box

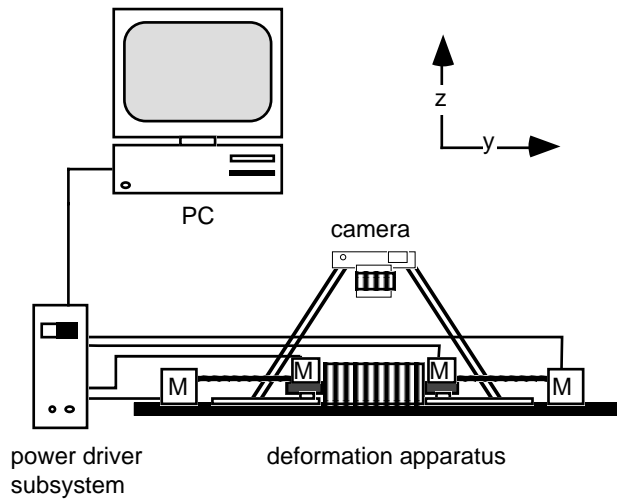


Figure 3.3. General set-up of apparatus;  $y$  and  $z$  are along symmetry axes of apparatus.

each time step, because the ratio of pure and simple shear is constantly changing during progressive deformation if the kinematic vorticity number  $W_n$  is to remain constant. Corresponding particle paths (Ramberg 1975) or flow lines (Fig. 3.4) are shown for the coordinate system used here, because the geometry of the flow lines is characteristic for each flow type (Passchier 1998).

A control panel allows the user to set specific parameters, such as the kinematic vorticity number and strain rate along a specific axis and duration of the experiment. Each second signals are passed on from the PC to the stepping motors via the power driver subsystem. The rotation angle per step is  $1.8^\circ$  with an accuracy of  $0.05^\circ$ . The velocity range is 1-10000 steps/s, which result in 0.005-50 rotations/s and a displacement of 0.005-50 mm/s. The range of possible displacement rates guarantees an accurate control of the movement of the four sides of the box, bulk strain rate, and progressive deformation type. The maximum shear strain that can be reached with our apparatus is restricted by the geometry of the shear box. For one experimental run, the maximum attainable  $R_{xy}$  value, defined as the strain axis ratio in the  $xy$ -plane, is 10 in simple shear and 4 in pure shear. Corresponding maximum finite shear strain  $\gamma$  for simple shear is 3, and for pure shear the maximum  $k$ -value is 2. In other flow types an  $R_{xy}$  of at least 4 can always be obtained. In practice, this means that the maximum duration of one experimental run achieving maximum finite shear strain is 180 min. Higher finite strains than the values mentioned here can be achieved with our machine, but only by running series of experiments. After each experimental run the precise orientation of the object is measured and photographed. After returning the box to the starting position the object is placed in the corresponding measured orientation and another experimental run under the same conditions as the previous run can be carried out. This technique is particularly useful when studying one or a few rigid objects (Passchier and Simpson 1986).

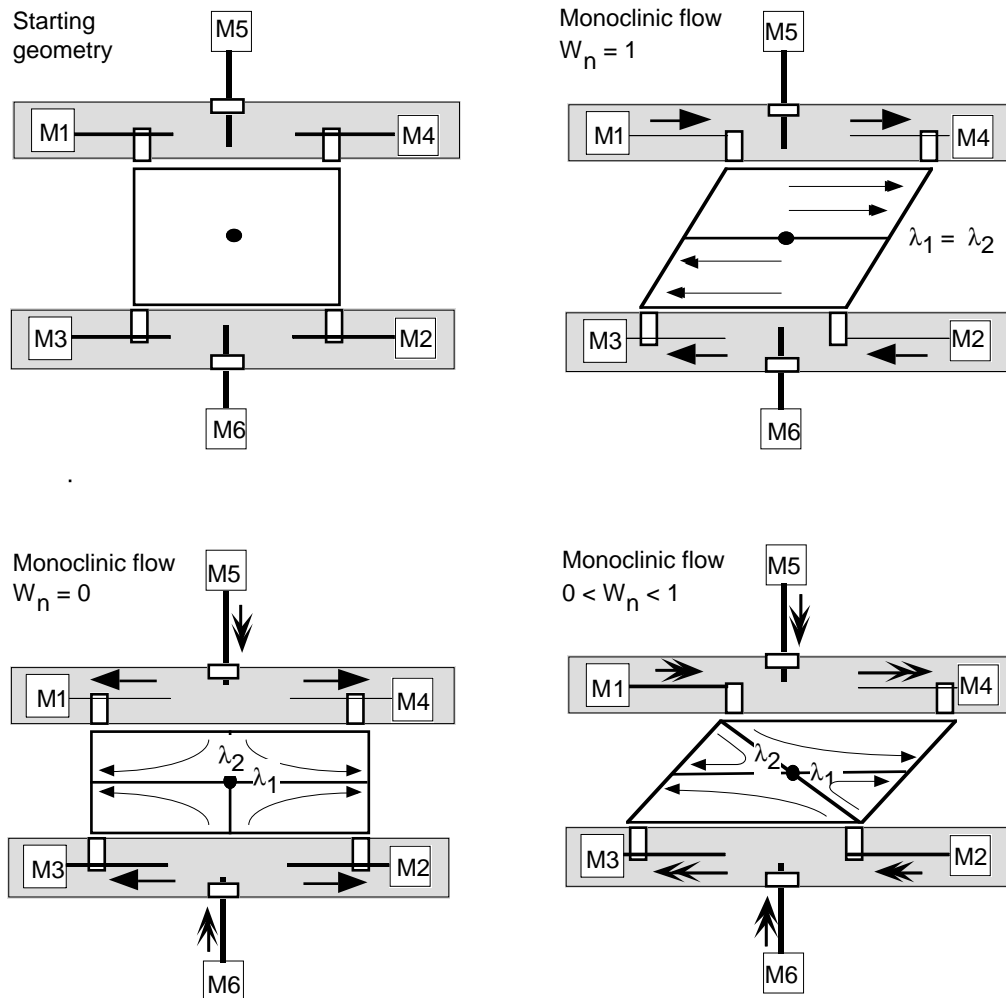


Figure 3.4. Schematic diagrams illustrating different flow types in shear box (see Figure 3.1). Arrows indicate direction of movement of pistons and specific parts in reference frame of machine; arrows with bold arrowheads signify constant velocity; double arrow heads indicate continuously changing velocity. Longer arrow indicates higher velocity. Within deformation box, bold lines signify flow apophyses ( $\lambda_1$  and  $\lambda_2$ ), and thin lines trace particle paths where small arrowheads point in direction of particle movement. Black dot is center of reference frame. M1- M6 are motors. Figure is not to scale.

### 3.3 Experimental materials

The range of suitable analog materials for our apparatus is restricted by two factors: leakage at the bottom of the deformation box and strength of the stepping motors. Leakage problems of the deformation box limits suitable materials to those with viscosities of at least  $10^3$  Pa s. The strength of the motors limits suitable materials to those with viscosities  $\leq 10^6$  Pa s, leaving a viscosity range of  $10^3 - 10^6$  Pa s. This means that most crystalline analog materials, as well as paraffin wax, cannot be deformed in our apparatus. Polymers such as Polydimethylsiloxane (PDMS; trade name: SGM 36; produced by Dow Corning, UK) a transparent polymer with a

density of  $0.965\text{gcm}^{-3}$  and consisting of repetitive chains; the longer the chain the higher the viscosity (Weijermars 1986), Rhodorsil Gomme a pinkish opaque bouncing putty produced by the Société des Chimiques Rhône-Poulenc (France) and mixtures of Rhodorsil Gomme and Plastilina (Swedish version of Harbutt's Plasticine; McClay (1976)) are ideally suitable for use in our shear box. For the first tests, which were performed to establish the properties of this shear box and for pilot experiments, we used PDMS and Rhodorsil Gomme. The flow behavior of both materials is Newtonian for strain rates below  $10^{-1}\text{ s}^{-1}$  (Fig. 3.5). At room temperature viscosities of PDMS and Rhodorsil Gomme are  $5.0 \times 10^4\text{ Pa s}$  and  $2.9 \times 10^4\text{ Pa s}$  (Weijermars 1986), respectively. A major advantage of PDMS over other materials commonly used in geological modeling is its transparency. Furthermore, it is nontoxic and relatively cheap. The flow behavior of Plastilina is highly non-Newtonian (Fig. 3.5) with  $n = 7.5$  (Weijermars 1986), where  $n$  is the stress exponent of power law flow.

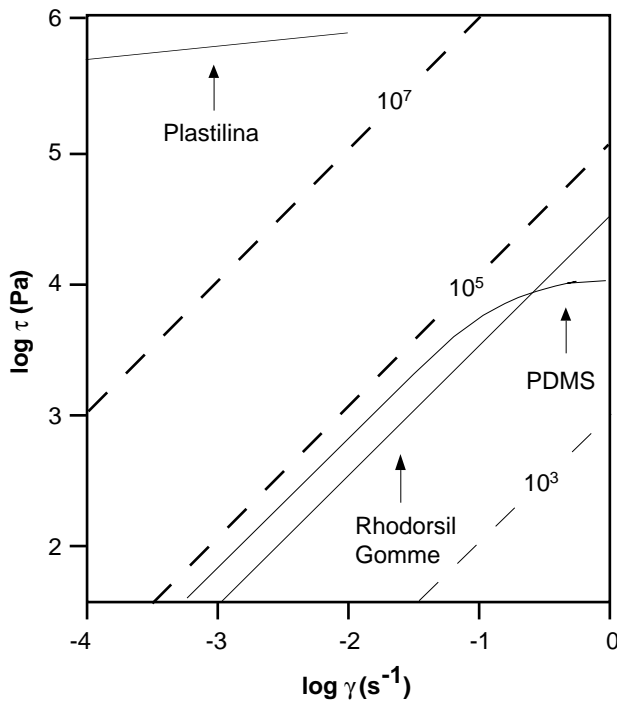


Figure 3.5. Graph illustrating shear stress and shear strain rate of some materials suitable for in the apparatus (modified from Weijermars 1986). Thin diagonal lines represent viscosity contours in Pa s. See text for discussion.

### 3.4 Types of flow modeled by new apparatus

In order to discuss the flow types that can be modeled with the new apparatus we use the terminology of Passchier (1998) to describe monoclinic flow. Passchier (1998) defined monoclinic flow using the instantaneous stretching axes (ISA), defined as vectors  $\mathbf{a}_I$ ,  $\mathbf{a}_{II}$  and  $\mathbf{a}_{III}$ , where  $a_I$ ,  $a_{II}$  and  $a_{III}$  are the magnitudes of stretching rates of material lines instantaneously parallel to the ISA. The vorticity vector  $\mathbf{w}$  is parallel to  $\mathbf{a}_I$ ;  $w$ , the vorticity, is the sum of the angular

velocity of material lines instantaneously parallel to  $\mathbf{a}_{II}$  and  $\mathbf{a}_{III}$  (Passchier 1997). Any type of monoclinic flow can now be described by the four numbers  $w$ ,  $a_I$ ,  $a_{II}$ , and  $a_{III}$ . Alternatively, three normalized numbers  $W_n$ ,  $A_n$  and  $T_n$  can be defined that describe the geometry of monoclinic flow completely.

These numbers are defined as the *sectional kinematic vorticity number*

$$W_n = w / (a_{II} - a_{III}),$$

the *sectional kinematic dilatancy number* (representing the instantaneous area change in the x-y plane during progressive deformation):

$$A_n = (a_{II} + a_{III}) / (a_{II} - a_{III}),$$

and the *sectional kinematic extrusion number* (representing the shortening or extension in the z-direction):

$$T_n = a_I / (a_{II} - a_{III}).$$

In addition, a *kinematic volume change number* can be defined as.

$$V_n = T_n + A_n.$$

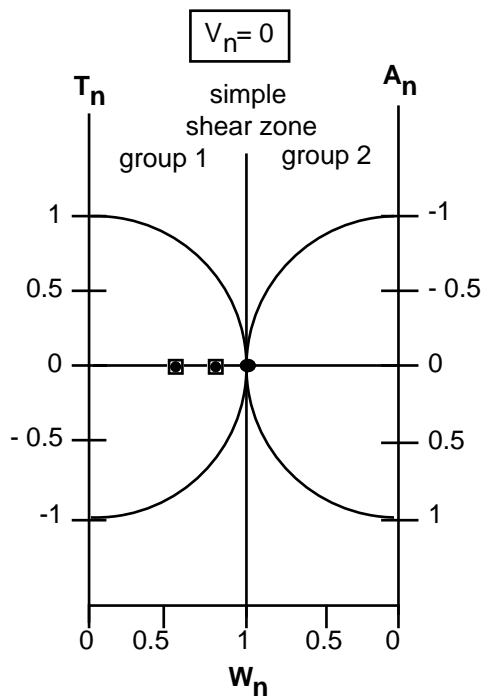


Figure 3.6. Representation of all types of homogeneous constant-volume monoclinic flow (modified from Passchier 1998).  $W_n$  is sectional kinematic vorticity number,  $A_n$  is sectional kinematic dilatancy number,  $T_n$  is sectional kinematic extrusion number.  $V_n$ , kinematic volume change number, is 0. With apparatus it is possible to model all shear zone types in this graph; open squares represent test experiments and black dots represent pilot experiments.



In our case  $V_n$  is approximately zero because of the incompressibility of the sample materials under our experimental conditions, and therefore  $T_n = -A_n$ . This means that all possible monoclinic flow types at  $V_n = 0$  can be depicted in a plane plotting  $W_n$  against  $A_n$  or  $T_n$  (Fig. 3.6). As many as three nonrotating material lines can be defined in monoclinic flow, the flow eigenvectors or apophyses. For our apparatus eigenvector  $\lambda_3$  is always parallel to the z-axis of our reference frame and  $\lambda_1$  is always parallel to the x-axis. The third eigenvector  $\lambda_2$  coincides with  $\lambda_1$  in simple shear flow, and otherwise  $\lambda_2$  is situated somewhere in the xy-plane. Two different main groups of monoclinic model shear regimes can be defined for shear boxes of this type, based on the magnitude of  $\lambda_1$  and  $\lambda_2$ . If  $|\lambda_1| > |\lambda_2|$  the shear zone is of group 1, and if  $|\lambda_1| < |\lambda_2|$  it is of group 2 (Fig. 3.6). Material lines parallel to the flow apophyses can be either instantaneously extending, shortening, or not changing in length. When there is no stretching or shortening along  $\lambda_3$  (plane strain flow),  $A_n$  and  $T_n$  are zero. Material lines parallel to either  $\lambda_1$  or  $\lambda_2$  are not deforming when  $A_n^2 + W_n^2 = 1$  (Passchier 1991, 1997), and these situations are represented by the circular curves in figure 3.6. All types of flow shown in figure 3.6 can be modeled with our apparatus.

### 3.5 Flow tests and boundary conditions

In order to test flow conditions that can be obtained in the shear box, we (1) checked the flow patterns in the shear box using particle paths, (2) obtained the distribution of  $R_{xy}$  throughout the sample, and (3) investigated the rotation rate of a sphere in simple shear flow.

To check the flow patterns several experimental runs were performed with different kinematic vorticity numbers and strain rates. We then compared flow lines observed in the matrix material with flow lines predicted by theory (Ramberg 1975) and the movement of particle in the central area of the box. The shear box was filled with PDMS. After a few hours of settling carbon powder was sprinkled on top of the material. An additional 5 mm thick layer of PDMS was then put on top of the carbon powder. Again a few hours of settling were needed to ensure a flat surface, which is necessary to observe the exact movement of the marker particles. All experiments were performed with a dextral shear sense. For the experiments, the initial dimensions of the shear box were 150 x 100 mm and the angle  $\psi$  between the sides (Fig. 3.2B) was  $135^\circ$  at the beginning of each experiment. The test experiments presented here were performed at constant kinematic vorticity numbers ( $W_n$ ) of 0.8 and 0.6, a strain rate in the x-direction of  $3.3 \times 10^{-4} \text{ s}^{-1}$ , and plane strain flow ( $T_n = A_n = 0$ ). Photographs were stacked on top of each other in order to determine the flow pattern (ten Brink 1996; Weijermars 1998). The acute angle  $\alpha$  between the two flow apophyses (Fig. 3.4) during homogeneous deformation can be expressed as  $\alpha = \arccos W_n$  for plane strain flow (Bobyarchick 1986, Passchier 1986). At  $W_n = 0.8$  the angle  $\alpha$  is  $36.9^\circ$  and at  $W_n = 0.6$  it is  $53.1^\circ$ . The observed  $\alpha$  values in the test experiments are  $37^\circ \pm 0.5^\circ$  at  $W_n = 0.8$  (Fig. 3.7A) and  $53^\circ \pm 0.5^\circ$  at  $W_n = 0.6$  (Fig. 3.7B). This demonstrates that the apparatus is well suited to model homogeneous flow in monoclinic shear zones. The experiments also indicate that the flow pattern is constant in time, as particle paths do not intersect during progressive deformation (Fig. 3.7). Hence, time independent plane strain flow is realized in at least part of the apparatus.

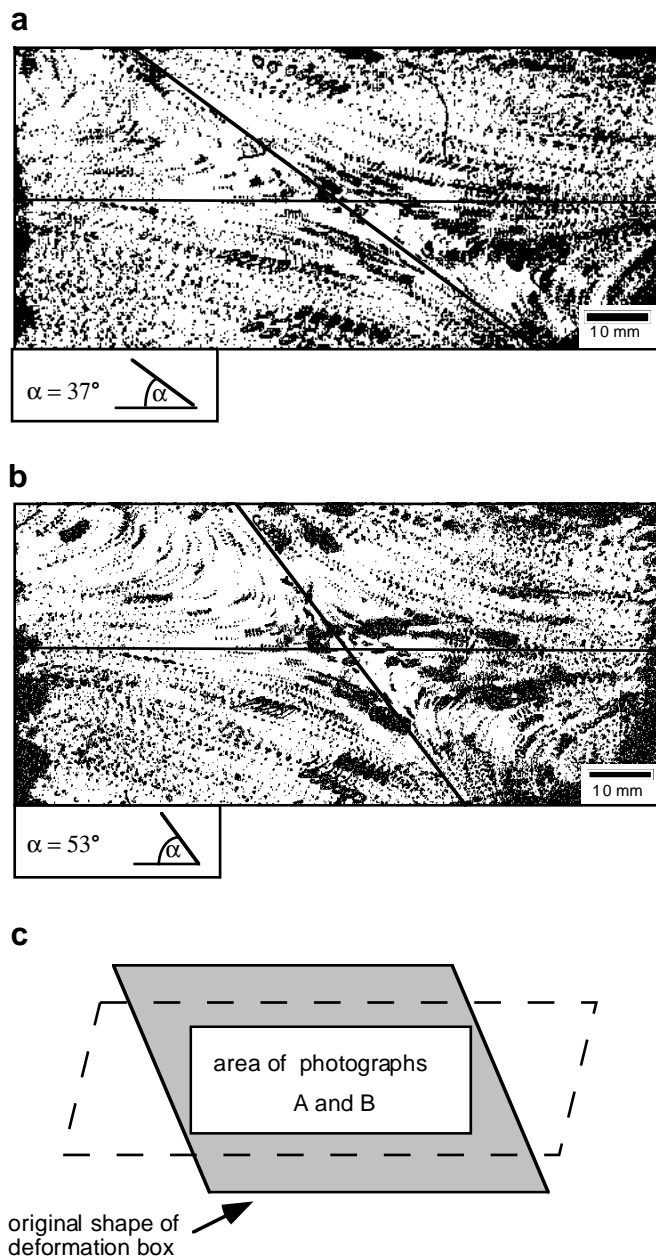


Figure 3.7. Diagrams illustrating particle paths within matrix material PDMS during progressive deformation at  $W_n = 0.8$  (A) and at  $W_n = 0.6$  (B). Series of photographs taken during test experiments were stacked onto each other in order to determine flow pattern during progressive deformation. Insets in (a) and (b) show theoretical acute angle  $\alpha$  between two flow apophyses (see Figure 3.4) during progressive deformation. (c) Position of area photographed during deformation (white box) inside deformation box. Original shape of deformation box is shown in gray and final shape is shown by dashed line.

To quantify the area of homogeneous deformation in the sample we performed a number of plane strain test experiments with different vorticities ( $W_n = 0.8, 0.6$ ), strain rates (stretching rate of the x-axis:  $2.0 \times 10^{-4} \text{ s}^{-1}$ ,  $3.3 \times 10^{-4} \text{ s}^{-1}$ ,  $4.7 \times 10^{-4} \text{ s}^{-1}$ ) and matrix materials (PDMS, Rhodorsil Gomme). The preparation and procedure of the experimental runs were identical to those described for the other test experiments. We used the computer program PatMatch (Bons and Jessell 1995), which performs strain analysis by analyzing displacements between two images to obtain the distribution of  $R_{xy}$  within a deformed sample. Results reveal that a large area of the samples deform homogeneously and the  $R_{xy}$  values closely correspond to theoretical values (Fig. 3.8). Inhomogeneous flow occurs only in a narrow zone adjacent to the corrugated walls. The width of this zone depends on the viscosity of the matrix material and is inde-

pendent of the kinematic vorticity number and strain rate (within the accuracy of our measurements). For PDMS the width of the zone with inhomogeneous flow is 0.8 to 1.3 cm measured from the tips of the corrugated wall; for Rhodorsil Gomme this width is 0.6 to 1.1 cm.

A third set of experiments investigated the behavior of a rigid sphere in plane strain simple shear flow at a simple shear strain rate of  $1 \times 10^{-3} \text{ s}^{-1}$  to a finite strain  $\gamma$  of 2. We inserted a Plexiglas sphere with a diameter of 0.8 cm in the middle of the deformation box and took a number of consecutive photos during progressive deformation. Figure 3.9 shows the change in orientation of the sphere ( $\theta$ ) against simple shear strain ( $\gamma$ ) observed in the experiment and the theoretical values of rotation (Ghosh and Ramberg 1976). Experimental values show good agreement with theoretical values.

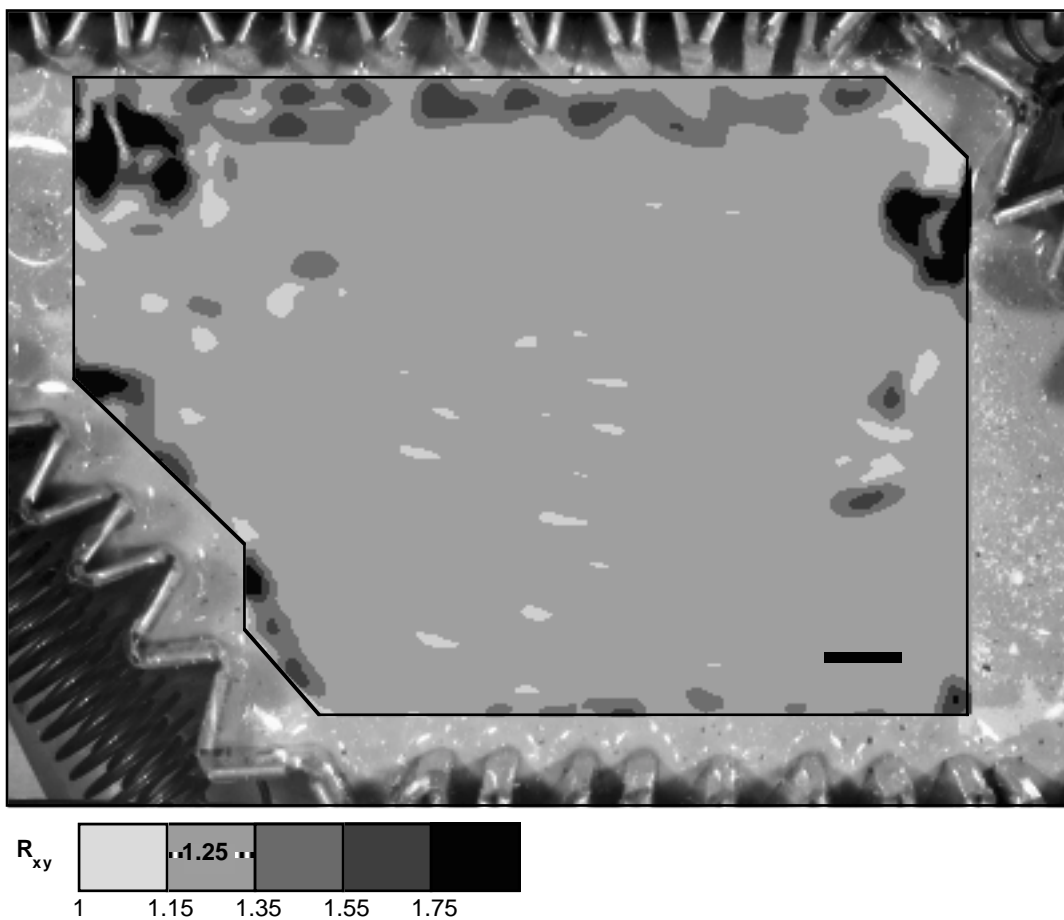


Figure 3.8. Photograph of deformation box. Inset represents distribution of  $R_{xy}$  values over analyzed area of sample. Inset was generated using pattern matching program PatMatch (Bons and Jessell 1995). Different gray shades represent different ranges of  $R_{xy}$  values. Dashed line in legend represents theoretical value of  $R_{xy}$  ( $R_{xy} = 1.25$ ) and at same time measured average of analyzed area (excluding narrow zone close to pistons). Most of analyzed area exhibits  $R_{xy}$  values that correspond to theoretical value of  $R_{xy}$ . Note that on upper left corner and on upper right side reflections cause significant errors in PatMatch routine, because program cannot identify patterns in reflected areas. Experimental conditions are:  $W_n = 0.6$ , stretching rate in  $x$ -direction is  $3.3 \times 10^{-4} \text{ s}^{-1}$ , and sample material is Rhodorsil Gomme. Scale bar = 1 cm.

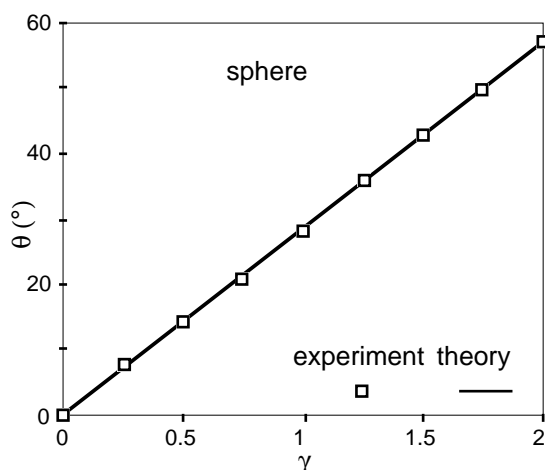


Figure 3.9. Graph illustrating change in orientation of rigid sphere as function of shear strain in simple shear flow ( $W_n = 1$ ). Solid line represents theoretical values (after Ghosh and Ramberg, 1976) and squares represent experimental values.

The flow tests presented here are all in plane strain ( $A_n = T_n = 0$ ), where the specimen surface remains flat. Under these conditions a large volume of homogeneous flow can be obtained. In experiments with extrusion of material parallel to the z-axis ( $A_n \neq 0$  and  $T_n \neq 0$ ), the rigidity of the pistons in the z-direction causes the sample surface to attain a parabolic shape, which has an effect on the flow homogeneity. Accordingly, any user of our apparatus working at  $T_n \neq 0$  should test the effect of boundary conditions for the specific experimental setup used.

Leakage of material with a viscosity of  $5.0 \times 10^4$  Pa s out of the deformation box is  $< 0.5$  vol% during one experimental run if the experimental duration is  $< 4$  hr. Leakage does not exceed 1 vol% in 24 hr if the sample material (viscosity:  $5.0 \times 10^4$  Pa s) is left in the deformation box without performing experiments.

### 3.6 Pilot experiments: rotation of mica fish in plane strain

As an example of the practical application of our apparatus, we present the modeling of mica fish. Mica fish are commonly observed in mylonites and their asymmetrical form and the stair-stepping of their tails are often used to determine shear sense (Lister and Snoke 1984, Passchier and Trouw 1996). Study of natural mica fish shows that in the plane parallel to the stretching lineation and perpendicular to the foliation, their shape is predominantly monoclinic. All studied examples lie with their long axis tilted  $2^\circ - 40^\circ$  with respect to the inferred flow plane (ten Grotenhuis and Passchier 1999). This could mean that mica fish are in a stable irrotational position with respect to the apophyses of bulk flow for at least part of their evolution. In addition, it is not clear to what extent object shape, flow partitioning,  $W_n$ , or other factors influence the development of mica fish. Our deformation apparatus is suitable to study kinematic aspects of the development of such mica fish.

Analytical work of Ghosh and Ramberg (1976) showed that in two-dimensional homogeneous flow with a particular kinematic vorticity number, the rate of rotation of a rigid elliptical particle in a Newtonian viscous fluid varies in a systematic manner depending on the orientation and the axial ratio ( $R_{ob}$ ) of the inclusion. This means that the orientation of the particle is a

function of the initial angle, the aspect ratio of the particle, and strain. Until now, experiments investigating the rotation of rigid objects in homogeneous flow were mainly restricted to simple shear (Ghosh and Ramberg 1976, ten Brink 1996). With our apparatus, we can expand such work to homogeneous monoclinic flow experiments.

To investigate the effect of object shape on the rotation behavior we performed experiments with a monoclinic object in a Newtonian viscous fluid (PDMS). The object is made of rigid India rubber and has a long side  $A$  of 10 mm, a short side  $B$  of 7 mm, and height  $h$  of 16 mm (Fig. 3.10). The angle between  $A$  and  $B$  is  $135^\circ$ . The aspect ratio of the object ( $R_{ob}$ ) in the  $xy$ -plane is three. The angle  $\theta$  is between the long axis of the object and the  $y$ -direction of the reference frame. Angles are measured clockwise.  $A$  and  $B$  are parallel to the  $z$ -axis. The object is placed in the middle of the box with its top 5 mm below the surface of the PDMS and parallel to the  $y$ -direction,  $\theta_0 = 0^\circ$ . The experiments model plane strain monoclinic flow ( $T_n = 0$ ) with kinematic vorticity numbers ( $W_n$ ) of 1 (simple shear flow), 0.8, and 0.6 (Fig. 3.6). In the simple shear experiment the simple shear strain rate is  $1 \times 10^{-3} \text{ s}^{-1}$  and the final shear strain  $\gamma$  is 3. For the flow experiments at  $W_n = 0.8$  and  $W_n = 0.6$  the stretching rate along the  $x$ -axis is held constant at  $3.3 \times 10^{-4} \text{ s}^{-1}$ . After one experimental run the maximum  $R_{xy}$  value reached was 3.58 at  $W_n = 0.8$  and 2.68 at  $W_k = 0.6$ . For the experiments with  $W_n = 0.8$  and 0.6, seven consecutive runs were performed.

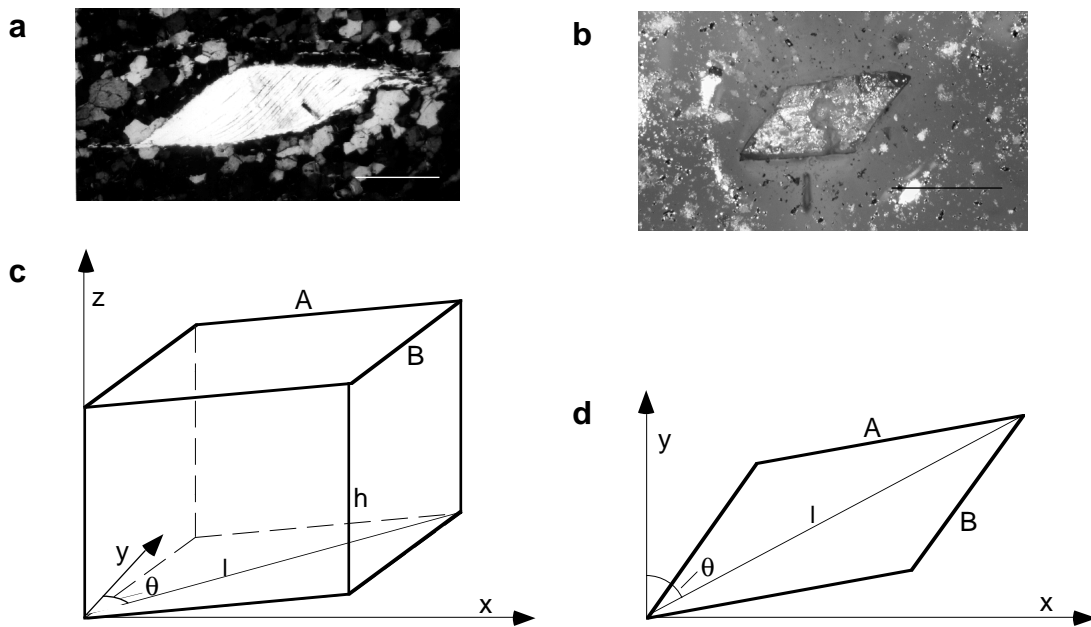


Figure 3.10. (a) Natural example of muscovite mica fish (Ribeira belt, Brazil); crossed polars, scale bar = 1 mm. (b) Photograph of object used in experiments, inserted in its matrix (PDMS); scale bar = 10 mm. (c) Schematic three-dimensional drawing of rigid monoclinic object used as analog for mica fish;  $x$ ,  $y$ , and  $z$  correspond to reference frame of apparatus,  $h$  is height,  $l$  is longest axis of object, and  $\theta$  is angle between longest axis ( $l$ ) and  $y$ -axis of reference frame. (d) Schematic drawing of  $AB$ -plane of object

Figure 3.11 shows the experimental results and the theoretical orientation of the long axis for ellipses with  $R_{ob} = 3$  against the simple shear component of strain ( $\gamma$ ) for  $W_n = 1$ ,  $W_n = 0.8$  and  $W_n = 0.6$  (equations (11) - (13) in Ghosh and Ramberg 1976). We chose to plot the simple shear component of strain ( $\gamma$ ) and not  $R_{xy}$  in Figure 3.11 because  $\gamma$  increases linearly with progressive deformation. The highest  $\gamma$  value for one experimental run was 1.08 at  $W_n = 0.8$  and 0.61 at  $W_n = 0.6$ .

The experiments show a deviation in the orientation of the lozenge object from theoretical values for ellipses. In simple shear the rotation curves of the object and the theoretical curve of an ellipse with  $R_{ob} = 3$  differ considerably (Fig. 3.11A). The theoretical curve for an ellipse of  $R_{ob} = 2.7$  fits the experimental results better with regard to the amount of shear strain necessary

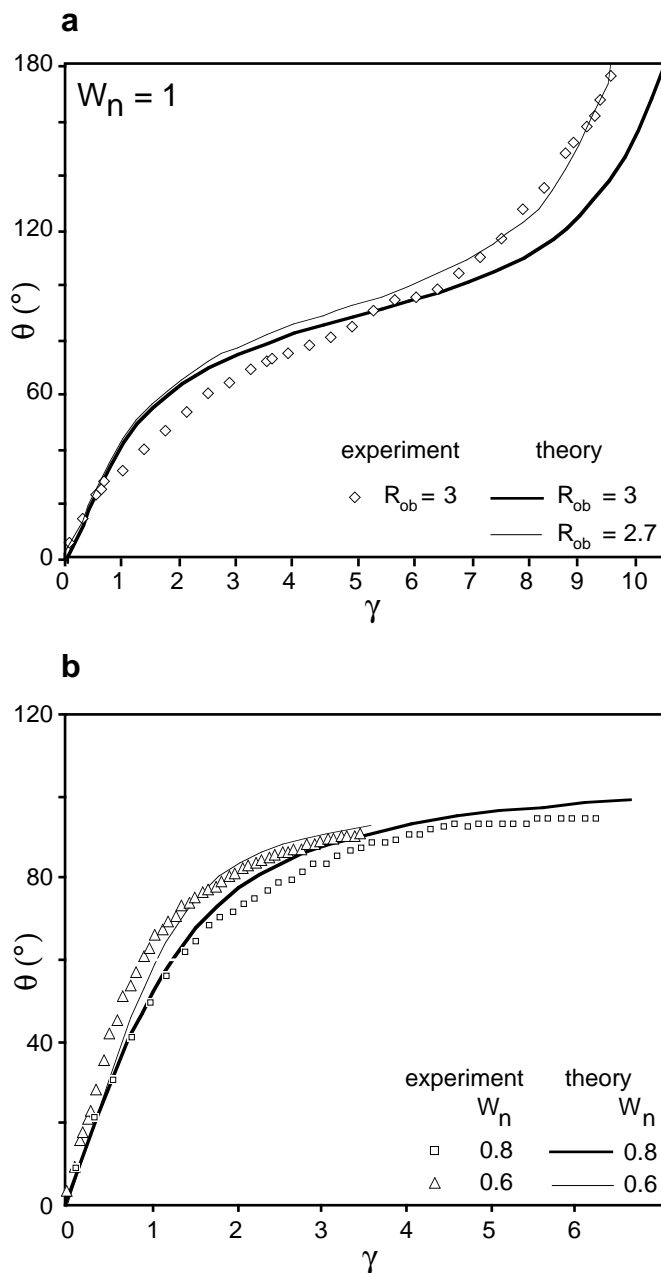


Figure 3.11. (a) Graph illustrating change in orientation of rigid monoclinic object ( $\theta$ ) as function of simple shear component of strain in monoclinic flow with  $W_n = 1$ . Solid line represents theoretical values (after Ghosh and Ramberg, 1976) and symbols represent experimental values.  $R_{ob}$  is aspect ratio of object. (b) Graph illustrating change in orientation of rigid monoclinic object ( $\theta$ ) with aspect ratio of 3 as function of simple shear strain in monoclinic flow with  $W_n = 0.8$  and 0.6. Solid lines represent theoretical values (after Ghosh and Ramberg, 1976) and symbols represent experimental values.

for a  $180^\circ$  rotation of the object, but the shape of the curves ( $\theta$  versus  $\gamma$ ) is systematically different (Fig. 3.11A). In monoclinic flow with  $W_n = 0.8$  and  $W_n = 0.6$  experimental results show that the object attains a semi-stable position (Fig. 3.11A). This position is  $95^\circ$  at  $W_n = 0.8$  and  $90^\circ$  at  $W_n = 0.6$  (Fig. 3.11B). Theory predicts  $5^\circ$  higher values for the semistable position of an ellipse of  $R_{ob} = 3$  in both experimental flow types. Theoretical values for an ellipsoid with  $R_{ob} = 2.7$  show even stronger deviations from experimental results. We suggest that the observed deviation from theory is due to the shape of the rigid object. Both the axial ratio of an object and its shape i.e. elliptical, rectangular, or lozenge-shaped influence the behavior of such an object in monoclinic flow.

Nevertheless, the preferred orientation ( $\theta$ ) of mica fish in nature is  $50^\circ$  to  $88^\circ$  using the reference frame of the experiments. Therefore, monoclinic flow with a kinematic vorticity number smaller than 1 cannot be the only explanation for the orientation of mica fish in shear zones, and further experiments are needed to explain the behavior of these structures.

### 3.7 Conclusions

The newly developed apparatus described in this paper can combine simple and pure shear independently and simultaneously and allows the modeling of structures in all types of homogeneous monoclinic flow, as illustrated in Passchier (1998). Test and pilot experiments show that flow in the apparatus is homogeneous in plane strain except for a small zone along the pistons, and that particle paths,  $R_{xy}$ , and rotation rates of spheres are comparable to theoretical values in monoclinic shear zones. Limitations of the apparatus are the maximum finite strain of one experimental run, availability of suitable analog materials, and the limited range of attainable strain rates. For one experimental run, the maximum strain axis ratio in the  $xy$ -plane  $R_{xy}$  is at least 4 for all types of monoclinic flow that can be modeled in the machine. The setup of the apparatus and technical limitations restrict suitable materials to those with a viscosity in the range of  $10^3$  to  $10^6$  Pa s. The attainable range of strain rate is strongly dependent on the analog material used.





## Chapter 4

### Are polymers suitable rock-analogs?

#### Abstract

To evaluate if a polymer is suitable for analog modeling it is essential to know the rheological properties of the material. Polymers used in analog modeling exhibit a complex rheological behavior only part of which has been taken into account in most modeling studies. The mechanical behavior is strongly dependent on strain rate and temperature, and is characterized by specific dependencies of the storage and loss moduli, related to the elasticity and viscosity, on the deformation rate (frequency).

We present a set of new data from measurements with an oscillatory parallel-disk rheometer obtaining the storage and loss moduli at a broad range of frequencies and strains. Investigated materials are polydimethylsiloxane (PDMS), mixtures of PDMS and BaSO<sub>4</sub> (filler), Rhodorsil Gomme and mixtures of Rhodorsil Gomme and plasticine, all commonly used in analog experiments.

Our results show that mixtures of plasticine and Rhodorsil Gomme exhibit a dependence of the rheological properties with strain and therefore these mixtures are problematic for analog modeling. For mixtures of PDMS and BaSO<sub>4</sub>, the significance of the elastic component increases with increasing filler content, accordingly these mixtures have a limited application for modeling of viscous deformation. Pure PDMS and Rhodorsil Gomme exhibit Newtonian flow behavior at strain rates commonly used in analog modeling.

#### 4.1 Introduction

Polymers (e.g. Polydimethylsiloxane (PDMS)) and polymers with fillers (e.g. bouncing or silicone putties) in combination with other materials (e.g. sand) have been extensively used for analog modeling in geosciences for decades. Polymers have been applied in experiments modeling the development of small-scale structures in ductile shear zones (e.g. Ghosh and Sengupta 1973, Fernandez et al. 1983, Ildefonse et al. 1992a,b, Passchier and Sokoutis 1993), medium-scale structures such as boudinage or mullions (e.g. Ramberg 1955, Ghosh and Ramberg 1976, Sokoutis 1987, Kobberger and Zulauf 1995) and strain variation in layers of different rheology (e.g. Treagus and Sokoutis 1992), and large scale fold and fault structures (e.g. Dixon and Summers 1985, Brun et al. 1994). In large-scale experiments polymers are commonly used to represent the ductile lower crust. Polymers are also used to model rising plumes, convection, magmatic fabric developments, and emplacement of igneous bodies (e.g. Whitehead and Luther, 1975, Nataf et al., 1984, Roman-Berdiel et al. 1995, Anma 1997, Anma and Sokoutis 1997, Donnadieu and Merle 1998).

Several papers have been published in the geological literature which specifically or in parts investigate the physical properties of polymeric liquids and related materials (e.g. McClay 1979, Dixon and Summers 1985, 1986, Weijermars 1986, Sokoutis 1987, Treagus and Sokoutis 1992, Kobberger and Zulauf 1995). McClay (1976) and Kobberger and Zulauf (1995) performed constant strain rate, plane strain compression tests and concluded that the mechanical behavior of different types of plasticine is complex, but that after a certain amount of strain it is linear viscoelastic. Dixon and Summers (1985, 1986) used an annular shear rig to obtain rheological properties of a silicone putty. They have shown that the mechanical behavior of the silicone putty and the plasticine cannot be fully described by flow laws which are used to describe rock deformation (power-law flow, Newtonian flow, Bingham flow behavior). Sokoutis (1987) and Sokoutis and Treagus (1992) used a capillary (extrusion) viscometer and a concentric cylinder (Couette) viscometer. Weijermars (1986) performed additional measurements with a Stokes (falling-ball) viscometer and a Weissenberg cone and plate rheometer, for the investigation of the viscosity of polymeric analog materials (plasticine, Rhodorsil Gomme, polymers and mixtures). They reported changes in viscosity with strain rate. In all these studies no other rheological properties than effective viscosity were measured.

Geologists performing analog modeling need comprehensive information about the rheological character of a material to evaluate its suitability as a rock analog. However the knowledge of the rheological properties of analog materials in the geological literature is strongly restricted to analyses of effective viscosity without specification of any other rheological quantities. Quantities such as the loss and storage moduli especially when determined in a broad range of deformation rates allow to determine the rheological character of a material (Nelson and Dealy 1993).

We performed a series of rheological measurements on several commonly used polymers. Our results show that the mechanical behavior is complex and that some commonly used polymers are in fact problematic as analog materials for rocks.

## **4.2 Structure and deformation of polymeric liquids**

### *4.2.1 Structure and mechanical behavior of polymeric liquids*

Polymeric materials used for analog modeling belong to the so-called thermoplastics. These are characterized by flexible linear chain-like macromolecules, which are formed by chemical binding of a number of small molecules (monomers). The polymer chains, when sufficiently long, are entangled and assume complex three dimensional structures. The mean form of the three dimensional structure can be characterized as a soft ellipsoid, the size of which is chain length dependent. In an undeformed system, the chains assume an equilibrium state with random orientation of their long axes (Winter et al. 1993). During deformation chains can reorient with their long axes preferentially directed towards the drawing direction, can straighten and finally can glide past each other (Fig. 4.1). When deformation ceases, chains tend to "relax" to their equilibrium state both by a form retraction and by a randomization of orientation. Therefore, polymers behave like an elastic material when a high stress is applied for a short time (less than the chain relaxation time) but like a viscous material when a low stress is applied for a long time (longer than the chain relaxation time). For a constant imposed strain, the initial elastic response is gradually converted into permanent viscous deformation and the associated

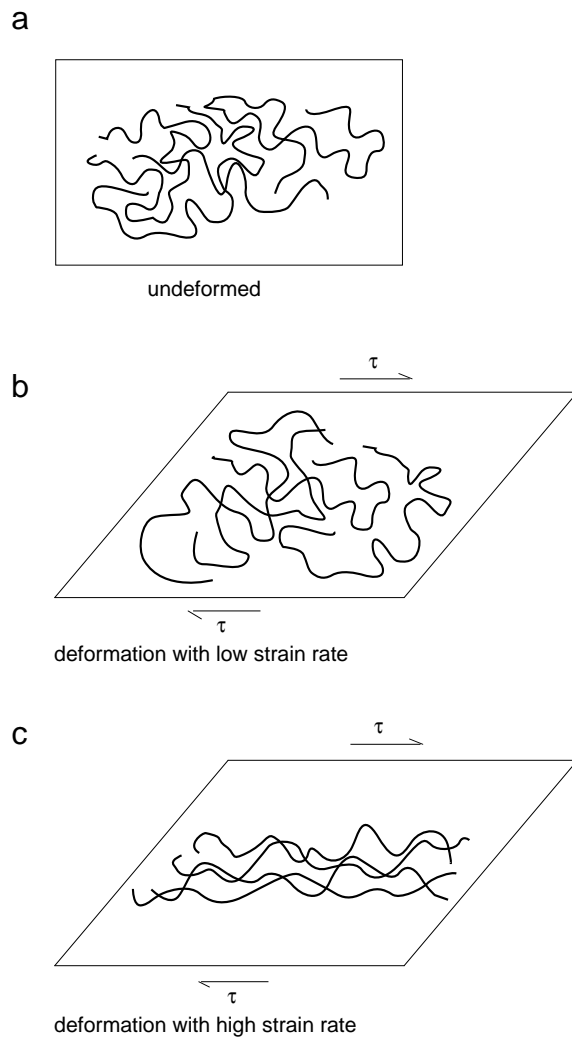


Figure 4.1. Sketch of chains of a polymeric liquid in a) undeformed equilibrium state, b) deformed state at low deformation rate relative to relaxation time of polymer chains, c) deformed state at high deformation rate relative to relaxation time of polymer chains.

stress decays with time (Maxwell model). Such behavior is termed viscoelastic as it is characterized by a combination of elastic deformation and viscous flow. An important feature of viscoelastic materials is the time-dependence of rheological properties (Askeland 1990). At a certain range of deformation rates time-independent rheological properties may be observed for a given material but there certainly exists a range where the material will show time-dependent properties. Besides this time-dependence, properties of viscoelastic materials can be strain-independent, "linear" or strain-dependent, "non-linear". The term linear viscoelastic is used when during testing the material remains in equilibrium state and the rheological properties are not influenced by the conditions of testing, hence rheological properties are strain-independent. The term non-linear viscoelastic is used when the material structure is altered under observed conditions and consequently rheological properties are strain-dependent. (Fig. 4.1).

#### 4.2.2 Viscoelastic properties of polymers

##### 4.2.2.1 Linear viscoelastic behavior

The properties of linear viscoelastic materials are usually described by the storage  $G'$  and loss  $G''$  moduli (Table 4.1), whereby the storage and loss moduli are representative for the elastic and viscous component, respectively (Nelson and Dealy 1993).

Table 4.1. Notation

---

$a_T$	shift factor for calculation of mastercurve
$G'$	storage modulus, Pa
$G''$	loss modulus, Pa
$G_0$	elastic shear modulus, Pa
$G$	shear modulus, Pa
$k$	constant
$n$	power law exponent
$T_{\text{ref}}$	reference temperature for the calculation of mastercurve, °C
$T_m$	experimental temperature for the calculation of mastercurve, °C
$\delta$	phase shift angle
$\gamma$	shear strain
$\dot{\gamma}$	shear strain rate, $s^{-1}$
$\gamma_0$	shear strain amplitude
$\eta$	kinematic viscosity, Pa s
$\eta^*$	complex viscosity, Pa s
$\eta_0$	zero shear viscosity, Pa s
$\omega$	frequency, $\text{rad s}^{-1}$
$\omega_m$	experimental frequency, $\text{rad s}^{-1}$
$\omega_r$	frequency where $G' = G''$ , $\text{rad s}^{-1}$
$\sigma$	shear stress
$\sigma$	shear stress amplitude
$\tau$	relaxation time, s

---

These material properties are usually determined by applying sinusoidal shear strain of amplitude  $\gamma_0$  and frequency  $\omega$  to a sample. The shear strain as a function of time is

$$\gamma(t) = \gamma_0 \sin(\omega t) \quad (4.1)$$

and the corresponding shear strain rate

$$\dot{\gamma}(t) = \gamma_0 \omega \cos(\omega t) \quad (4.2)$$

If the response is linear, the resulting shear stress will also be sinusoidal but can be shifted in phase as follows

$$\sigma(t) = \sigma_0 \sin(\omega t + \delta) \quad (4.3)$$

where  $\delta$  is the phase shift angle and  $\sigma_0$  is the stress amplitude (Nelson and Dealy 1993, Jeffrey Giacomini and Dealy 1993).

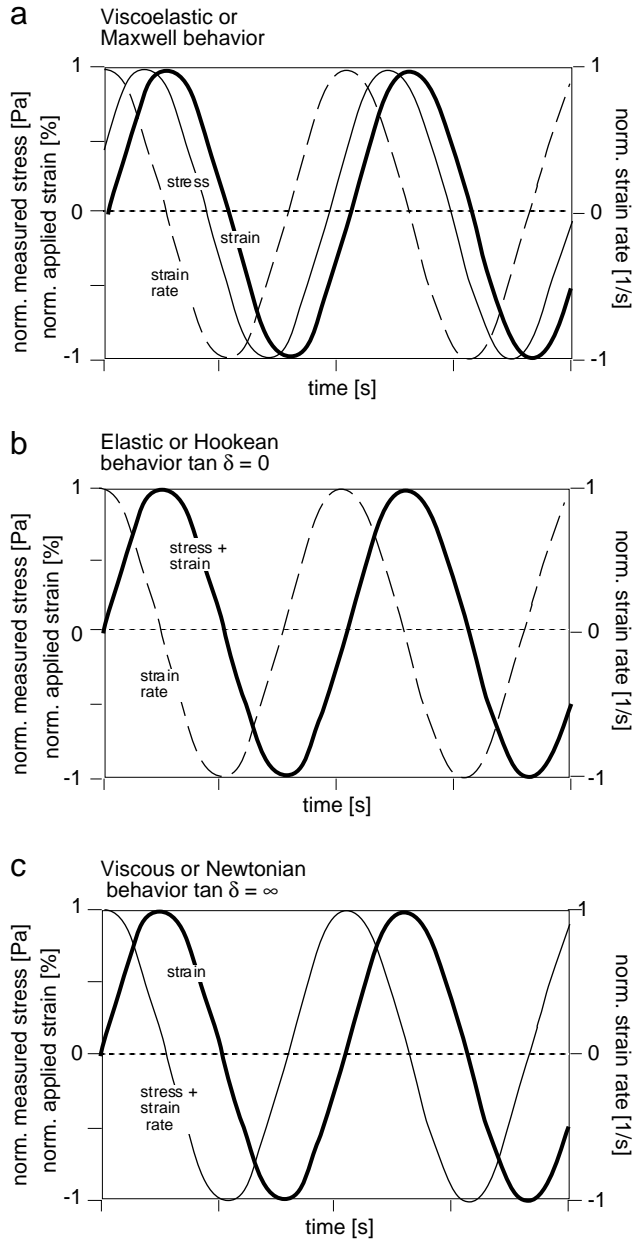


Figure 4.2. Graph to illustrate the applied sinusoidal strain and strain rate and resulting stress. a) Viscoelastic or Maxwell behavior; resulting stress is not in phase with the applied strain or strain rate. b) Elastic or Hookean behavior; resulting stress is in phase with the applied strain. c) Viscous or Newtonian behavior; resulting stress is in phase with the strain rate.

The phase angle  $\delta$  can be regarded as characterizing the distribution of the deformation energy into the two fractions: (1) the energy stored in the system as an elastic deformation and (2) the energy lost irreversibly. For purely elastic behavior  $\delta$  is zero, and the ratio between shear stress and strain is constant in time. For viscous behavior  $\delta = \pi/2$  and the ratio between the shear stress and strain rate is constant (Fig. 4.2).

The shear stress is usually written as a trigonometric identity as follows

$$\sigma(t) = \gamma_0 [G' \sin(\omega t) + G'' \cos(\omega t)] \tag{4.4}$$

and  $\delta$  as

$$\tan \delta = \frac{G''}{G'} \tag{4.5}$$

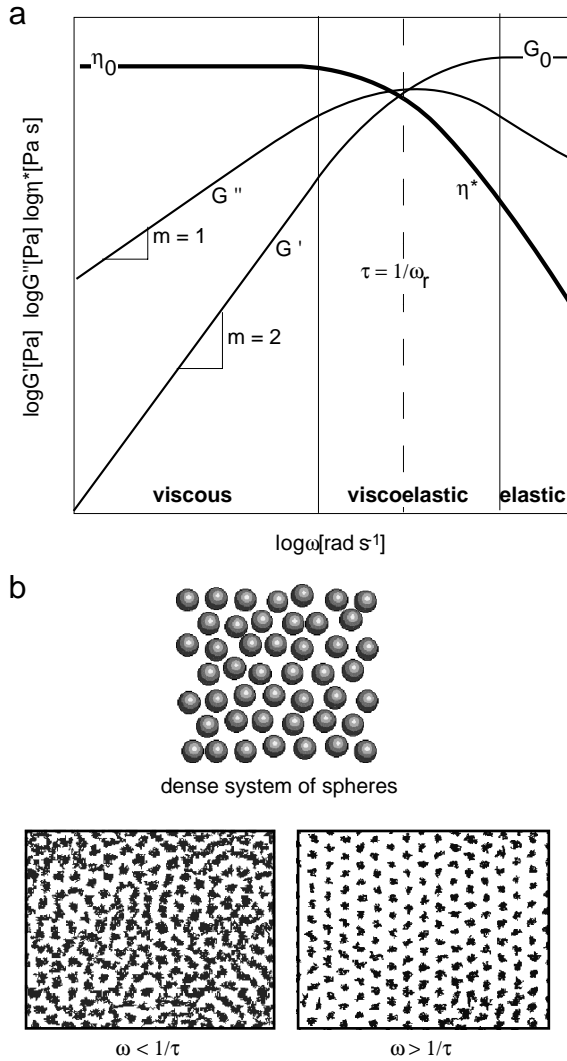


Figure 4.3. Representation of typical rheological properties of linear viscoelastic material; a) plot of log frequency ( $\omega$ ), against log storage modulus ( $G'$ ) and loss modulus ( $G''$ ); different fields signify different mechanical behavior, determined by the relation between  $G'$  and  $G''$ . Viscous behavior is characterised by  $G'' \gg G'$  and slopes of  $G''$  and  $G'$  of 1 and 2 respectively. Elastic behavior is characterised by  $G' \gg G''$  and by a constant value for  $G'$ . Viscoelastic field is between the elastic and viscous field.  $\eta^*$  [Pa] is the complex viscosity; b) representation of centre paths of particles in a simple model (dense system of spheres) corresponding to low ( $\omega < 1/\tau$ ) and high ( $\omega > 1/\tau$ ) deformation rate.

where  $G'(\omega)$  is the storage modulus and  $G''(\omega)$  is the loss modulus. In a simple viscoelastic system both moduli are functions of frequency with a characteristic behavior, which is linked to the relaxation time of the structural units e.g. the polymer chains. An example of such behavior is illustrated schematically in Figure 4.3. In such a diagram a plateau of  $G'$  and a low  $G'/G''$  ratio ( $G' \gg G''$ ) are both characteristic for elastic behavior (Hookean). The elastic shear modulus describing the material properties in this range is given by

$$G_0 = \lim_{\omega \rightarrow \infty} G'(\omega) \quad (4.6)$$

In the frequency range where  $G'' \gg G'$  and where  $G'$  and  $G''$  obey the characteristic proportionalities to  $\omega^2$  and  $\omega$ , respectively, flow behavior is viscous (Newtonian). Here the system can be characterized by the complex viscosity  $\eta^*(\omega)$  given by

$$\eta^*(\omega) = \frac{\sqrt{G'^2 + G''^2}}{\omega} \quad (4.7)$$

(Winter et al. 1993). The complex viscosity  $\eta^*(\omega)$  is equal to the kinematic viscosity  $\eta$  *only* if  $G'' \gg G'$ . Only in this range, the viscosity is a meaningful material property and the complex viscosity can then approach the value of the zero shear viscosity

$$\eta_0 = \lim_{\omega \rightarrow 0} G''(\omega) / \omega \quad (4.8)$$

The intermediate cross-over region between the two limiting types of behavior (elastic and viscous) can be regarded as typically viscoelastic (Maxwell). The point at which  $G'$  and  $G''$  cross each other determines the place ( $\omega_p$ ) on the frequency scale which is related to the relaxation time  $\tau$  of the structural units constituting the system, ( $\tau=1/\omega_p$ ). Assuming a simple Maxwell model, the maximum of  $G''$  and intersection of the functions of  $\log(G')$  and  $\log(G'')$  vs.  $\log(\omega)$  always occur at the same frequency.

Fig. 4.3b gives an example of a possible structural interpretation of the mechanically observed relaxation which can be considered for molecular or colloidal systems. For a dense system of spheres which can be regarded as representing molecules or particles there is a solid-like state at higher and a liquid-like state at low frequencies. In the high frequency regime, they indicate only vibrational motions and quasi localized positions of particles between the neighbors, whereas, at low frequencies displacements exceeding particle sizes make the system viscous - changing neighbors becomes possible. According to such a model, the relaxation is related to the position correlation of particles and the mechanical response can be considered as a Fourier transform of the position autocorrelation function with the characteristic relaxation time necessary for particles to escape from the surroundings of the initial neighbors.

#### 4.2.2.2 Non-linear viscoelastic behavior

In non-linear viscoelastic materials increasing deformation amplitude, i.e. finite strain at a constant frequency leads to structural changes, for example, chain orientation and extension, which influence the material properties. In such cases, the stress-response becomes non-sinusoidal, therefore the property definitions for  $G'$ ,  $G''$  and  $\delta$  are not meaningful for such a response (Jeffrey Giacomini and Dealy 1993). Other methods of analysis as those discussed here are required in order to characterize such non-linear viscoelastic behavior.

#### 4.2.3 Relation of $G'$ and $G''$ to shear modulus and coefficient of viscosity

In geological literature it is common to describe the viscous and elastic behavior of rocks in terms of the coefficient of viscosity ( $\eta$ ), which relates the shear strain rate to shear stress, and the shear modulus ( $G$ ), which relates elastic shear strain to shear stress.

$$\eta = \frac{\sigma(t)}{\dot{\gamma}} \quad (4.9)$$

$$G = \frac{\sigma(t)}{\gamma(t)} \quad (4.10)$$

Using the equations (4.2 - 4.7) the coefficient of viscosity  $\eta$  and the shear modulus  $G$  can be rewritten in terms of  $G'$  and  $G''$

$$\eta = \frac{G''}{\omega} \quad (4.11)$$

$$G = G' \quad (4.12)$$

The coefficient of viscosity  $\eta$  may *only* be used in ranges where the material exhibits viscous behavior ( $\tan \delta \rightarrow \infty$ ). The shear modulus  $G$  can only be used for elastic behavior ( $\tan \delta \rightarrow 0$ ). Therefore, to describe the rheological behavior of rocks *either* the viscosity *or* the shear modulus is an appropriate quantity.

#### 4.2.4 Typical rheological behavior of polymeric liquids and polymeric liquids with fillers

In complex systems like polymers, structural units of considerably different size, i.e. monomers and polymer chains relax with rates which differ by many orders of magnitude. Therefore, the observed frequency dependencies of  $G'$  and  $G''$  indicate more than one relaxation region as illustrated in Figure 4.4. This figure shows a typical example of viscoelastic behavior of a melt of a polyisoprene sample with linear chains of the molecular weight  $M_w=130000$  (Pakula et al. 1996).

The two different relaxation ranges observed for the polymer melt at low and high frequencies correspond to structural rearrangements concerning two different structural units i.e. monomers and polymers, respectively. The ranges characteristic to viscous and elastic response appear now at various deformation rates and correspond to different size scales in the examined system. Further complication of the structure, for example by introduction of fillers, can lead to creation of new structural scales and new relaxation processes with relaxation times which will depend on particle size and the structure that particles form in the matrix (Gohr et al. 1999). Such additional relaxation can shift the regions of typical deformation behavior (viscous, elastic and viscoelastic) of the material to different deformation rates.

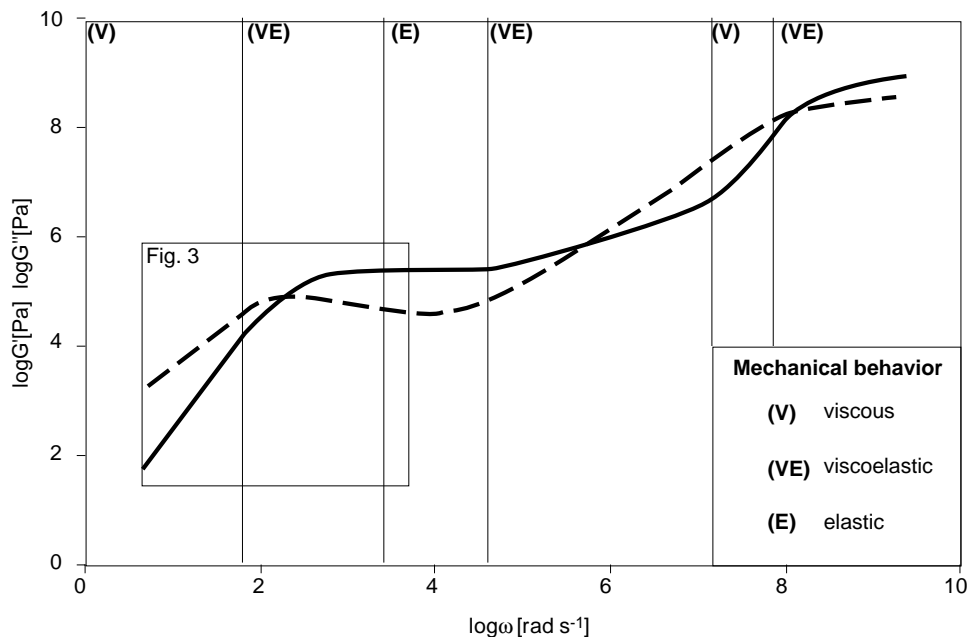


Figure 4.4. Typical example of results characterizing the viscoelastic behavior of a melt of a polyisoprene sample ( $M_w$  130000) with linear chains.



The examples given above show that details of viscoelastic and consequently rheological response of polymeric materials can be strongly influenced both qualitatively and quantitatively. In complex polymers with a broad chain length distribution or with fillers with a broad particle size distribution regions may exist where, for example,  $G'' > G'$ , the slope of  $G''$  is not equal to 1, and the viscosity is a function of the strain rate. For such behavior the relation between shear stress and strain rate is often empirically described by a power-law function.

$$\dot{\gamma} = k\sigma^n \quad (4.13)$$

where  $k$  is a constant and  $n$  the power-law index. A constant power-law index ( $n$ ) for a range of strain rates is achieved if the slopes of the functions of  $\log(G'')$  and  $\log(G')$  vs.  $\log(\omega)$  are both constant. In polymers the power-law behavior is due to specific superposition of various molecular or supramolecular relaxation processes whereas in rocks the power-law behavior is considered as associated with dislocation creep or relaxation. Hence, in polymers and rocks two structurally different mechanisms result in a similar macroscopic behavior.

### 4.3 Rheological measurements

A number of polymers that are commonly used in geological experiments have been tested. The first step in the rheological characterization of polymeric liquids and similar materials is the determination if the material is linear or non-linear viscoelastic. This is done by deriving  $G'$ ,  $G''$  and  $\eta^*$  at a constant frequency but varying applied strain. The material is linear viscoelastic only if the values of  $G'$ ,  $G''$  and  $\eta^*$  are constant in the applied strain range. The second step is to derive  $G'$ ,  $G''$  and  $\eta^*$  at a range of frequencies.

#### 4.3.1 Method

For measurements we used an oscillatory parallel-disk rheometer (Rheometric RMS 800). The rheometer cell consists of two equally sized parallel disks (Fig. 4.5) of radius  $R=6.5\text{mm}$  and the distance between the disks  $d=1.5\text{mm}$ . The sample is put between the two plates. At a given frequency of the sinusoidal strain the phase angle  $\delta$  and the amplitude of the stress response  $\sigma(t)$  are measured.

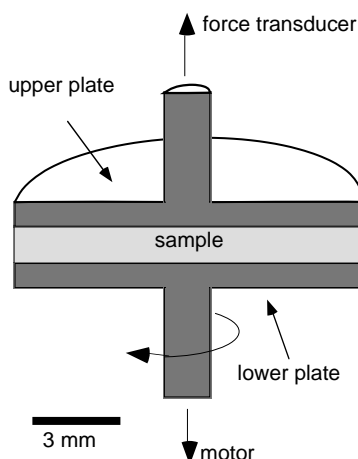


Figure 4.5. Sketch of parallel-disk rheometer geometry. The fluid (polymer) is sheared between an oscillating lower and upper disk. Strain is applied with a certain amplitude and frequency and resulting stress is measured

The rheometer has a limited range of frequencies ( $10^{-3}$  -  $10^2$  rad/s) that can be applied. To obtain values for  $G'$  and  $G''$  over a wider range of frequencies a so-called master curve is constructed. To do this, measurements are performed at different temperatures and are later shifted along the frequency scale to positions supposed as corresponding to the behavior at a chosen reference temperature  $T_{ref}$  according to

$$G'(\omega, T_{ref}) = G'(a_T \cdot \omega_m, T_m) \quad (4.14)$$

$$G''(\omega, T_{ref}) = G''(a_T \cdot \omega_m, T_m) \quad (4.15)$$

The value of the shift factor  $a_T$  is calculated with

$$\log(a_T) = \log(\omega(T_m)) - \log(\omega(T_{ref})) \quad (4.16)$$

where  $T_m$  is the temperature and  $\omega_m$  the frequency at which measurements were performed (Winter et al. 1993). The procedure works well for melts of amorphous polymers in which temperature independent structure and temperature independent relaxation spectrum can be assumed.

### 4.3.2 Results

#### 4.3.2.1 PDMS and mixtures of PDMS and BaSO<sub>4</sub>

PDMS (trade name: SGM 36; produced by Dow Corning, UK) is a transparent polymer with a density of  $965 \text{ kgm}^{-3}$  (Weijermars 1986).

To determine if PDMS is linear or non-linear viscoelastic measurement of rheological properties as a function of finite strain at constant strain rate were performed (Fig. 4.6) and revealed a linear viscoelastic flow behavior. Figure 4.7a shows the temperature dependence of the rheological properties for pure PDMS. Figure 4.7b illustrates the calculated master curve of PDMS

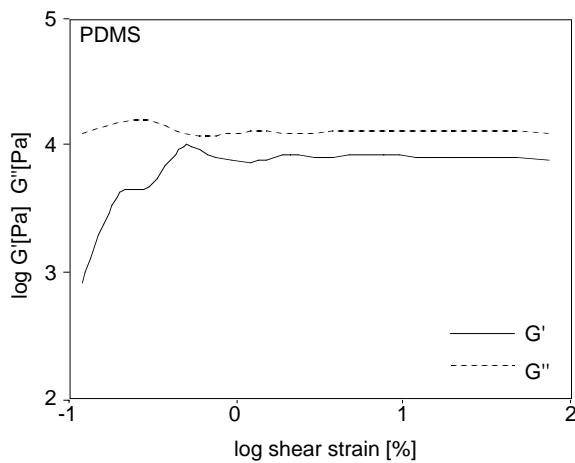


Figure 4.6. Plot of finite shear strain versus  $G'$  and  $G''$  for PDMS, confirming its linear viscoelastic flow behavior.

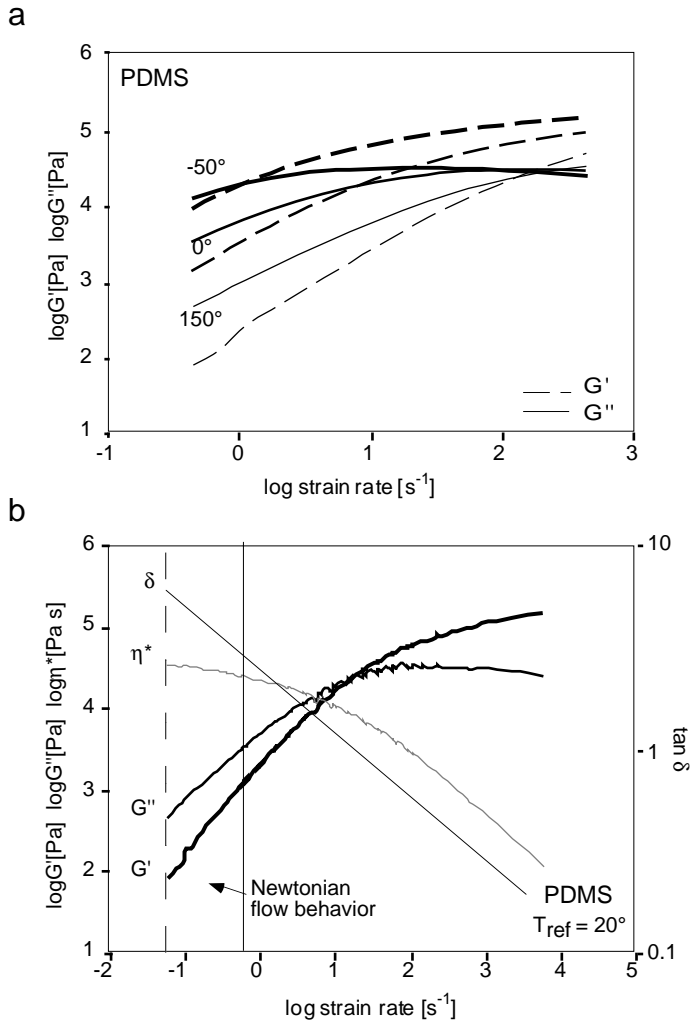


Figure 4.7. Rheological data of PDMS; a) plot of strain rate versus  $G'$  and  $G''$  measured at different temperatures; b) mastercurve for  $20^\circ C$ , showing  $G'$ ,  $G''$ ,  $\eta^*$  and  $\tan \delta$ , below a strain rate of  $0.5 s^{-1}$  PDMS shows viscous (Newtonian) flow behavior.

for a reference temperature of  $20^\circ C$ . The mastercurve for PDMS shows that at  $20^\circ C$ , at strain rates below  $5 \times 10^{-1} s^{-1}$  the slope of  $G''$  is 1 and that of  $G'$  is 2, indicating viscous flow behavior. In this range of strain rates the complex viscosity represents a meaningful value which is  $3 \times 10^4 Pa s$ . For strain rates between  $5 \times 10^{-1} s^{-1}$  and  $13 s^{-1}$   $G'' > G'$ .

Rheological data for 3 different mixtures of PDMS with the filler material  $BaSO_4$  (25 wt%, 33 wt%, 50 wt%) are given in Figure 4.8. For increasing filler content the values of  $G'$  and  $G''$  increase. For mixtures with 33 wt% and 50 wt%  $BaSO_4$   $G' > G''$  at the range of measured strain rates, indicating viscoelastic behavior with a high elastic component. The mixture with 25 wt%  $BaSO_4$  has a  $G'-G''$  crossover at a strain rate of  $16 s^{-1}$ . Below this value  $G''$  is larger than  $G'$ . Below a strain rate of  $1 s^{-1}$  the slopes of  $G'$  and  $G''$  have a constant value, indicating power-law behavior. The viscosity decreases from  $1 \times 10^5 Pa s$  at a strain rate of  $4.3 \times 10^{-2} s^{-1}$  to  $3 \times 10^4 Pa s$  at a strain rate of  $1 s^{-1}$ . This corresponds to a power-law index (n-value) of 1.23.

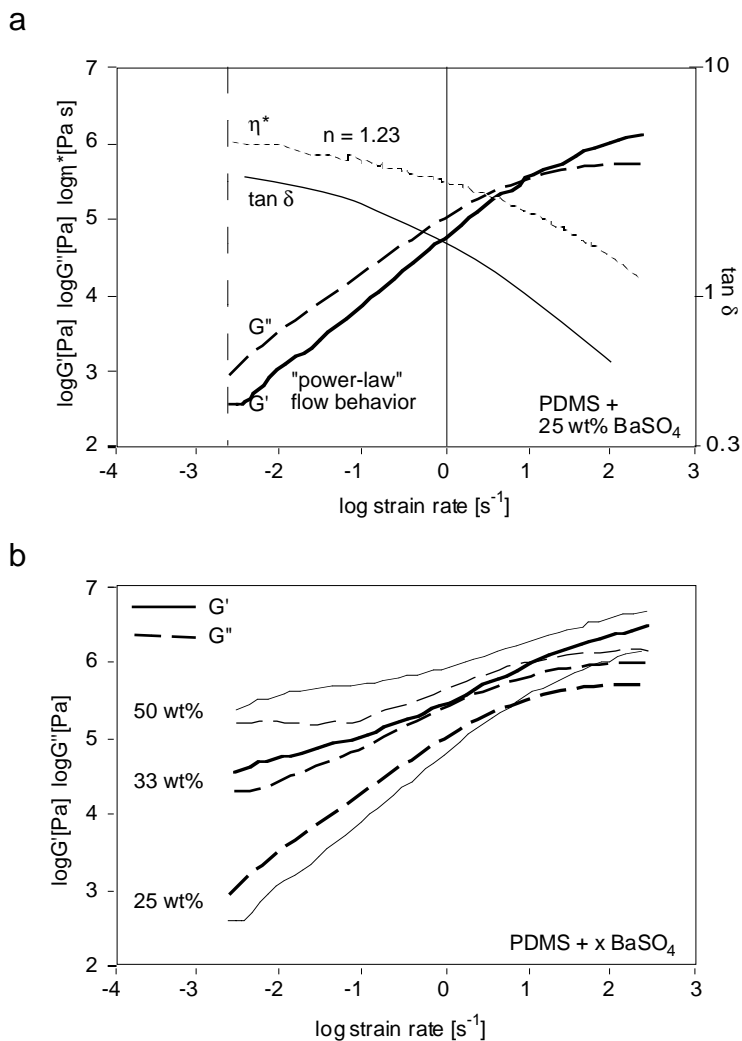


Figure 4.8. Rheological measurements of three mixtures of PDMS and BaSO<sub>4</sub>; a) results for PDMS with 25 wt% BaSO<sub>4</sub>, plot shows strain rate versus  $G'$ ,  $G''$ ,  $\eta^*$ ,  $\tan(\delta)$ . This material shows power-law behavior below a strain rate of  $16 \text{ s}^{-1}$ ; b) results for PDMS with 33 and 50 wt% BaSO<sub>4</sub>, plot shows shear strain rate versus  $G'$ ,  $G''$ . Both materials behave viscoelastic with a high elastic component.

#### 4.3.2.2 Rhodorsil Gomme

The mastercurve for Rhodorsil Gomme (pinkish opaque bouncing putty, Société des Chimiques Rhône-Poulenc (France)) at  $T_{\text{ref}}$  of 20°C is shown in Figure 4.9. Three strain rate ranges with distinctly different mechanical behavior can be distinguished. Below a strain rate of  $1 \times 10^2 \text{ s}^{-1}$  the slope of  $G''$  is 1 and that of  $G'$  is 2 and  $G'' > G'$ , i.e. the material is in the viscous behavior range. The complex viscosity  $\eta^*$  in this range is  $8 \times 10^3 \text{ Pa s}$ . Between  $1 \times 10^2 \text{ s}^{-1}$  and  $2 \times 10^3 \text{ s}^{-1}$  the slopes of both  $G'$  and  $G''$  are not constant; this is the viscoelastic range. The cross-over of  $G'$  and  $G''$  occurs at a strain rate of  $2.7 \times 10^2 \text{ s}^{-1}$ . Above a strain rate of  $2 \times 10^3 \text{ s}^{-1}$   $G'$  approaches a plateau at  $5 \times 10^5 \text{ Pa}$  in the elastic range.

#### 4.3.2.3 Mixtures Rhodorsil Gomme and white plastilina

Figure 4.10 depicts strain percentage versus  $G'$  and  $G''$  at different frequencies for 2 different mixtures of white plasticine (PI; Swedish version of Harebutt's Plasticine (McClay 1976)) and Rhodorsil Gomme (RG) (32wt% PI/68wt% RG, 50wt% PI/50wt% RG, 75wt% PI/25wt% RG). The mixture of 32wt% PI/68wt% RG exhibits constant values of  $G'$  and  $G''$  with increasing finite strain, thus this mixture is linear viscoelastic. Figure 4.11 depicts the corresponding mastercurve. Below a strain rate of  $26 \text{ s}^{-1}$  the slopes of  $G''$  and  $G'$  are constant, but not equal to 1 and 2, respectively. The calculated  $n$ -value assuming power law flow is 1.25. Above a strain rate of  $5 \times 10^3 \text{ s}^{-1}$  the mechanical behavior is elastic. For mixtures of 50wt% PI/50wt% RG and 75wt% PI/25wt% RG values of  $G'$  and  $G''$  are not constant with increasing finite strain and therefore the material is non-linear viscoelastic.

#### 4.3.3 Comparison of results with existing data

Our data for PDMS closely resemble those given by Weijermars (1986) (Fig. 4.12) and confirm a Newtonian flow behavior below a strain rate of around  $5 \times 10^{-1} \text{ s}^{-1}$  at room temperature (20-25°C). Between strain rates of  $2 \times 10^{-1} \text{ s}^{-1}$  and  $13 \text{ s}^{-1}$  the flow behavior is viscoelastic, whereby  $G'' > G'$ . Above a strain rate of  $13 \text{ s}^{-1}$  no viscous flow is present as  $G' > G''$ . Our data additionally show that the mechanical behavior of PDMS changes significantly with temperature (Fig. 4.7). Treagus and Sokoutis (1992) measured the viscosity of PDMS mixed with 23wt%  $\text{BaSO}_4$  at strain rates between  $6 \times 10^{-3} \text{ s}^{-1}$  and  $1 \times 10^{-1} \text{ s}^{-1}$  (Fig. 4.12). Their finding of a non-Newtonian flow behavior for this mixture is confirmed by our data for a mixture of PDMS and 25wt%  $\text{BaSO}_4$ . The power-law index ( $n$ ) for the mixture with 25 wt%  $\text{BaSO}_4$  is 1.23, which is slightly above the  $n$ -value of 1.1 for the mixture investigated by Treagus and Sokoutis (1992).

Viscosity measurements of Rhodorsil Gomme have been performed by Weijermars (1986) and Sokoutis (1987) (Fig. 4.12). Our data for Rhodorsil Gomme confirm the Newtonian flow behavior below a strain rate of  $1 \times 10^2 \text{ s}^{-1}$ , as concluded from these measurements. The viscosity determined from our data is  $8 \times 10^3 \text{ Pa s}$ , in contrast to the value of  $3 \times 10^4 \text{ Pa s}$  from earlier measurements (Weijermars 1986, Sokoutis 1987). Above a strain rate of  $1 \times 10^2 \text{ s}^{-1}$  the material shows viscoelastic behavior and above  $2 \times 10^3 \text{ s}^{-1}$  elastic behavior. Earlier measurements were not performed in the latter range.

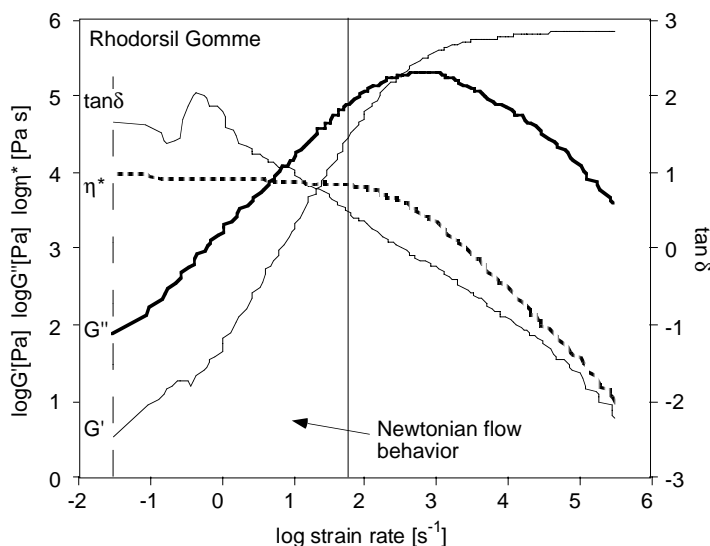


Figure 4.9. Mastercurve of Rhodorsil Gomme, showing  $G'$ ,  $G''$ ,  $\eta^*$  and  $\tan \delta$  versus strain rate. Rhodorsil Gomme behaves viscously below a strain rate of  $1 \times 10^2 \text{ s}^{-1}$ .

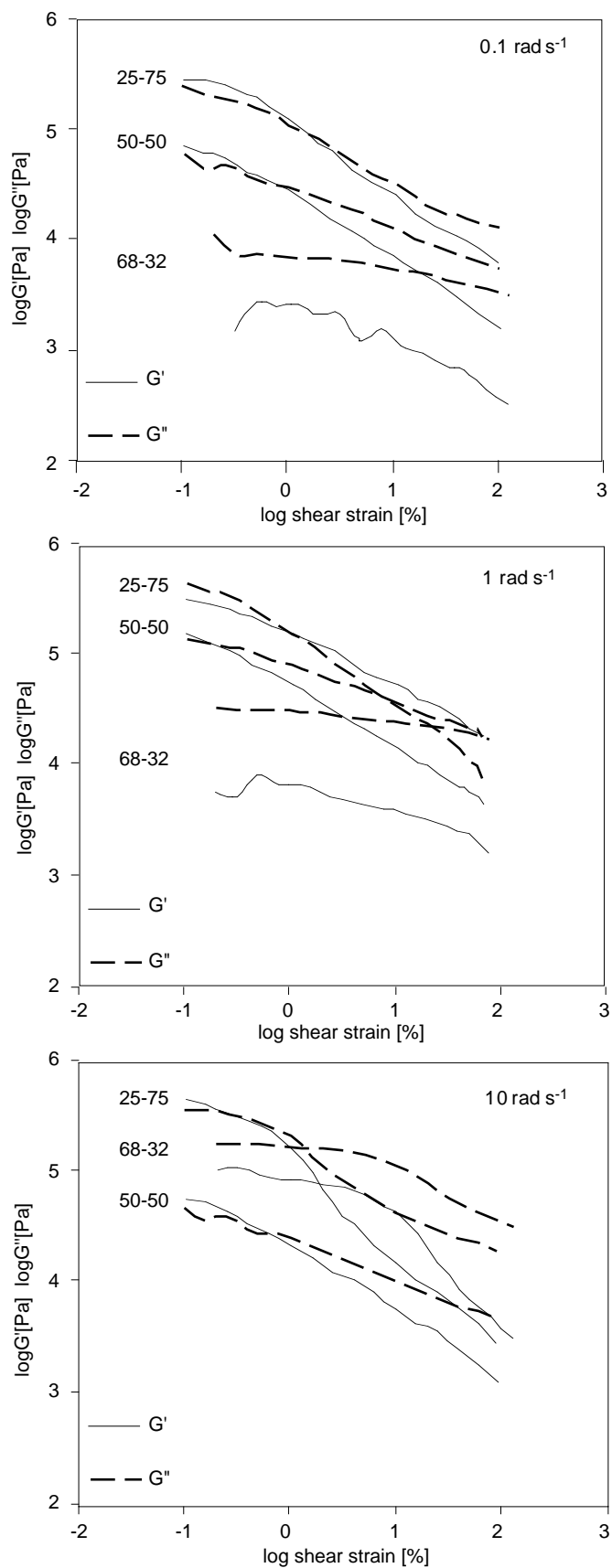


Figure 4.10. Variation of  $G'$  and  $G''$  with shear strain showing the non-linear, strain-dependent viscoelastic behavior of mixtures of plasicine and Rhodorsil Gomme, 25-75, 50-50 and 68-32 are the weight ratios of Rhodorsil Gomme and plasicine.

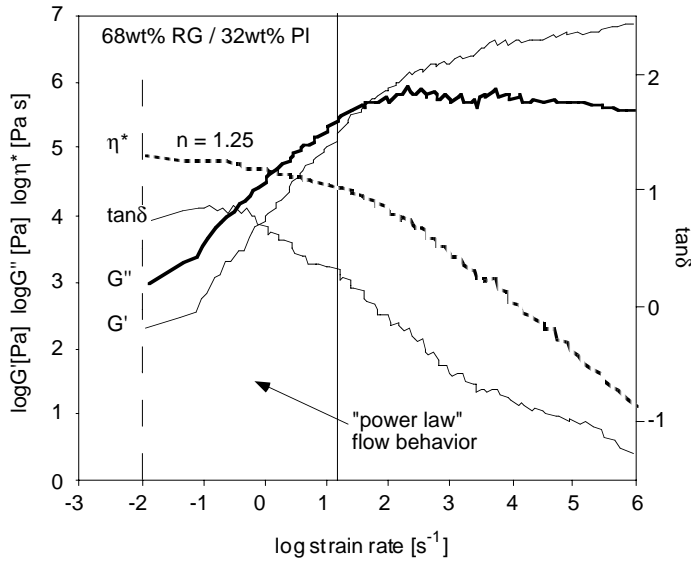


Figure 4.11. Mastercurve of the mixture of 32 wt% Plastilina and 68 wt%, Rhodorsil Gomme, showing  $G'$ ,  $G''$ ,  $\eta^*$  and  $\tan \delta$  versus strain rate. The mixture behaves like a power law material below a strain rate of  $26 \text{ s}^{-1}$ .

Our data for mixtures of white plasticine and Rhodorsil Gomme do not confirm comparable data of Weijermars (1986) and Sokoutis (1987). Our findings show that these materials are non-linear viscoelastic (Fig. 4.10), and therefore viscosity is not a meaningful rheological property.

McClay (1976) and Kobberger and Zulauf (1995) measured the rheological properties of several types of plasticine and a mixture of plasticine and oil using a uniaxial compression apparatus. They investigated the response of the different materials at constant strain rate and a range of finite strains and used measured values only at a finite strain at which a constant stress response was seen to derive the power-law exponent of the materials. With this procedure they assured linear viscoelastic behavior of the investigated materials. Therefore, the derived power-law exponents are meaningful for the specific range of strain percentage. Dixon and Summers (1985, 1986) investigated the rheological properties of a silicon putty with an annular shear rig. The plots (Fig. 4.10; Dixon and Summers 1985) of time versus shear strain clearly show the time-dependent response of the material and therefore the significance of the elastic component in the rheological behavior of the material. Nevertheless, it is not clear whether the material is linear or non-linear viscoelastic.

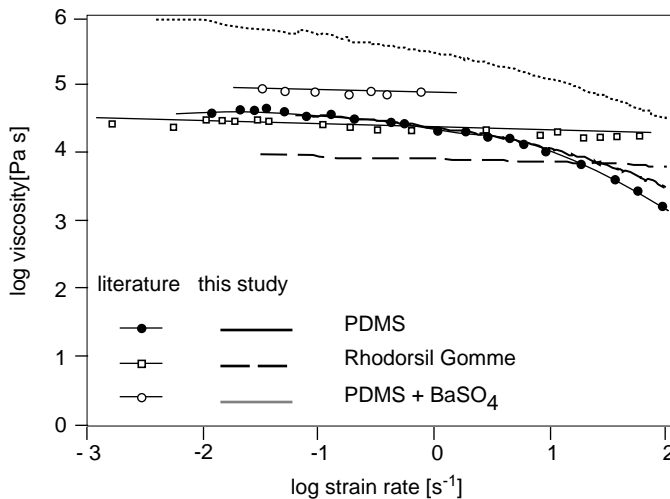


Figure 4.12. Stress-strain rate plot of existing data from literature. PDMS and Rhodorsil Gomme from Weijermars (1986) and Sokoutis (1987), PDMS with 23 wt%  $\text{BaSO}_4$  from Treagus and Sokoutis (1992) and the data for PDMS, Rhodorsil Gomme and PDMS with 25 wt%  $\text{BaSO}_4$  from this study.

Weijermars (1986) measured the viscosity of several mixtures of Rhodorsil Gomme and BaSO<sub>4</sub> with different ratios of the filler to matrix. The purpose of this work was a) to derive power-law exponents for the different mixtures and b) a function to predict the power-law exponent of mixtures of Newtonian polymers and filler material. As shown by our data for mixtures of PDMS and BaSO<sub>4</sub> (Fig. 4.8) mixtures with a filler content of 33 and 50 wt% are characterized by higher storage moduli than loss moduli. Therefore, mixtures of polymeric liquids and fillers do not necessarily flow viscously. If  $G' > G''$  derived power-law exponents are meaningless. Hence, the general function given by Weijermars (1986) should not be used.

#### **4.4 Implications for the use of polymers and related materials as rock analogs**

Analogs are used as scaled-down models of rocks. Their rheological properties should closely fit the requirements of scaling. This should not be checked only according to viscosity but by a complete rheological investigation of material properties. A modern analysis of polymers must include the determination of the storage and loss moduli.

First of all, the rheological behavior at a range of strains at a given strain rate should be known in order to determine if the material is linear or non-linear viscoelastic. If it is non-linear viscoelastic the behavior of the material strongly depends on its deformation history. Therefore, the behavior of these materials is unpredictable. If the material is linear viscoelastic the next step is to determine the values for the storage and loss moduli. The relation of these two moduli is an expression of the different types of linear viscoelastic behavior. If the value of the loss modulus is below the value of the storage modulus viscosity, measurements are not meaningful as the elastic behavior dominates. For polymers the rheological behavior is strongly dependent on strain rate and temperature. Therefore, it is necessary to know the rheological properties of a material exactly at experimental conditions.

As the rheological properties of polymers depend on the relaxation time of the structural units, mixing of polymers with different chain lengths or addition of filler may result in materials with rheological properties very different from those of the endmembers. Therefore, it should be possible to create materials with properties favorable for analog modeling of rocks.

#### **4.5 Conclusions**

The knowledge of the effective viscosity alone is not sufficient to fully describe the rheological properties of polymers and related materials. The values of the storage and loss moduli are necessary to evaluate the suitability of a polymer for analog modeling. First of all, the properties as a function of the finite strain must be known in order to determine if the material linear or non-linear viscoelastic. If the properties are not constant with increasing finite strain, a material is non-linear viscoelastic. In this case, its use as a rock-analog is problematic as the material properties (i.e. viscosity, storage and loss moduli) are a function of the deformation history. Examples for non-linear viscoelastic materials are mixtures of Rhodorsil Gomme and Plastilina used by Passchier and Sokoutis (1993), and Treagus and Sokoutis (1992) (weight percent ratio: 25/75, 50/50).



If a material is linear viscoelastic the values of the storage and loss moduli as a function of strain rate determine the mechanical behavior at specific strain rates. Three types of mechanical behavior can be distinguished:

- 1) elastic (Hookean) behavior
- 2) viscoelastic (Maxwell) behavior
- 3) viscous (Newtonian) behavior

Our results reveal that commonly used analog materials can only be used to model viscous deformation at specific strain rates. The upper limit for viscous deformation modeling is  $5 \times 10^{-1} \text{ s}^{-1}$  for PDMS and is  $1 \times 10^2 \text{ s}^{-1}$  for Rhodorsil Gomme. To model power law behavior of rocks mixtures of PDMS and  $\text{BaSO}_4$  with a  $\text{BaSO}_4$  content below approximately 30 wt% and mixtures of Rhodorsil Gomme and plastilina with a plastilina content of 32 wt% can be used at strain rates below  $1 \text{ s}^{-1}$  and  $26 \text{ s}^{-1}$ , respectively. The power law exponent (n-value) for a mixture of PDMS and  $\text{BaSO}_4$  with a  $\text{BaSO}_4$  content of 30 wt% is 1.23 and for a mixture of Rhodorsil Gomme and plastilina with a plastilina content of 32 wt% it is 1.25. For mixtures with a  $\text{BaSO}_4$  content above 30 wt% (mixture PDMS/ $\text{BaSO}_4$ ) the elastic component dominates.

These results show that exclusive measurements of viscosity are not sufficient to determine the mechanical behavior of a material and therefore to assess its suitability for specific analog modeling requirements.



## Chapter 5

# The influence of strain localisation on the rotation behaviour of rigid objects in experimental shear zones

### Abstract

Mica fish and tourmaline fish were analysed in thin section to determine their orientation distribution. They are oriented with their long axes tilted with respect to the mylonitic foliation, where fish with a small aspect ratio exhibit a slightly larger angle as fish with a large aspect ratio. This orientation seems to be a stable orientation for the mica and tourmaline fish. Analogue experiments with two rheologically different matrix materials are performed to explain the data. One material is PDMS, a linear viscous polymer. The other is tapioca pearls, a granular material with low cohesion and Mohr-Coulomb type behaviour. In contrast to a fairly homogeneous strain distribution in PDMS, distinct small-scale shear bands develop in tapioca pearls during deformation. Experiments model different vorticity numbers, and parallelogram-shaped rigid objects with different aspect ratios are used. Rotation rates of objects in a viscous matrix are very similar to analytical solutions for ellipses in viscous flow, but stable orientations differ from data of natural examples. In all experiments with a Mohr-Coulomb matrix elongated objects have a stable orientation due to strain localisation. We therefore suggest that strain localisation is an important characteristic of the rheology of mylonites.

### 5.1 Introduction

Mylonitic rocks usually contain porphyroclasts that can develop into shear sense indicators such as sigma and delta clasts or lenticular structures such as mica fish (White et al. 1980, Simpson and Schmid 1983, Lister and Snoke 1984, Passchier and Simpson 1986, Hanmer and Passchier 1991, Passchier and Trouw, 1996). The understanding of these structures is essential for the correct interpretation of the flow kinematics in mylonites with porphyroclasts.

To gain better understanding of the behaviour of porphyroclasts in mylonites, analytical and experimental studies have investigated the behaviour of single or multiple objects or inclusions in a homogeneous viscous matrix. The rheology of a deforming mylonite is usually described as non-linear viscous, with a power-law relationship between strain rate and stress (Kirby and Kronenberg 1987). Although the stress exponent,  $n$ , which defines the sensitivity of strain rate to stress is usually assumed to be 1-3 in mylonites, most modelling studies on porphyroclast behaviour assumed linear (Newtonian) viscous behaviour with  $n = 1$ . Jeffery's (1922) work shows that the rotation rate of an elliptical object in simple shear is a function of the strain rate, and of the aspect ratio and orientation of the object. Solutions for pure shear flow (Gay 1968) and combinations of pure and simple shear, general flow (Ghosh and Ramberg 1976), have also been proposed. This early work has been extended to the motion of rigid particles in non-

Newtonian fluids by Ferguson (1979) and to triaxial elliptical particles by Jezek et al. (1994). According to the equations for rigid elliptical particles in a Newtonian viscous fluid all objects, except lines and planes rotate continuously in simple shear. Elongated objects have a pulsating rotation rate under these conditions. In plane strain general flow with kinematic vorticity number ( $W_k$ , Means et al. 1980) between 0 and 1, elliptical objects rotate towards a stable orientation, if their aspect ratio exceeds a critical value ( $R_{crit}$ ).  $R_{crit}$  is a function of the kinematic vorticity number ( $W_k$ ):

$$R_{crit} = \sqrt{(1 + W_k)/(1 - W_k)}$$

(Ghosh and Ramberg 1976, Passchier 1987). Objects with a lower aspect ratio rotate continuously, but with a pulsating rotation rate. In simple shear ( $R_{crit} = \infty$ ) there are no stable orientations except for lines and planes. In pure shear ( $R_{crit} = 1$ ) all objects rotate towards a stable position, and spheres are stationary.

In analogue experiments and numerical modelling several aspects of the deformation of porphyroclast systems have been studied. For the behaviour of rigid objects in a ductile matrix different materials have been used as an analogue for the matrix, such as silicon putty (e.g. Ghosh and Ramberg 1976, Ildefonse et al. 1992), honey with titanium oxide (Fernandez et al. 1983), paraffin wax (Ildefonse and Mancktelow 1993) and octachloropropane (OCP), polyacrylamide (pAA) solution, and glycerine (Ten Brink 1996). These experiments modelled either simple or pure shear flow and rigid object were usually rectangular. Results from these experiments show that for most matrix materials the embedded rectangular particles behave as predicted for elliptical particles with a similar aspect ratio by the analytical solutions mentioned above. In the case of a non-coherent boundary (Ildefonse and Mancktelow 1993) and for experiments with a non-Newtonian anisotropic viscous matrix material (OCP and pAA solution, ten Brink 1996) the results differ from these analytical solutions. These results indicate that the rheological properties of the matrix are an important factor for the behaviour of porphyroclasts. Numerical models mainly concentrate on the flow perturbation around a rigid particle (Bons et al. 1997, Pennacchioni et al. 2000). All the above models predict that after large strains, most objects in a population are orientated close to their stable slow rotation orientation. Vorticity analysis, based on the orientation distribution of particles in a natural shear zone were done by several authors, e.g. Passchier (1987), Jezek et al. (1994), and Masuda et al. (1995). Masuda et al. (1995) made distribution plots of aspect ratio versus orientation for initially randomly distributed particles in plane strain flow after different amounts of finite strain, to predict both vorticity number of flow and finite strain in mylonites.

Bell (1985) proposed a contrasting theory on the behaviour of rigid objects in a shear zone. He suggested that non-coaxial deformation partitions into zones of nearly coaxial deformation and zones of generally non-coaxial shearing. Porphyroblasts and porphyroclasts would lie within coaxial deformation zones and would rotate little or not at all with respect to bulk flow axes.

In this study attention is paid to the behaviour of objects with a parallelogram shape in simple shear and combinations of pure and simple shear. In natural shear zones objects with a parallelogram or lenticular shape are common as so-called mica fish, usually composed of muscovite or biotite (Eisbacher 1970, Fig. 5.1). Similar structures can also be formed by other

minerals, such as garnet (Azor et al 1997) and tourmaline (Fig. 5.1). From observations on natural mica fish by Eisbacher (1970) and Lister and Snoke (1984) it is known that mica fish all have a similar orientation, with their long axis tilted with respect to the flow plane. This suggests that they rotated towards a stable orientation. This orientation is different from the stable or slow rotation rate orientation of elongate rigid objects predicted by theory and observed in experiments with rigid ellipsoids. We tried to investigate how the orientation of these structures can be explained and what this tells us about the flow kinematics and rheology in ductile shear zones. The shape and orientations of mica and tourmaline fish from three different localities are described and the observed geometries and orientations were used as a basis to perform a number of analogue experiments.

## 5.2 Measurements of natural samples

Two sets of mica fish and one set of tourmaline fish were analysed in thin section to determine their orientation distribution. The first set are isolated muscovite fish within pure quartzites from a shear zone near Conceição do Rio Verde, Southern Minas Gerais State, Brazil (Trouw et al. 1983). The quartzites belong to the lower unit of the Neoproterozoic Andrelândia Depositional Sequence (Paciullo et al. 1993, Ribeiro et al. 1995). The outcrop (Locality 45°06' E, 21°56'S, Chapter 2) is situated in an ENE trending subvertical dextral shear zone of about 500 m thickness. The metamorphic grade during deformation is estimated as upper greenschist facies. In 3D the mica fish have a flake or disc shape. In the plane parallel to the stretching lineation and perpendicular to the foliation the mica fish are elongated and have a parallelogram or lenticular shape (Fig. 5.1a & b).

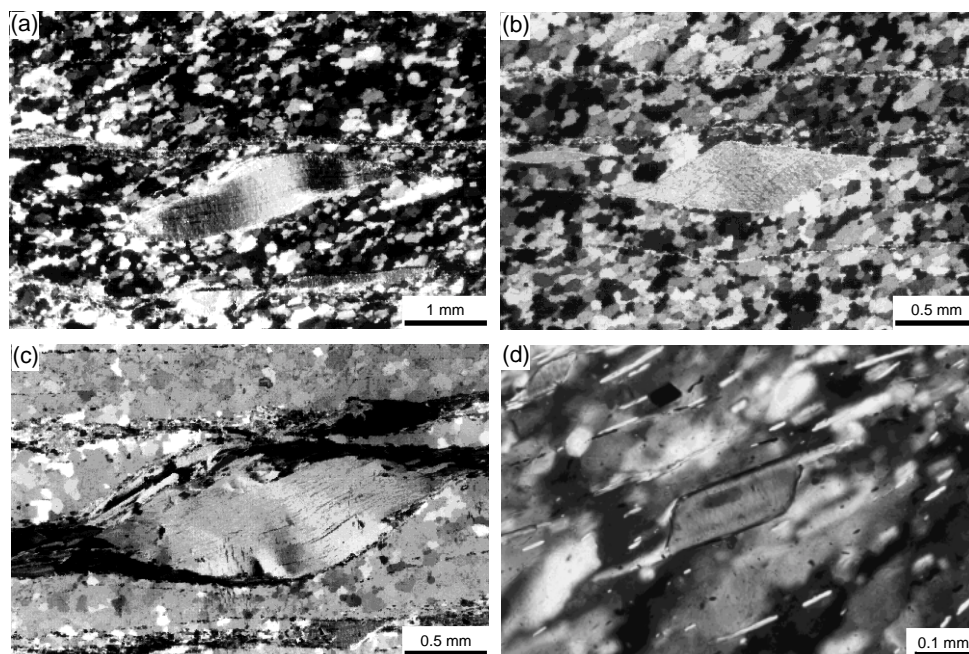


Figure 5.1. Photomicrographs of mica and tourmaline fish in thin sections parallel to stretching lineation and perpendicular to foliation. Shear sense is dextral in all pictures. a) Lenticular shaped muscovite fish from Conceição do Rio Verde, Brazil. b) Parallelogram shaped muscovite fish from Conceição do Rio Verde, Brazil. c) Lenticular biotite fish from Santa Rosa Mylonite zone, California, U.S.A. d) Parallelogram shaped tourmaline fish from Lambari, Brazil.

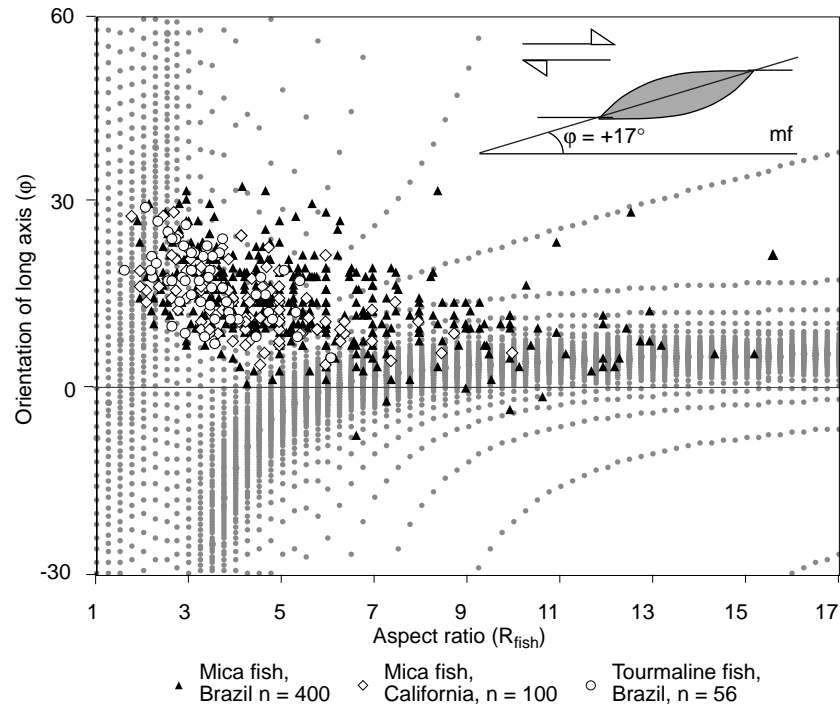


Figure 5.2. Plot of the orientation of long axis with respect to aspect ratio (long axis/short axis) of mica and tourmaline fish. Small grey dots show the distribution pattern of initially homogeneously distributed ellipses for simple shear after a shear strain of  $\gamma = 10$ , according to the solutions of Jeffery (1922) (after Masuda et al. (1995)). Inset shows definition of  $\phi$  and the sign convention used throughout this paper.

The aspect ratio ( $R_{\text{fish}} = \text{longest axis/shortest axis}$ ) of the fish in this plane is between 2 and 16, with an average of 5.7 (Fig. 5.2). Trails of very small mica fragments extend from the tips of the mica fish into the matrix. These 10-100  $\mu\text{m}$  wide trails define the mylonitic foliation. The matrix surrounding the mica fish consists of fine-grained quartz with a crystallographic preferred orientation (CPO) and an oblique shape foliation (Means 1981), which makes an angle of  $34^\circ$  with the mylonitic foliation. The mica fish are inclined to the mylonitic foliation in the same direction as the oblique foliation. The angle ( $\phi$ ) between the long axes of 400 measured mica fish and the mylonitic foliation has a median value of  $13^\circ$  (Fig. 5.2).

The second set of samples comes from the Santa Rosa mylonite zone, Palm Canyon, California. The mica fish are developed in mylonitized granodiorites, which are present in a 700-900 m thick sequence of mylonites in Palm Canyon (Wenk and Pannetier 1990). The movement related with these mylonites is a thrust system and deformation occurred at middle amphibolite facies conditions (Simpson 1984, Wenk and Pannetier, 1990, Goodwin and Wenk 1995). The matrix of these mylonites is composed of quartz with a clear CPO. The mica fish from this location are muscovite as well as biotite fish. Both minerals show lenticular shapes (Fig. 5.1c). One hundred mica fish (31 muscovite & 69 biotite) were measured (Fig. 5.2). The aspect ratio of these fish is between  $R_{\text{fish}} = 2$  and 10, with an average of 4.3. The mica fish from this shear zone are also orientated with their long axis inclined with respect to the mylonitic foliation. The median value of  $\phi$  for this shear zone is  $12^\circ$  for the biotite fish and  $15^\circ$  for the muscovite fish.

The third set of studied samples contains tourmaline fish (Fig. 5.1d). These samples are from a shear zone near Lambari, Southern Minas Gerais State, Brazil (Trouw et al. 1983) in the Andrelândia Depositional Sequence (Paciullo et al. 1993, Ribeiro et al. 1995). Deformation in these samples occurred under middle amphibolite facies conditions. The matrix consists of fine-grained quartz with a clear CPO. In contrast to the more smooth mica fish the tourmaline fish have an angular parallelogram shape with straight sides and typically have an angle of about  $50\text{--}55^\circ$  between the sides (Fig. 5.1d). Their long side is usually parallel to the mylonitic foliation. The aspect ratio  $R_{\text{fish}} = 1.5 - 6$ . The orientation of the long axes of the tourmaline crystals has a median value of  $17^\circ$  (Fig. 5.2).

The data from each location show a similar trend, a slightly higher angle for the fish with a small aspect ratio and lower angle for fish with a high aspect ratio. None off the distribution plots of aspect ratio with respect to orientation of rigid ellipsoids of Masuda et al. (1995) resemble the pattern observed in figure 5.2. For comparison the distribution pattern of the longest axes of initially homogeneously distributed ellipses for simple shear after a shear strain of  $\gamma = 10$  is plotted (Fig. 5.2). Lister and Snoke (1984) suggested that inhomogeneous flow of the matrix might play a role in mylonites containing mica fish. Observation of boudinaged mica fish, linked by fine-grained mica trails could be taken as evidence that part of the deformation is accommodated in narrow zones in the investigated mylonites, as in the case of S-C mylonites (Berthé et al. 1979, Lister and Snoke 1984). However, such mylonites normally show no decrease in grain size, change in crystallographic preferred orientation or other signs of enhanced strain towards the trails of mica grains. Also, these trails are normally parallel without the anastomosing geometry seen in many ductile shear zones with flow partitioning. Therefore these trails could also represent the trace of the finite strain ellipsoid. Clearly, the orientation of the mica fish is a crucial feature. We therefore carried out two sets of experiments with opposite rheological matrix properties to see which one could mimic the observed object orientations: one with a homogeneous viscous material and one with extreme flow localisation.

## 5.3 Experimental Method

### 5.3.1 The apparatus

The experiments were performed with a deformation apparatus that can model deformation in general flow regimes (Chapter 3). The apparatus consists of a four-sided deformation box, with walls constructed from 1 cm wide, 12 cm high Plexiglas segments, which are connected with flexible plastic (Fig. 5.3). The segments are connected at the outside to two metal springs. This construction ensures homogeneous contraction and extension of the walls. Two opposing sides of the deformation box, consisting of 30 segments, are always parallel to the x-direction of the x, y, z-reference frame of the apparatus (Fig. 5.3). The two other sides, made with 20 segments, can rotate about the z-axis. A 0.35 mm thick elastic latex sheet forms the bottom of the deformation box. This construction results in a deformation box that slides with low friction on the base plate and which is open at the top. The contraction or extension of the flexible sides of the deformation box is controlled by six stepping motors. This set-up allows all types of monoclinic flow to be modelled. Boundary effects extend 10-15 mm into the matrix from the walls (Chapter 3). Velocity of the motors is controlled by the computer program LabView<sup>®</sup>.

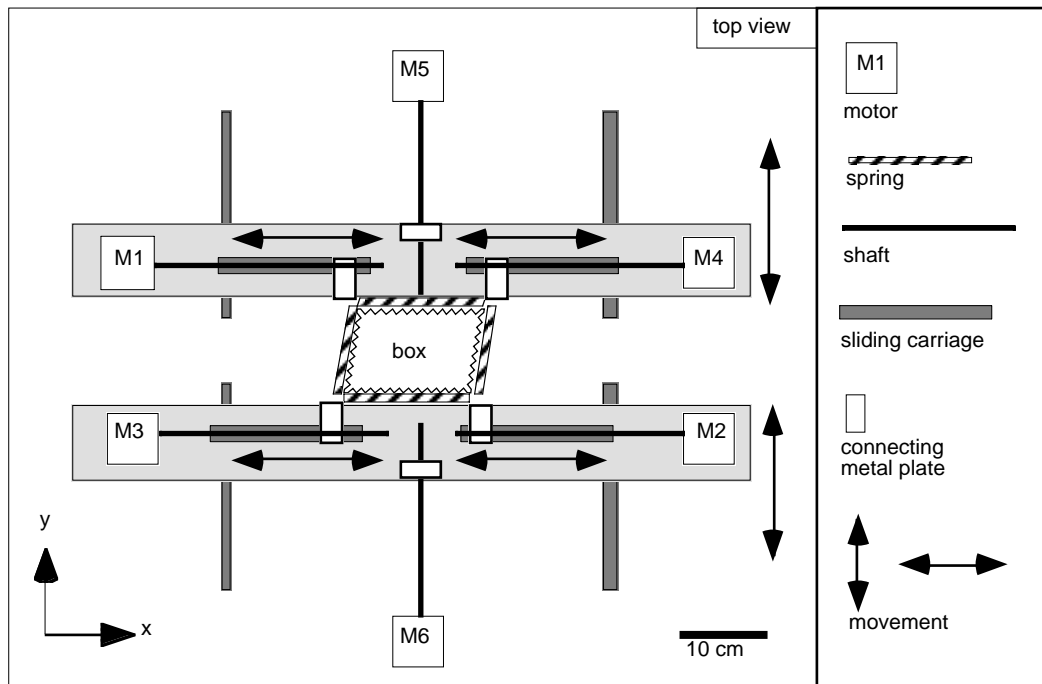


Figure 5.3. Schematic drawing of deformation apparatus, seen from top. The sides of the box can be independently moved by the six motors to create any type of bulk monoclinic flow.

### 5.3.2 Experimental procedure

Experiments were carried out in dextral plane strain progressive deformation, also known as subsimple shear (Simpson and De Paor 1993) or stretching shear zone geometry (Passchier 1998). The kinematic vorticity number values of deformation modelled in the experiments were 1 (simple shear), 0.95, 0.8 and 0.6. Two different analogue matrix materials were used. (1) PDMS (polydimethylsiloxane, trade name SGM 36, produced by Dow Corning, UK), a transparent Newtonian viscous polymer with viscosity  $5.0 \times 10^4$  Pa·s at room temperature and a density of  $0.97 \text{ g/cm}^3$  (Weijermars 1986). (2) As an analogue with extreme flow localisation we searched for a material with semi-brittle behaviour and low cohesion. Sand would have been suitable, except for its high density. We settled for densely packed tapioca pearls, approximately equidimensional spheres with a cross section of  $2.0 \pm 0.4 \text{ mm}$ . The tapioca pearls show Mohr-Coulomb type behaviour similar to sand, but with a low cohesion that is suitable for the deformation apparatus. The coefficient of internal friction,  $\mu$ , and cohesion,  $C_0$ , for fault initiation in tapioca pearls are:  $\mu = 0.74 \pm 0.05$  and  $C_0 = 39 \pm 44 \text{ Pa}$  (Appendix A).

Rigid blocks of India Rubber with a density of  $1.46 \text{ g/cm}^3$  are used as analogue for the mica and tourmaline fish. The objects are always placed with their flat top side parallel to the base plane (xy-plane) of the apparatus. In the xy-plane the objects had two principal shapes, parallelogram shape and square ( $R_{ob} = 1$ ), (Fig. 5.4). Parallelogram shapes in the xy-plane were used to resemble natural mica and tourmaline fish. The angle between the sides was  $45^\circ$  and length width ratios ( $R_{ob}$ ) were 3, 4, 6, and 10 (Fig. 5.4). The square object ( $R_{ob} = 1$ ) was used for reference. The major and minor axis of the object in the xy-plane are referred to as the a-axis and b-axis (Fig. 5.4, Table 5.1). The c-axis of the object is always parallel to the z-axis of



Table 5.1. Dimensions of the objects. \*Sharp angle between the sides of the object.

Particle name	A (mm)	b (mm)	c (mm)	Angle *
3	22.5	7.5	24.0	45°
4	22.0	5.5	33.0	45°
6	27.5	4.5	21.5	45°
10	35.0	3.5	21.5	45°
1rect	20.5	20.5	41.0	90°

the apparatus. According to the analytical equations of Jeffery (1922), only the ratio between the a- and b-axis is important for the behaviour of the object in this orientation. The orientation of the a-axis of the objects ( $\varphi$ ) is measured with respect to the x-direction of the apparatus. Objects were placed with their long axis perpendicular to the x-direction ( $\varphi = 90^\circ$ ) or parallel to the x-direction ( $\varphi = 0^\circ$ ) at the start of the first run of each experiment. Table 5.2 gives an overview of the performed experiments with the used strain rate (experiments with  $W_k = 1$ ) or stretching rates ( $W_k < 1$ ).

The finite strain that can be reached in the apparatus is limited to  $\gamma = 3$  for  $W_k = 1$  and to a stretch of 150% along the x-axis for  $W_k < 1$ . Higher strains were achieved by running series of experiments (Passchier and Simpson 1986). After each experimental run the precise orientation of the object was photographed and measured. After returning the box to the starting position the object was placed in the measured final orientation and another experimental run under the same conditions as the previous run was carried out. This technique is particularly useful when studying one or a few rigid objects. Experiments presented here were run until the object stopped rotating for at least a strain of  $\gamma = 0.5$  or stretch along x-axis of 105%, or had rotated a full  $180^\circ$ . Images of the sample were taken with a digital camera with a resolution of 800 by 600 pixels. The orientation of the objects was measured with the program NIH image; the accuracy of measured orientation is  $0.5^\circ$ . We present the orientation of the object ( $\varphi$ ) as a function of the simple shear component of deformation ( $\gamma$ ) rather than strain ratio  $R_f$ . This is done for two reasons: a) the equations given by Ghosh and Ramberg (1976) give the orientation as a function of the simple shear component of deformation and b) this component increases in a linear way with time at constant vorticity number and strain rate, unlike the strain ratio ( $R_f$ ).

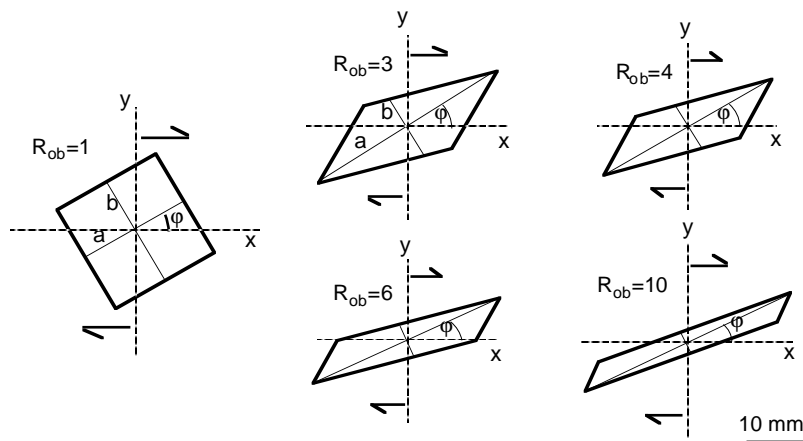


Figure 5.4. Schematic drawing of the rigid objects used in the experiments, with angles used to describe their orientation ( $\varphi$ ).

Table 5.2. List of performed experiments: \* TP = tapioca pearls

Vorticity number ( $W_k$ )	Matrix material	$R_{ob}$ of studied objects, starting orientation $\varphi_0 = 90^\circ$	$R_{ob}$ of studied objects, starting orientation $\varphi_0 = 0^\circ$	Strain rate ( $W_k=1$ ) or stretching rate ( $W_k < 1$ ) ( $s^{-1}$ )
1	PDMS	1rect, 3, 4, 6		$2 \cdot 10^{-3}$
1	TP*	1rect, 3, 4, 6, 10	4	$2 \cdot 10^{-3}$
0.95	TP	3, 4, 6, 10	3,6	$3.3 \cdot 10^{-4}$
0.8	PDMS	3, 4, 6		$3.3 \cdot 10^{-4}$
0.8	TP	3, 4, 6, 10	10	$3.3 \cdot 10^{-4}$
0.6	TP	3, 4, 6, 10	4	$3.3 \cdot 10^{-4}$

## 5.4 Results of the experiments

### 5.4.1 Orientation of objects

The results for the simple shear experiments with the square object ( $R_{ob} = 1$ ) in PDMS and tapioca pearls matrices are shown in figure 5.5. The rotation rate of the object in PDMS is constant and similar to the rate predicted by theoretical solutions. In tapioca pearls the object is also continuously rotating, but at a lower rate as in PDMS, and the rotation rate is not constant. The minimum and maximum rotation rates in tapioca pearls are reached when the object has an orientation of  $\varphi = 65-75^\circ$  and  $\varphi = 20-30^\circ$ , respectively.

Figure 5.6 shows the results of the experiments with elongate objects in PDMS for a vorticity number of 1 (simple shear) and 0.8. In simple shear ( $W_k = 1$ ) the rotation rate of the objects has a minimum and maximum when their long axis is orientated at  $\varphi = 0^\circ$  and  $\varphi = 90^\circ$  respectively. For objects with  $R_{ob} = 3$  and 4 the curves are very similar to the analytical solution for ellipsoids with the same aspect ratio. For  $R_{ob} = 6$ , the analytical solution for an ellipse with a

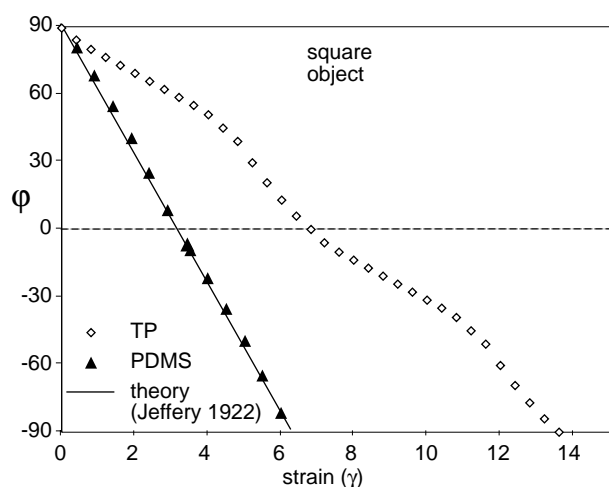


Figure 5.5. Object orientation ( $\varphi$ ) versus strain for experiments with a square object with two different matrix materials. Solid thick line indicates expected orientation of the object according to analytical solutions of Jeffery (1922) for a circular object.

Table 5.3. Stable orientations ( $\varphi$ ) of the particles, -: object does not have a stable orientation under these conditions

Object ( $R_{ob}$ )	PDMS		Tapioca pearls			
	$W_k = 1$	$W_k = 0.8$	$W_k = 1$	$W_k = 0.95$	$W_k = 0.8$	$W_k = 0.6$
3	-	-5.6	24.4	2.9	10.7	10.8
4	-	-4.4	16.7	8.8	13.5	10.8
6	-	-4.4	14.4	4.9	14.4	12.4
10	-	-	11.8	0.4	8.7	12.1
1rect	-	-	-	-	-	-

slightly smaller aspect ratio ( $R_{ob} = 5.6$ ) fits better. In experiments with vorticity number 0.8 all objects reach a semi-stable orientation with a small negative  $\varphi$ -value (Table 5.3) as predicted by Ghosh and Ramberg (1976). Objects with  $R_{ob} = 3, 4$  and 6 closely follow the rotation rates predicted by analytical solutions for  $W_k = 0.8$ .

Figure 5.7 shows the results for experiments with non-square objects in a matrix of tapioca pearls for  $W_k = 1$  (simple shear). From a starting orientation of  $\varphi_0 = 90^\circ$ , all objects rotated clockwise in the dextral shear. Their rotation rate decreased with increasing finite strain to reach a stable orientation, which is different for each aspect ratio. In all cases this orientation is at a positive angle ( $\varphi > 0$ ). These results are completely different from the analytical solutions given by Ghosh and Ramberg (1976) for an elliptical object in simple shear. One experiment with  $\varphi_0 = 0^\circ$  was performed for the monoclinic object with  $R_{ob} = 4$  to check if this angle is a stable or a semi-stable orientation. In this case the object started to rotate *counterclockwise* and

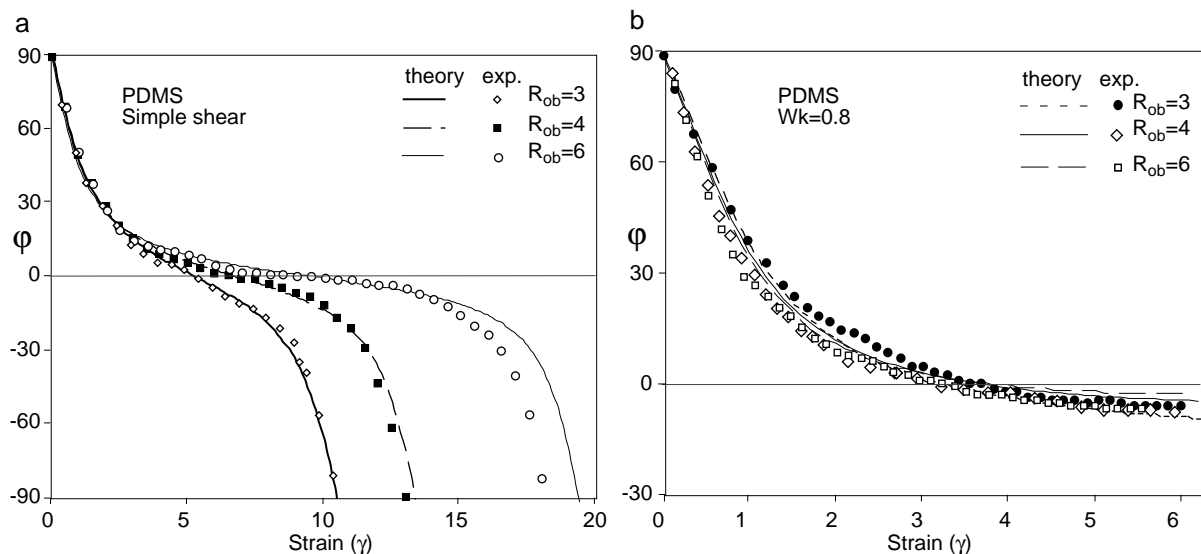


Figure 5.6. Object orientation ( $\varphi$ ) versus strain for different object aspect ratios with PDMS as a matrix material. Analytical solutions according to Jeffery (1922) are given as solid lines. (a) Simple shear  $W_k = 1$ . (b)  $W_k = 0.8$ .

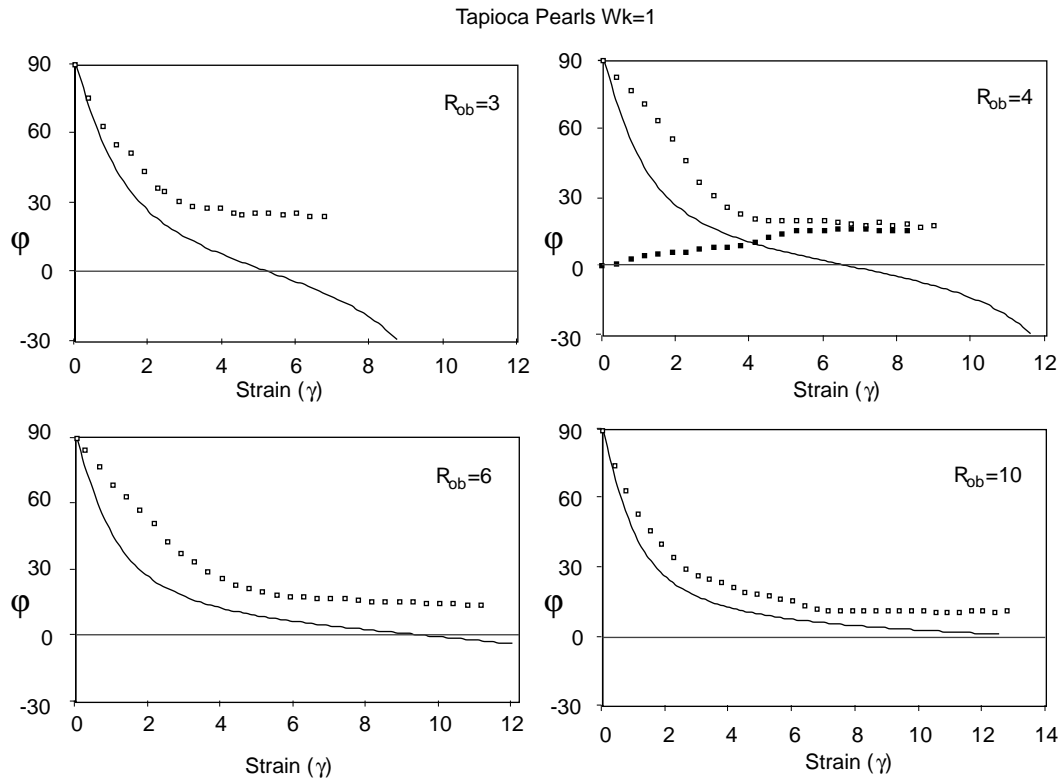


Figure 5.7. Object orientation ( $\varphi$ ) versus strain for experiments with tapioca pearls as a matrix material with four different objects. All experiments model simple shear deformation. Initial orientation for the objects is  $\varphi_0 = 90^\circ$  for all objects and  $\varphi_0 = 0^\circ$  for an additional experiment with the object with  $R_{ob} = 4$ . Solid lines are analytical solutions according to Jeffery (1922) for comparison.

reached the same orientation as for the experiment with  $\varphi_0 = 90^\circ$ . This indicates that the small positive angle is indeed a stable orientation for the object. The stable orientation ( $\varphi_{\text{stable}}$ ) is a function of the aspect ratio and decreases with increasing aspect ratio. This was also observed in the mineral-fishes in natural shear zones (Fig. 5.2).

The results for the experiments with tapioca pearls as matrix material with vorticity numbers 0.95, 0.8 and 0.6 are given in figure 5.8. The objects in these experiments show the same trend as in experiments with  $W_k = 1$ . When  $\varphi_0 = 90^\circ$  all objects start to rotate clockwise, towards a stable orientation (Table 5.3). Experiments with  $\varphi_0 = 0^\circ$  gave the same stable position as the experiments with  $\varphi_0 = 90^\circ$  for the same objects under the same conditions. The stable orientation ( $\varphi_{\text{stable}}$ ) as a function of aspect ratio of the object ( $R_{ob}$ ) for all experiments is plotted in figure 5.9. For experiments with a tapioca pearls matrix the maximum value for  $\varphi_{\text{stable}}$  is observed for the object with  $R_{ob} = 3$  in simple shear. Additionally it is shown that for all objects the lowest angle is observed for the experiments with  $W_k = 0.95$ .

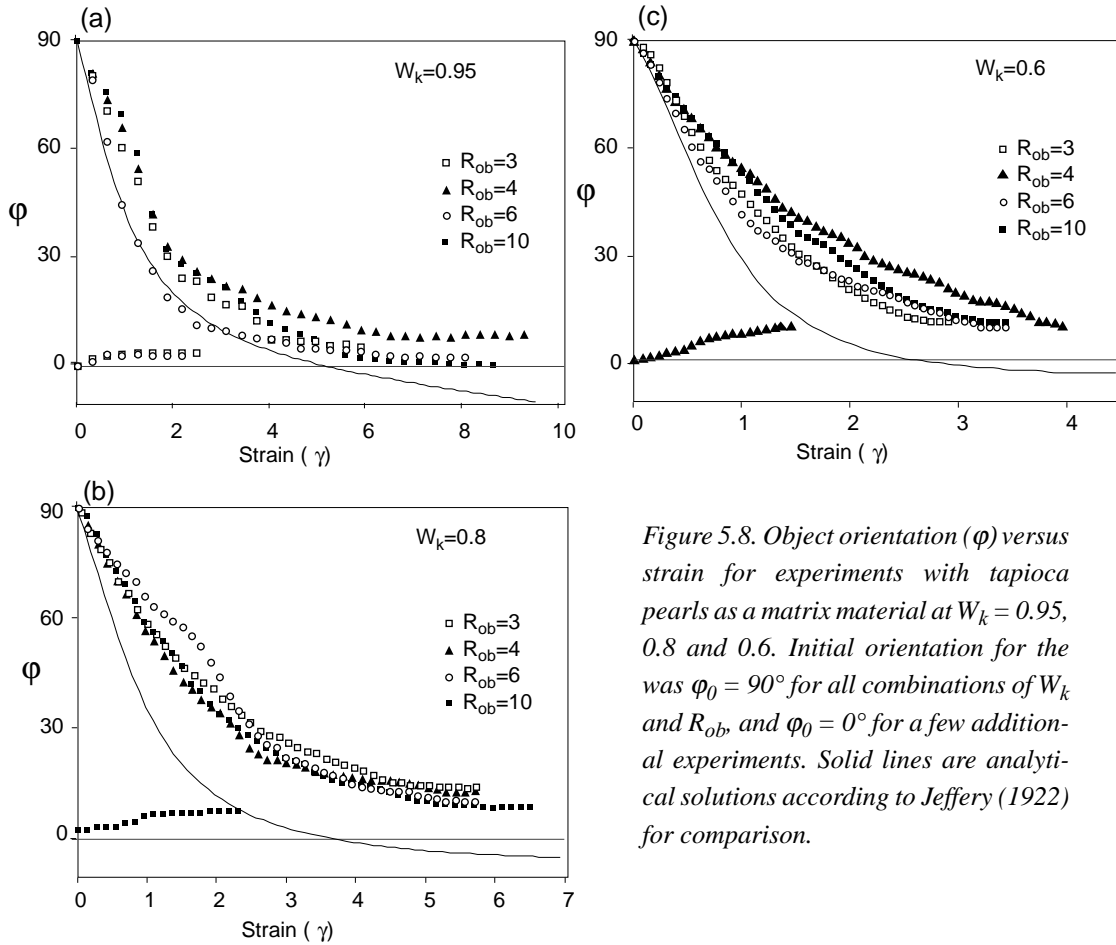


Figure 5.8. Object orientation ( $\phi$ ) versus strain for experiments with tapioca pearls as a matrix material at  $W_k = 0.95$ ,  $0.8$  and  $0.6$ . Initial orientation for the was  $\phi_0 = 90^\circ$  for all combinations of  $W_k$  and  $R_{ob}$ , and  $\phi_0 = 0^\circ$  for a few additional experiments. Solid lines are analytical solutions according to Jeffery (1922) for comparison.

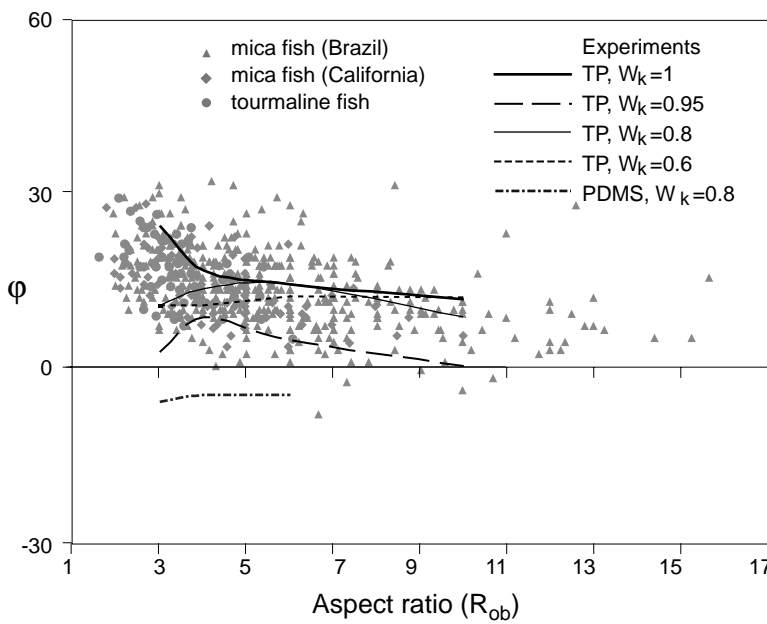


Figure 5.9. Plot of stable object orientation ( $\phi$ ) versus aspect ratio ( $R_{ob}$ ) for all performed experiments where a stable orientation was observed, together with the data of mica and tourmaline fish from three locations.

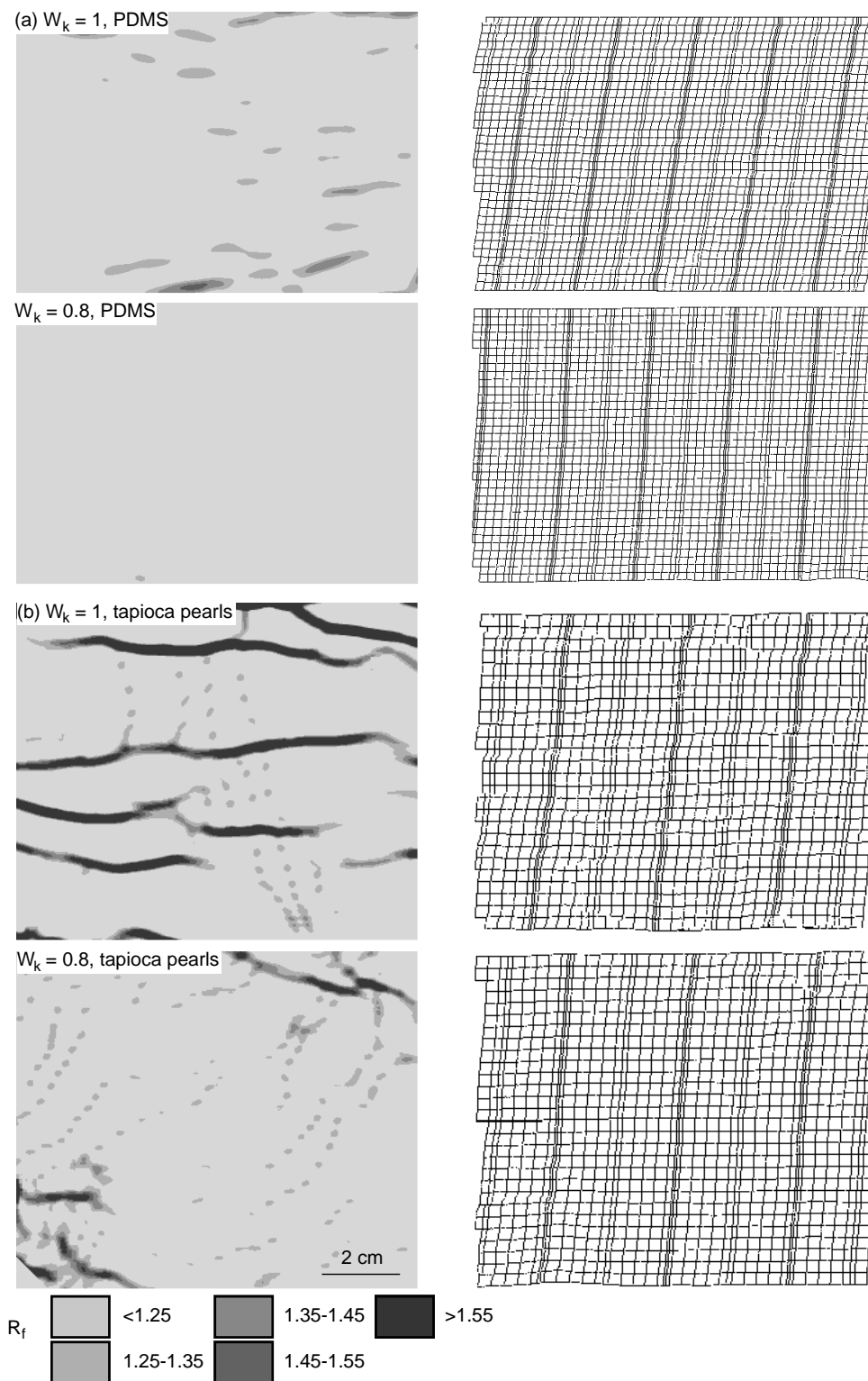


Figure 5.10. Analysis of the distribution of strain in samples without rigid object, shown as grey scale plots of the finite strain ellipse axial ratio ( $R_f$ ) and as deformed superimposed grids for a strain increments of  $R_f = 1.2$ . (a) Deformation in PDMS is homogeneously distributed throughout the sample and rarely exceeds the minimum finite strain value of  $R_f = 1.25$  that can be resolved. (b) Deformation in tapioca pearls aggregates is localised in dark dextral shear bands.

### 5.4.2 Analyses of strain distribution

Strain distribution during a strain increment within the sample was determined using pattern matching software "PatMatch" (Bons and Jessell 1995). With this program the distribution of deformation during each strain increment can be determined. Both materials were first investigated in the absence of a rigid object. In deforming PDMS, strain is distributed homogeneously throughout the material (Fig. 5.10a, Piazzolo 2000). In a matrix of tapioca pearls the strain is concentrated in small fault zones or shear bands (Fig. 5.10b), which are approximately parallel to the  $xz$ -direction. The regions between these zones show relatively little deformation. Analysis of the experiments with PDMS with a central object (Fig. 5.11) show the finite strain is distributed very homogeneously during the analysed time interval. Analysis of the experiments with tapioca pearls with a central object in its stable position show that in progressive simple shear deformation microfaults or shear bands are developed in the sample. The orientation of the shear bands is similar in tapioca pearls with and without a central object (Fig. 5.10 and 5.12). The shear bands accommodate up to 60% of the strain in the experiments with a central object. The long side of the object is parallel to the shear bands. The shear bands are not stable through time, but disappear while new bands appear at different places. With a decreasing vorticity number the spacing between the shear bands increases and the shear bands develop at a larger distance from the object (Fig. 5.12). Figure 5.12 shows the analyses of experiments with an object with  $R_{ob} = 6$  in its stable position. For this object the long side is parallel to the shear bands for  $W_k = 0.95$ , but not for  $W_k = 0.8$  and  $0.6$ . For objects with  $R_{ob} = 4$  and  $10$  in their stable positions the same is true. For an object with  $R_{ob} = 3$  in its stable position the long axis is only parallel to the shear bands in simple shear, not in shear with  $W_k = 0.95, 0.8$  and  $0.6$ .

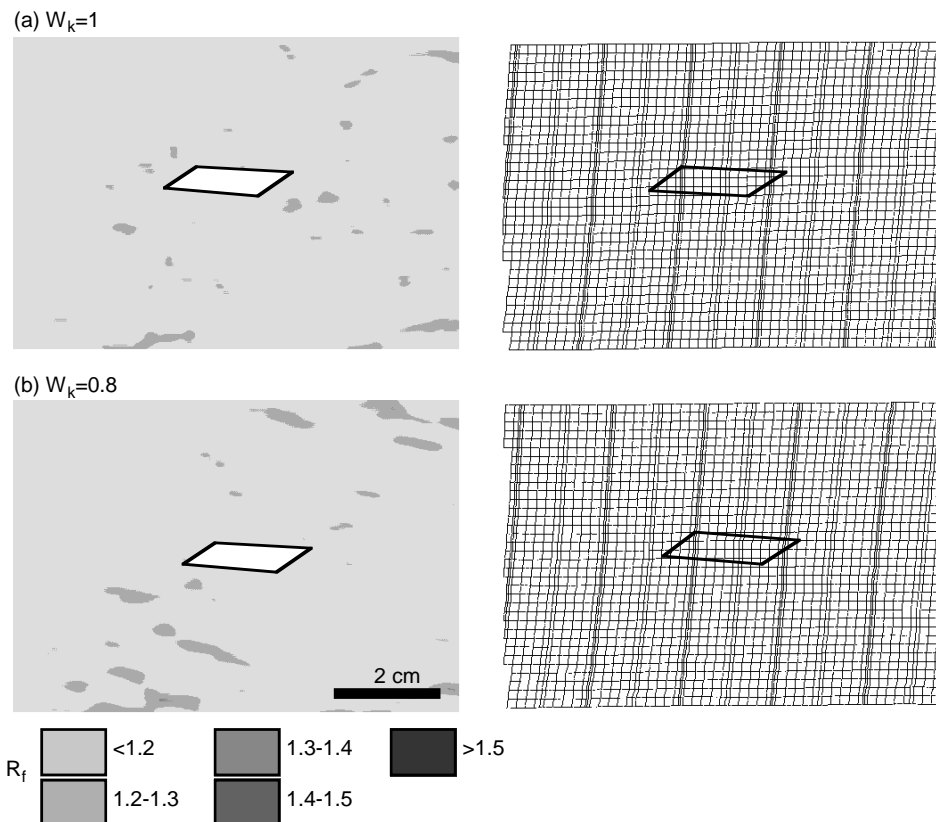


Figure 5.11. Contours of  $R_f$  values for experiments with PDMS as matrix material and object  $R = 6$ . a) Simple shear  $W_k = 1$ . b)  $W_k = 0.8$ . Bulk strain is in both cases  $R_f = 1.2$

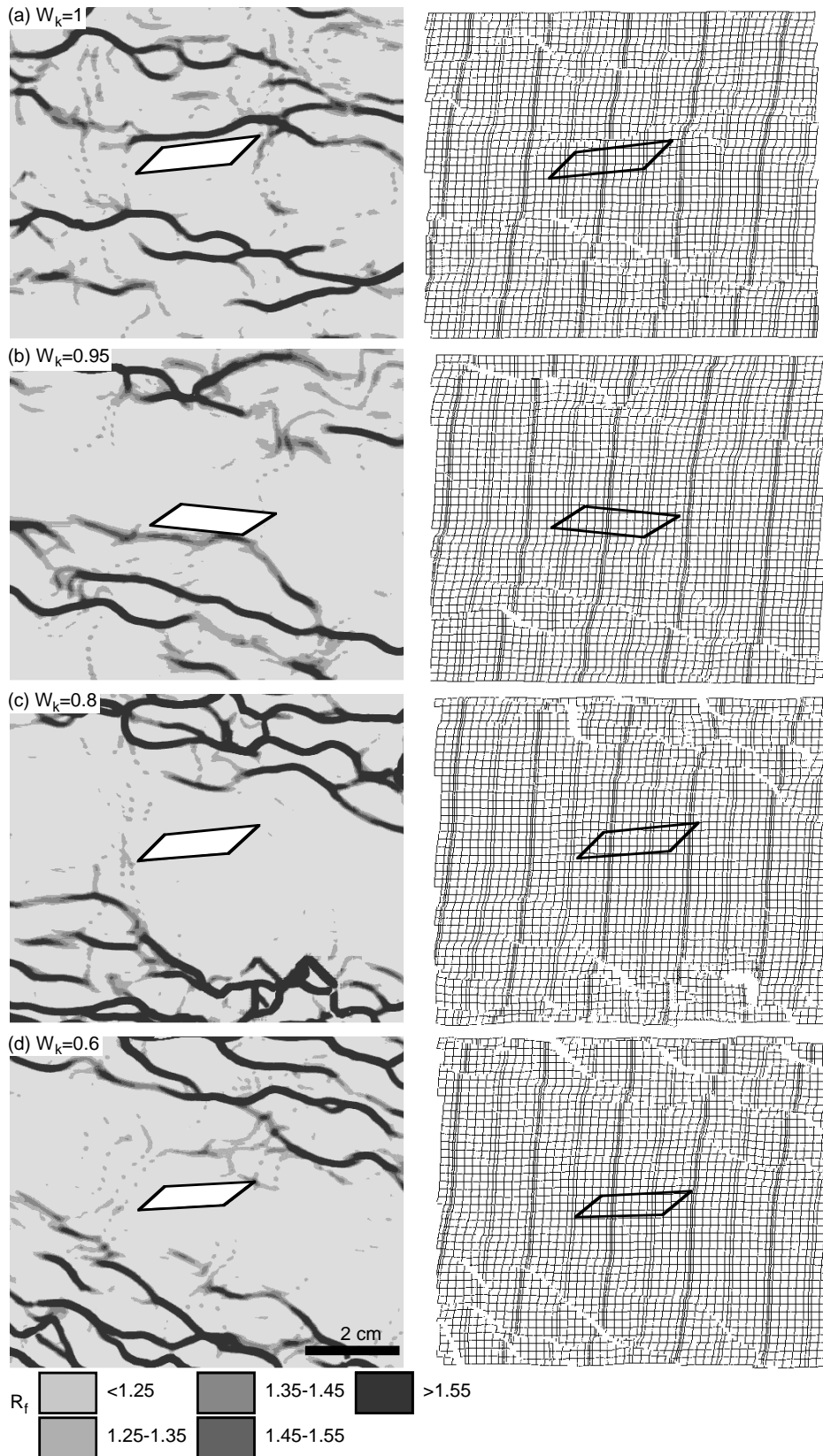


Figure 5.12. Contours of  $R_f$  values for experiments with tapioca pearls as matrix material and object  $R = 6$ . a) Simple shear  $W_k = 1$ . b)  $W_k = 0.95$ , c)  $W_k = 0.8$ , d)  $W_k = 0.6$ . Dark bands are highest strain rate zones. Bulk strain is in all cases  $R_f = 1.2$ .



## 5.5 Discussion

### 5.5.1 Discussion of experimental results

Analytical solutions of Jeffery (1922) and Ghosh and Ramberg (1976) for the rotation of elliptical objects in a Newtonian fluid are very similar to the results from experiments with monoclinic shaped objects in PDMS for objects with the same aspect ratio. The monoclinic instead of an elliptical shape of the objects appears to have very little effect on the rotation behaviour of the object.

The experiments with tapioca pearls show completely different results. The square object ( $R_{ob} = 1$ ) in simple shear is the only object with continuous clockwise rotation, although the rotation rate of this object is much lower than predicted by the analytical solutions and not constant. In all other experiments with tapioca pearls as a matrix material the object rotate towards a stable orientation, which is with its long axis at a positive angle to the x-axis of the apparatus. The orientation depends on the aspect ratio of the object and the vorticity number. The reason for this difference in behaviour compared to the experiments with PDMS is the different deformation behaviour of the matrix material. In tapioca pearls a significant part of the deformation is concentrated in shear bands and the areas between the shear bands undergo only limited deformation. This localisation of the strain is more pronounced in experiments with a central object, where the shear bands accommodate 60% of the deformation. This type of deformation is similar to the model of Bell (1985) and Bell et al. (1992): in the experiments the objects are situated in the low deformation areas or microlithons and therefore rotate slower compared to rotation rates in analytical solutions and experiments with PDMS. However, a significant part of the deformation is accommodated in the microlithons and the square object ( $R_{ob} = 1$ ) continues to rotate, in contrast to the model of Bell et al. (1992). The stable orientation of the monoclinic objects in the simple shear experiments and of the objects with  $R_{ob} = 4, 6$  and  $10$  in experiments with  $W_k = 0.95$  is with their long side subparallel to the shear bands in the matrix (Fig. 5.12a and b). Therefore, in these experiments the orientation of the shear bands seems to determine the orientation of the object. In the other cases, where the long side of the object is not parallel to the shear bands, the distance from the object to the closest shear bands is probably too large for the shear bands to have an influence on the orientation of the object. The controlling factor for the orientation of the objects in these experiments is not clear, but is probably due to stress distribution in the complex arrangement of shear bands, object and microlithon matrix. The incoherence of the matrix/object boundary as studied by Ildefonse and Mancktelow (1993) and Pennacchioni (2000) does not seem to be of great importance in our experiments, since no concentration of strain was observed along the object.

### 5.5.2 Comparison of experimental results with measurements of mica and tourmaline fish.

The measurements of natural mica and tourmaline fish from three different shear zones show very similar results for each shear zone. On average the long axes of fish with a low aspect ratio have a slightly higher angle to the mylonitic foliation than the long axes of fish with a high aspect ratio. To explain the orientation of the mineral fish in these measurements they are compared to the analytical solutions for rigid elliptical objects in Newtonian fluids (Jeffery 1922, Ghosh and Ramberg 1976) and to the experiments with monoclinic shaped objects in PDMS and tapioca pearls. For this comparison a few assumptions must be made. First of all the deformation of the mica and tourmaline fish should be slow in order to regard them as rigid objects. We think this is a valid assumption, because the mica and tourmaline fish can still be found as relatively large clasts in the intensely sheared matrix. Secondly, there should be little

interaction between the fish. The orientation of the fish is assumed to be only a function of their aspect ratio, and not influenced by interaction with neighbouring mineral fish. In the samples, the distance between the fish is usually large enough (more than a fish length) that interaction can be assumed to be negligible for most of the fish.

The trend of long axis versus aspect ratio for the natural mica and tourmaline fish and the trend for analytical solutions for ellipses in a Newtonian fluid and experiments with PDMS as matrix material show very little resemblance (Fig. 5.9). A stable orientation ( $\phi_{\text{stable}}$ ) for the elongated objects can be found in experiments with vorticity number  $W_k < 1$ , but the stable orientations as observed in these experiments and also the orientations resulting from analytical solution for elongated objects in viscous flow with  $W_k < 1$  (Ghosh and Ramberg 1976) are all negative, whereas the orientation of most of the natural mica and tourmaline fish is positive. The orientation of the long object axis versus aspect ratio as observed for the natural mica and tourmaline fish is however similar to the stable orientations for rigid objects in a matrix of tapioca pearls deformed in simple shear (Fig. 5.9).

Obviously, deformation in the mylonite zones containing mica and tourmaline fish is by completely different mechanisms from our analogue materials. PDMS is a Newtonian viscoelastic fluid; tapioca pearls a low cohesion granular material with Mohr-Coulomb type deformation. Nevertheless, it is remarkable that despite this difference such a close relation exists between mica fish in mylonites and rigid objects in tapioca pearls. This probably means that the crucial factor influencing the development of mica fish is the geometry of flow kinematics. Deformation is distributed fairly homogeneously in PDMS, and is localised in discrete shear bands in tapioca pearls or any other granular, Mohr-Coulomb material. The similarity between the data from natural examples and results from experiments with a Mohr-Coulomb matrix suggests that there must be strain localisation in mylonites in order to form mica fish. Strain localisation is also predicted by Lister and Snoke (1984), although we do not agree with all details of the mechanisms they propose. Lister and Snoke (1984) proposed that mica fish bordered by shear bands, but experiments with tapioca pearls show that shear bands can be further away and migrating through the sample with the same effect. Possibly, deformation in mylonites can be described by inhomogeneous flow that occurs by short living shear bands that shift position, as in tapioca pearls. Ongoing deformation and recovery mechanisms may overprint earlier fabrics and erase traces of flow partitioning and may explain the absence of grain-size gradients or other signs of enhanced strain towards the trails of mica grains. This kind of flow partitioning which is homogenised over time in progressive deformation has also been observed in experiments with the polycrystalline material octachloropropane (Bons and Jessell 1999).

The observed decrease in angle with aspect ratio of the mica and tourmaline fish of the natural samples fits best with the results of the simple shear experiments. However, as mentioned in the previous section the distance of the shear bands to the objects is the important for the stable orientation of the objects in the simple shear experiments. In the experiments with  $W_k < 1$ , the distance between object and the nearest shear bands increases with decreasing vorticity number. Besides the vorticity, the distance from the object to the nearest shear bands depends probably also on the grain size of the material. We did not test the effect of grain size, since in rocks the deformation mechanism is different. Therefore it is not possible to give a conclusion about the natural samples considering the vorticity number here.

## 5.6 Conclusions

Analogue experiments on the rotational behaviour of elongated rigid objects were carried out using two end-member model materials: PDMS (a Newtonian viscous polymer) and tapioca pearls (with Mohr-Coulomb behaviour). Several kinematic vorticity numbers were modelled. The results from the experiments with PDMS as a matrix gave similar results as analytical solutions for ellipses in viscous flow (Jeffery 1922, Ghosh and Ramberg 1976), indicating that the aspect ratio, not the detailed shape is the controlling factor for the rotation behaviour of objects in viscous materials. The results of the experiments with tapioca pearls as a matrix material give completely different result. Under all studied conditions, the elongated objects obtain a stable orientation, between  $\phi = 0.4^\circ \pm 0.5^\circ$  and  $24.4^\circ \pm 0.5^\circ$ . The deformation in tapioca pearls is concentrated in small shear bands on the scale of the tapioca pearls. Measurements of the long axis of natural samples of mica and tourmaline fish with respect to the mylonitic foliation show an average a tilted, positive orientation. The average angle decreases with aspect ratio of the object. These results fit very well with the results from the experiments in tapioca pearls in simple shear. This indicates that strain localisation in micro shear bands or zones is probably an important characteristic of the rheology of natural rocks with mica fish or other "mineral fish" and possibly of all mylonites. The presence of fish-shaped objects may be indicative for strain partitioning, even where no other microstructural indications for flow partitioning are found.

## Appendix A

Aggregates of tapioca pearls show Mohr-Coulomb type behaviour, where the shear stress ( $\tau$ ) for failure is related to the normal stress ( $\sigma_n$ ) on the failure plane by:

$$\sigma_n = C_0 + \mu\tau.$$

The coefficient of internal friction,  $\mu$ , and cohesion,  $C_0$ , for tapioca pearls were determined using the method described by Kranz (1991). The simple apparatus consists of two compartments, the lower one fixed and the upper one supported by four cables of about 40 cm length (Fig. 5.13). The compartments are 7.5 cm high, have a cross section of 4.35 cm and were both

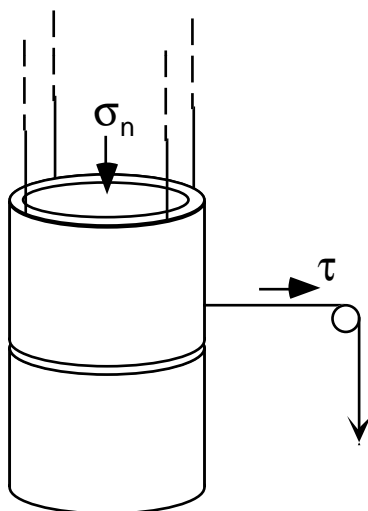


Figure 5.13. Schematic drawing of the set up used to measure the coefficient of internal friction and cohesion of tapioca pearls. Two cylinders are both filled with tapioca pearls. The bottom cylinder is fixed and the top cylinder is hanging on four cables, so the top cylinders can move frictionless with respect to the bottom one. The normal load is applied by the tapioca pearls in the upper cylinder and extra metal loads on top. The shear load is applied by the hanging mass over a pulley. Figure is not to scale.

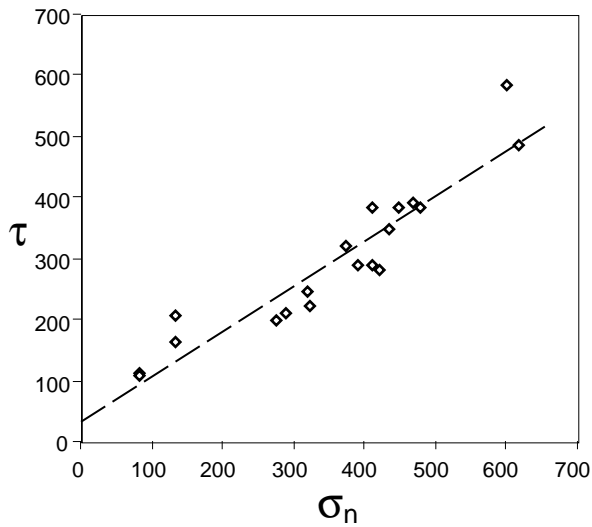


Figure 5.14. Plot of data from shear test on tapioca pearls shown as shear stress versus normal stress. The line is the best fit by linear regression and suggest that for failure in this material  $\mu = 0.74$  (slope) and  $C_0 = 39$  Pa (intercept)

filled with the pearls. A horizontal fault is created in the pearls when the top cylinder is shifted. The overlying tapioca pearls and extra metal loads determine the normal load across the horizontal fault surface between the two cylinders. Tapioca pearls were poured to the desired depth above the fault plane and the extra load was put on top. A shear load was applied to the top cylinder by adding water to a container hanging over a frictionless pulley. The shear load was increased until a distinct failure event occurred. The data points of this experiment are plotted in figure 5.14 as normal stress ( $\sigma_n$ ) versus shear stress ( $\tau$ ). The coefficient of internal friction,  $\mu$ , (slope) and cohesion,  $C_0$ , (intercept) follow from this plot. For tapioca pearls these values are  $\mu = 0.74 \pm 0.05$  and  $C_0 = 39 \pm 44$  Pa.

## Chapter 6

# Numerical modelling of simple shear flow around rigid objects in different matrix materials

### Abstract

The preferred orientation of certain objects such as mica fish in mylonites suggests that they reach a stable orientation during deformation. Theoretical and most experimental studies suggest continuous rotation of rigid objects in simple shear flow. In this study the effect of matrix rheology, the existence of inhomogeneities, boundary conditions and a slipping object-matrix interface on strain distribution and on rotation rate of rigid objects is studied with the finite difference code FLAC. Results of the experiments show that strain is localised around the rigid object in experiments with a Mohr-Coulomb type matrix, when soft layers are present in the matrix, or in the case of a soft object-matrix boundary in a power-law or Newtonian viscous matrix. In each of these cases rotation rate of the object is reduced and strain is localised, compared to the relatively homogeneously deforming power-law or Newtonian viscous matrix materials. This indicates that in mylonites an elongated rigid object can only reach a stable position in simple shear if deformation is localised around the object.

### 6.1 Introduction

The influence of the rheology of the matrix material, vorticity number of deformation, and aspect ratio of the object on the rotation of rigid elongated objects in plane strain deformation in analogue experiments was discussed in the previous chapter. These experiments have shown that the rheology of the matrix has a considerable effect on the rotational behaviour of rigid objects and that kinematic studies can therefore not be used to model all aspects of the behaviour of rigid objects in a deforming matrix. Analogue experiments and analytical solutions have shown that all rigid objects, except lines or planes, are continuously rotating in simple shear in a viscous matrix (Jeffery 1922, Ghosh and Ramberg 1976, Chapter 5). In a granular matrix material with a Mohr-Coulomb rheology, however, elongated objects obtain a stable position in simple shear (Chapter 5). In a viscous material strain is distributed relatively homogeneously, even when a single object is embedded in the material. Strain distribution is always inhomogeneous in a Mohr-Coulomb material. Discrete shear bands accommodate a large part of the strain, whereas the zones between the shear bands show only minor deformation, similar to the model of Bell et al. (1992) for partitioning of strain in mylonitic rocks. The localisation of strain is believed to be the decisive factor for the stable position of rigid elongated objects in

a Mohr-Coulomb matrix material. For the experiments in chapter 5 two matrix materials with completely different rheological behaviour were used, while the vorticity number of flow and the aspect ratio of the object were varied. Both matrix materials were homogeneous throughout the sample, and boundary conditions were equal for all the experiments. Anisotropy of the matrix material (Ten Brink 1996) and a non-cohesive object-matrix boundary (Ildefonse and Mancktelow 1993, Pennacchioni et al. 2000) are also considered to be important factors for the rotation of objects in a viscous matrix. Mechanical properties in mylonitic rocks are most likely anisotropic to some extent, due to alignment of micaceous minerals or a crystallographic preferred orientation. It can be envisaged that the object and matrix are partly or wholly decoupled.

Numerical models (Bons et al. 1997, Pennacchioni et al. 2000) and analytical solutions (Ferguson 1979, Jezek et al. 1994) of flow around circular objects in Newtonian and non-Newtonian viscous simple shear flow have shown that the stress exponent of the matrix material is of secondary importance for the flow pattern of the matrix and rotation of the object. However, boundary conditions (Bons et al. 1997) and cohesion between object and matrix (Pennacchioni et al. 2000) have a significant effect on the flow pattern. Bos (2000) reported microstructures from deformation experiments with mixtures of halite and kaolinite, which resemble the microstructures of mylonites with mica fish. In his experiments asymmetric halite clasts with elongated tails were developed in a fine grained anisotropic matrix of halite and kaolinite. Deformation of the mixture involved frictional sliding along kaolinite layers and pressure solution, giving a frictional-viscous behaviour.

The effect of several factors on strain distribution in the matrix and on the rotation rate of a rigid object in the matrix are studied with numerical simulations in this chapter. These factors are: (1) an inhomogeneous matrix with weak layers, (2) Mohr-Coulomb, power-law and Newtonian viscous rheologies, (3) the boundary conditions of the model, and (4) a slipping object-matrix boundary. The results of the numerical simulations are compared to microstructures of natural rocks with mica fish, presented in previous chapters, in order to get a better understanding of deformation around rigid objects and of rheology of the matrix material.

The computer code FLAC (Fast Lagrangian Analysis of Continua, Cundall and Board 1988; see also [www.itascacg.com](http://www.itascacg.com)) was used for the numerical simulations. FLAC is a plane-stress or plane-strain explicit finite difference code. In this code the discretised equations are solved by a dynamic relaxation scheme. New velocities and displacements are derived from stresses and forces through the equations of motion for each time step. Strain rates are derived from the velocities, and new stresses from the strain rates according to the relationship between stress and strain rate for the material (Ord 1994). This computer code has proven to be very useful in understanding the development of different microstructures, for example the formation of shear bands (Hobbs and Ord, 1989; Ord 1990), and fold geometry (Zhang et al. 1996a, 2000), and the understanding of glide processes, grain boundary sliding, and lattice rotation in polycrystalline aggregates (Zhang et al. 1996b; Zhang and Wilson, 1997).

## 6.2 Experimental method

### 6.2.1 Matrix models and material properties

Three different rheologies were used for the matrix: 1a) power-law viscous, 1b) linear (Newtonian) viscous, and 2) Mohr-Coulomb (plastic). The basic equation for the relation between strain rate ( $\dot{\gamma}$ ) and stress ( $\tau$ ) for a viscous material is:

$$\dot{\gamma} = B\tau^n \exp\left(\frac{-Q}{RT}\right) \quad (6.1)$$

(e.g. Sibson 1977), where B depends on the diffusion constant and temperature, Q is the activation energy, R is the gasconstant, T is the temperature, and n is called the power-law constant. For constant temperature this formula is simplified to:

$$\dot{\gamma} = A \cdot \tau^n \quad (6.2)$$

where A is a constant, used values are given in table 6.1. The power-law exponent (n) in the experiments described here is n = 3, as in the flow law for bulk diffusion controlled dislocation creep. A value of n = 3 is thought to be realistic in rock deformation (Poirier 1980). This type of behaviour is called power-law or non-Newtonian viscous behaviour. In this study I use the term power-law matrix for a matrix deforming according to this stress-strain rate relationship. Viscous deformation with a power-law exponent of n = 1 is also called Newtonian viscous behaviour. The relation between strain rate ( $\dot{\gamma}$ ) and stress ( $\tau$ ) is given by:

$$\dot{\gamma} = 1/\eta \cdot \tau \quad (6.3)$$

(Twiss and Moores 1992) where  $\eta$  is the viscosity (table 6.1), and  $\eta = 1/A$ . The viscosity used here is  $\eta = 10^{18}$  Pa·s, which is the estimated effective viscosity for the lower crust in extensional regimes and beneath low-gradient boundaries in convergent orogens (Clarck and Royden 2000). The value for the constant A was estimated using the values for activation energy and the diffusion constant for self diffusion of Farver and Yund (1991). For a temperature of T = 450°C, A =  $10^{-30}$ .

The third model material is deforming by frictional sliding. Sliding occurs when a critical shear stress ( $\tau$ ) is exceeded.

$$\tau = c + \mu\sigma_n \quad (6.4)$$

(Twiss and Moores 1992), where  $\sigma_n$  = normal stress. Cohesion (c) and coefficient of internal friction ( $\mu$ ) or friction angle ( $\phi$ , where  $\mu = \tan(\phi)$ ) are material properties. The Mohr-Coulomb yield function is sometimes expressed in terms of the critical principal stresses. The maximum compressive stress required for yield is:

$$\sigma_1 = \sigma_3 \frac{1 + \sin \phi}{1 - \sin \phi} + 2c \sqrt{\frac{1 + \sin \phi}{1 - \sin \phi}} \quad (6.5)$$

(Twiss and Moores 1992).

Table 6.1. Values of matrix properties.

Power-law viscous $\dot{\gamma} = A \cdot \tau^n$		Newtonian viscous $\dot{\gamma} = 1/\eta \cdot \tau$		Object in viscous matrix	
Density (g/dm <sup>3</sup> )	2700	Density (g/dm <sup>3</sup> )	2700	Density (g/dm <sup>3</sup> )	2700
Shear modulus (Pa)	1·10 <sup>9</sup>	Shear modulus (Pa)	1·10 <sup>9</sup>	Shear modulus (Pa)	2·10 <sup>11</sup>
Bulk modulus (Pa)	0.6·10 <sup>9</sup>	Bulk modulus (Pa)	0.6·10 <sup>9</sup>	Bulk modulus (Pa)	1.2·10 <sup>11</sup>
Constant A	1·10 <sup>30</sup>	Viscosity $\eta$ (Pa·s)	1·10 <sup>18</sup>	Viscosity $\eta$ (Pa·s)	1·10 <sup>20</sup>
Stress exponent n	3				
Mohr-Coulomb $\tau = c + \mu\sigma_n$		Object in Mohr-Coulomb matrix			
Density (g/dm <sup>3</sup> )	2700	Density (g/dm <sup>3</sup> )	2700		
Shear modulus (Pa)	2·10 <sup>10</sup>	Shear modulus (Pa)	2·10 <sup>11</sup>		
Bulk modulus (Pa)	1·10 <sup>10</sup>	Bulk modulus (Pa)	1.2·10 <sup>11</sup>		
Friction angle $\phi$ (°)	45	Viscosity $\eta$ (Pa·s)	5·10 <sup>23</sup>		
Cohesion (Pa)	5·10 <sup>7</sup>				

In this study a matrix material deforming according to this model is called a Mohr-Coulomb matrix. The values for friction ( $\phi = 45^\circ$ ) and cohesion ( $c = 50$  MPa, Table 6.1), are typical values for quartzites, (Goodman 1980). In the FLAC code all materials also have elastic properties, where bulk and shear modulus were similar to values used for numerical simulations by Hobbs and Ord (1989), (Table 6.1). The rheological model, matrix properties boundary conditions, and type of object-matrix boundary for all 23 experiments are listed in Table 6.2. A central object was inserted in the matrix. This object has a viscous rheology, with a high viscosity compared to the matrix (Table 6.1) in all experiments.

### 6.2.2 Boundary conditions

The model consists of a central object, embedded in a less competent matrix. The finite difference grid is rectangular and contains 80 x 80 elements (Fig. 6.1a), for experiments where the matrix has a Newtonian or non-Newtonian viscous rheology. Two different central objects were used, a square object consisting of 8 x 8 elements and a horizontally aligned rectangular object with a length-width ratio of three, consisting of 16 x 8 elements (Fig 6.1a). For the rectangular object the width of the elements in the y-direction is reduced to 2/3 times the standard unit size to get the desired aspect ratio (Fig. 6.1). The grid for the Mohr-Coulomb matrix rheology measured 180 by 60 elements in x- and y-direction respectively. The square object measured 12 x 12 elements and the rectangular object 24 x 12 elements. The length-width ratio for the Mohr-Coulomb matrix rheology was different, to reduce boundary effects, that will be discussed later. The object was located in the centre of the grid, initially parallel to the boundaries of the model, in all experiments.

Dextral simple shear deformation was modelled with two different sets of boundary conditions: 1) Fully velocity constrained, where the velocities in both x- and y-direction direction were set for all boundary nodes (Fig. 6.1). In this case all boundaries remain perfectly planar during the experiment. 2) Laterally unconstrained, where velocities in the x- and y-direction



were only set on the horizontal boundaries (Fig. 6.1). Stress was zero at the unconstrained boundaries. Only few experiments were performed with the latter set of boundary condition. Both sets of boundary conditions are comparable to those of different types of shear boxes. The first set is comparable to boundary conditions of a deformation box as described in chapter 3 and 5, and the second set is like the boundary conditions of a shear box where the sample is deformed between two rigid plates, but is laterally unconstrained. The shear strain rate was  $\dot{\gamma} = 2 \cdot 10^{-14} \text{ s}^{-1}$  in all experiments, which is in the range of  $10^{-13} \text{ s}^{-1}$  to  $10^{-15} \text{ s}^{-1}$  deduced from natural rocks (Pfiffner and Ramsey 1982). Calculations were carried out in  $5 \cdot 10^5$  strain increments of  $\gamma = 2 \cdot 10^{-6}$ , or  $1 \cdot 10^8 \text{ s}$  ( $\approx 3.2 \text{ year}$ ), to a finite strain of  $\gamma = 1$ .

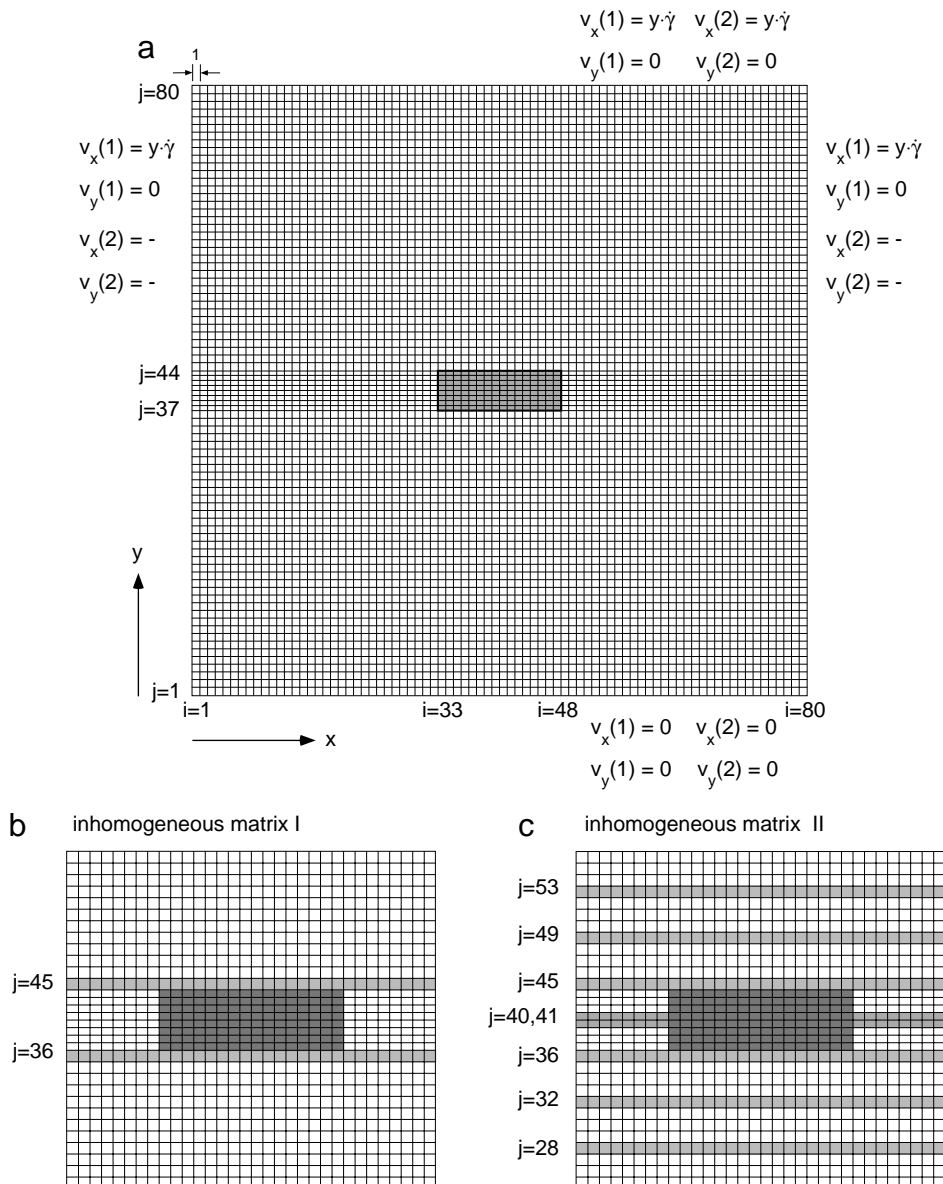


Figure 6.1. (a) The model showing the dimensions of the rectangular object ( $R_{ob} = 3$ , shaded) and the finite difference grid. Velocities in  $x$ - and  $y$ -direction for each boundary node are indicated at the sides of the model. (b, c) A 1.5 times magnification of the central part of the grid, showing the object (grey) and the weak zones (light grey) in the matrix in the model with inhomogeneous matrix I (b) and inhomogeneous matrix II (c).

### 6.2.3 Build-in inhomogeneities

Additional experiments were carried out with an inhomogeneous viscous matrix (Newtonian and power-law), by inserting relatively soft horizontal layers in the matrix. Two sets of experiments with such inhomogeneous properties were performed: inhomogeneous matrix type I with two horizontal soft rows above and below the object (row  $j=36$  en  $j=45$ , Fig. 6.1b), and inhomogeneous matrix type II an arrangement of soft layers as shown in Fig. 6.1c. Soft layers formed 25% of the matrix in this latter model.

The ratio between the constant  $A$  in the soft layers and the remainder of the matrix is given by  $Z_A = A_{\text{layers}} / A_{\text{matrix}}$ . In the experiments with a Newtonian viscous matrix the weaker zones have a viscosity two times less than the remainder of the matrix,  $Z_A = 2$ . Experiments with a power-law matrix are performed with variable  $Z_A$ , where the constant  $A$  is set at 2, 4, 10 or 25 times higher than the remainder of the matrix ( $Z_A = 2, 4, 10$  and  $25$ , Table 6.2). The stress exponent  $n$  is kept the same in both strong and weak matrix materials.

The effect of the weak zones on the relative rotation rate of the object ( $\Omega_{\text{rel}}$ ) compared to the rotation rate of the object in a homogeneous matrix is described by

$$\Omega_{\text{rel}} = \Omega_{\text{inhom}} / \Omega_{\text{hom}} \quad (6.6)$$

where  $\Omega_{\text{inhom}}$  is the rotation rate of the object in the inhomogeneous matrix and  $\Omega_{\text{hom}}$  is the rotation rate of the object in a homogeneous matrix.

### 6.2.4 Soft boundary between object and matrix

In one experiment the boundary between the object and the matrix was made softer than the remainder of the matrix, to model the effect of a less coherent object matrix boundary. A soft boundary was created by giving one layer of elements around the object a higher value for  $A$ . In the experiment a power-law matrix with  $Z_A = 10$  was modelled, the object was rectangular, and velocities on all boundaries were constrained.

## 6.3 Experimental results

Experiments were set to run up to a shear strain of  $\gamma = 1$ . This was not reached for all experiments, due to geometrical problems of the model. In zones of high material contrast, grid elements may rapidly obtain highly distorted shaped. Once the shape of grid elements exceed a certain degree of deformation, the model shuts down since stress and strain can not longer be calculated for these elements. Finite strain for each model is listed in table 6.2. Results of the numerical experiments were saved after every strain increment of  $\Delta\gamma = 0.2$ . Experiments with fully velocity-constrained boundaries are first discussed in section 6.3.1, while those with laterally unconstrained boundaries are presented in section 6.3.2. The deformed grid and the strain rate distribution are shown together. Comparison of the deformed grid with the strain rate distribution at a certain moment gives an idea whether the strain rate distribution is constant during deformation or not. When the strain rate distribution is constant through time the zones with a high strain rate coincide with high finite strain zones in the deformed grid. The orientation of the side of the object with respect to the  $x$ -direction is measured after each strain increment of  $\Delta\gamma = 0.2$  or 100.000 steps.

Table 6.2. List of experiments. <sup>1</sup> M-C = Mohr-coulomb matrix material, <sup>2</sup> Boundary conditions C = velocity on all boundaries is constrained. U = Velocity is laterally unconstrained. <sup>3</sup> Properties of the matrix are inhomogeneous in some experiments, see text for explanation. <sup>4</sup> Ratio between constant A.

Matrix rheology	Length/width ratio object	Boundary conditions <sup>2</sup>	Inhomogeneous matrix <sup>3</sup>	$Z_A$ <sup>4</sup>	Finite strain $\gamma$
M-C	3	C	-		1
M-C	1	C	-		1
Power-law	3	C	-		1
Power-law	3	C	I	2	1
Power-law	3	C	II	2	1
Power-law	3	C	I	4	0.88
Power-law	3	C	II	4	0.93
Power-law	3	C	I	10	0.77
Power-law	3	C	II	10	0.92
Power-law	3	C	I	25	0.6
Power-law	3	C	II	25	0.8
Power-law	3	C	o/m boundary	10	0.49
Power-law	3	U	-		1
Power-law	3	U	I	2	1
Power-law	1	C	-		1
Power-law	1	U	-		1
Newtonian	3	C	-		1
Newtonian	3	C	I	2	1
Newtonian	3	C	II	2	1
Newtonian	3	U	-		1
Newtonian	3	U	I	2	1
Newtonian	1	C	-		1
Newtonian	1	U	-		1

### 6.3.1 Fully velocity constrained boundaries.

#### 6.3.1.1 Homogeneous viscous matrix

The experiments with a homogeneous power-law or Newtonian viscous material are showing similar results. In the experiments with the rectangular object (Fig. 6.2), the highest strain rate is observed along the upper and lower side of the object and lowest in the zones next to the right and left sides of the object. For the square object (Fig. 6.3) highest strain rates are observed at the corners and lowest strain rates at the sides of the object. The strain distribution is constant through time, because the zones high and low strain rate coincide with the parts of the grid that are most and less deformed, respectively. The slight difference between the experiments with a power-law and Newtonian viscous matrix is that the values for the maximum and minimum strain rate are more extreme in the power-law matrix material. The effect of the object on the strain rate can be noticed at a significant distance from the object, for the elongated object especially around the upper left and lower right corner (Fig. 6.2).

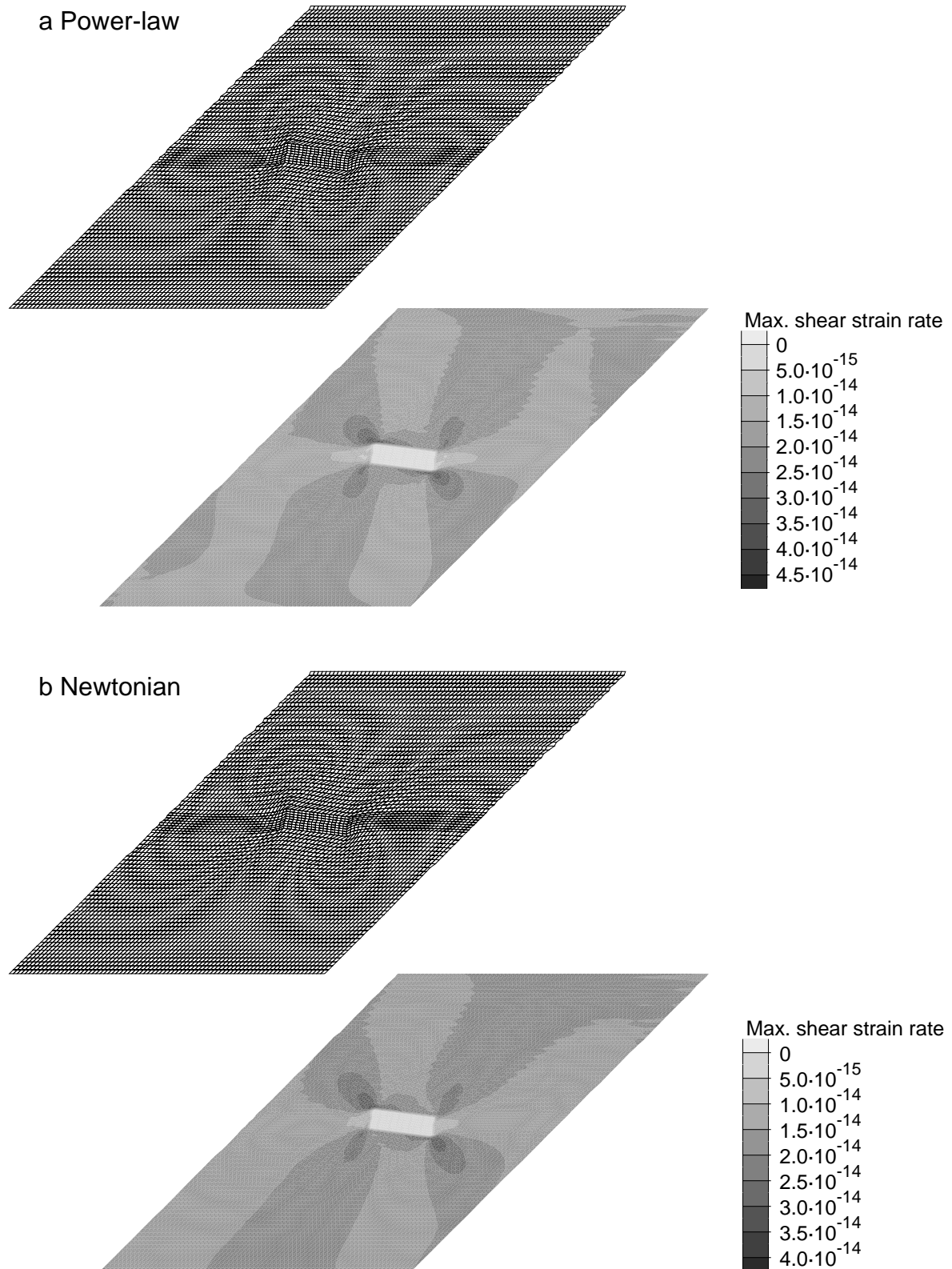


Figure 6.2. Deformed grid and distribution of the maximum strain rate after a finite strain of  $\gamma = 1$  for the experiments with a power-law (a) and Newtonian (b) viscous matrix material with homogeneous properties and a rectangular object.

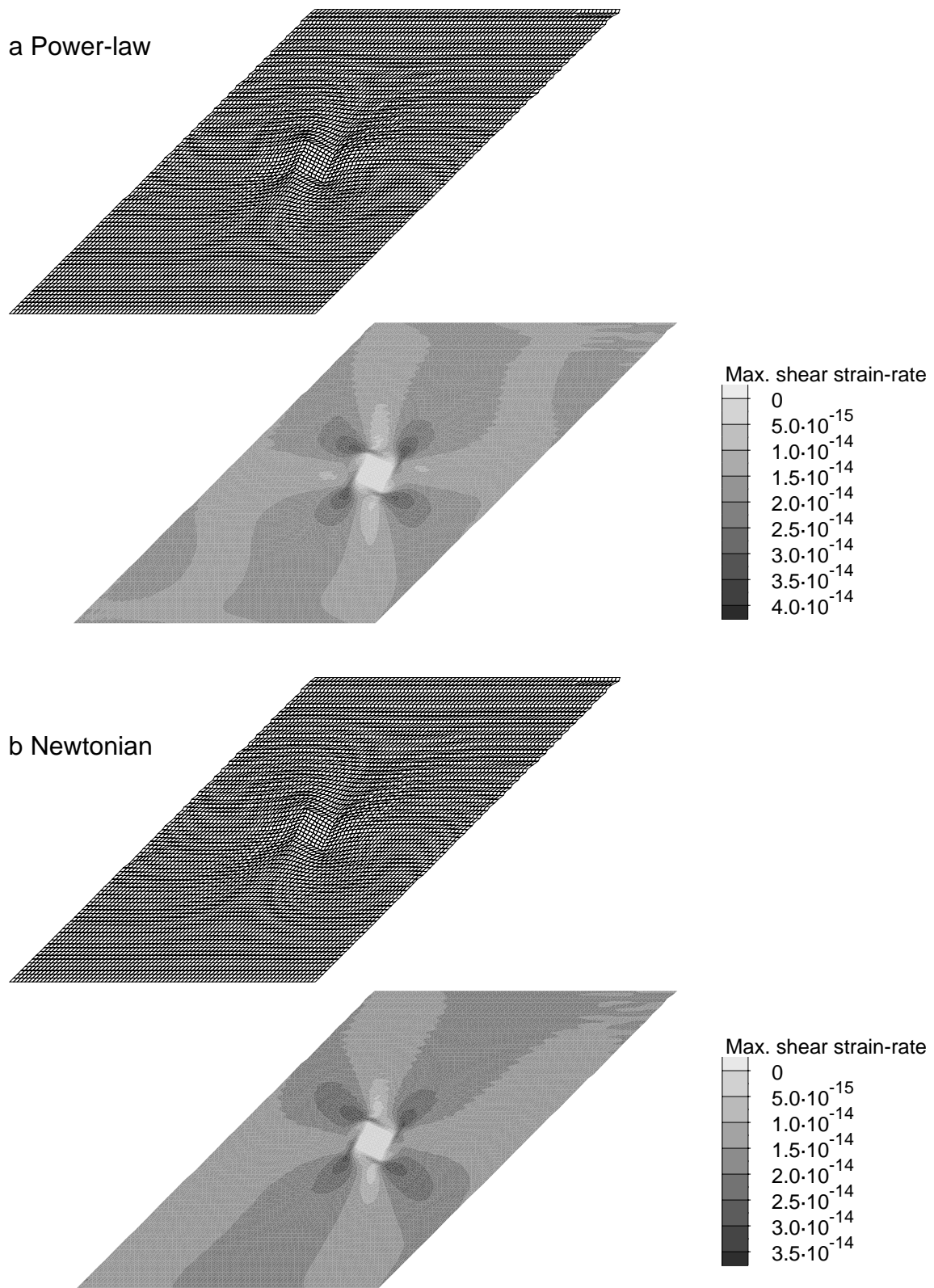


Figure 6.3. Deformed grid and distribution of the maximum strain rate after a finite strain of  $\gamma = 1$  for the experiments with a power-law (a) and Newtonian (b) viscous matrix material with homogeneous properties and a square object.

In a power-law or Newtonian viscous matrix in experiments with constrained velocity at the sides of the model, the square object rotates as predicted by analytical solutions for a sphere in a viscous fluid (Fig 6.4, Jeffery, 1922). The rectangular object has a rotational behaviour equal to the theoretical rotation of an ellipsoid with a 12.5% smaller aspect ratio under these condi-

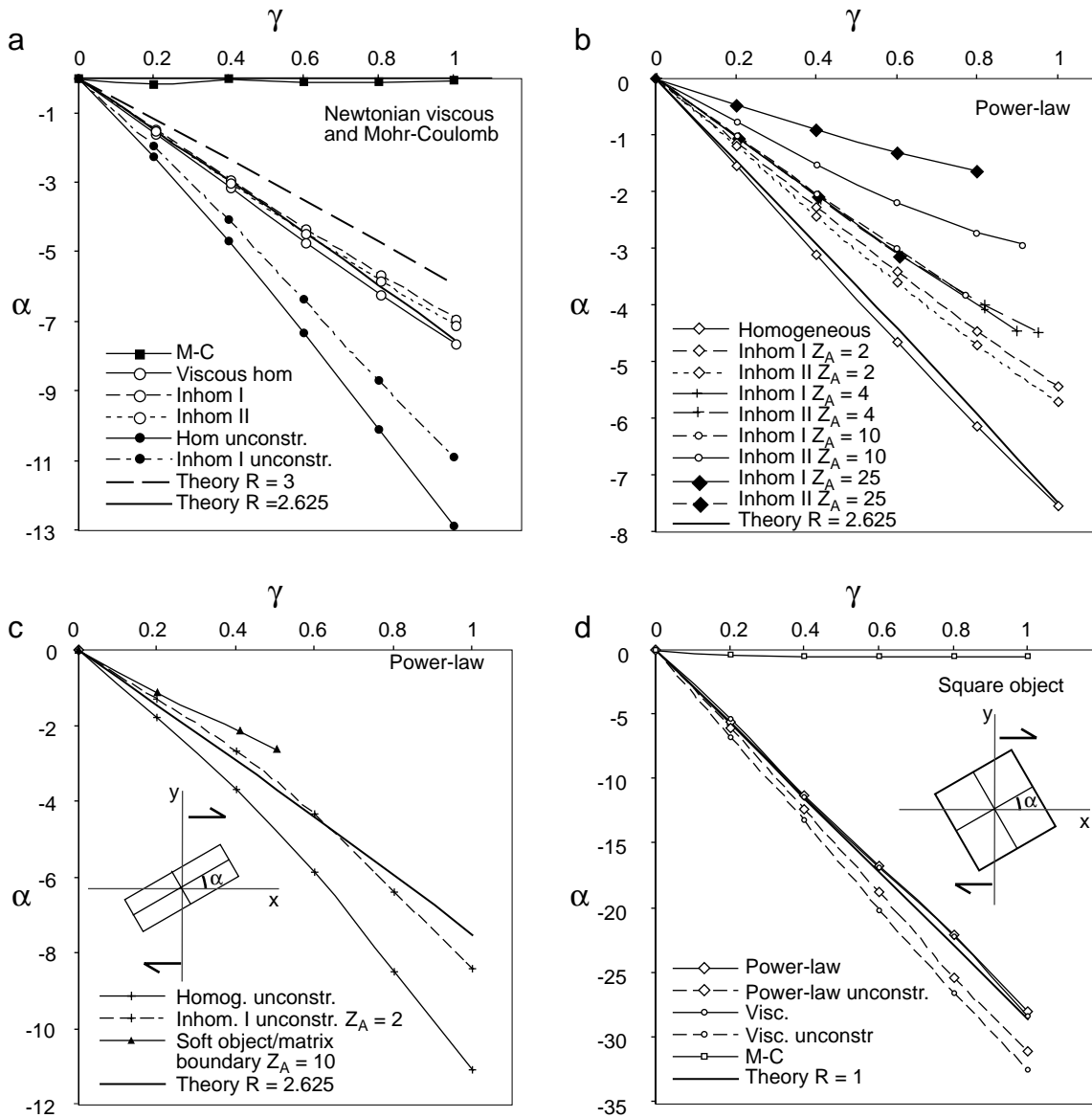


Figure 6.4. Graphs of the orientation of the object with respect to the  $x$ -direction of the model ( $\alpha$ ) versus the finite strain ( $\gamma$ ). (a) For the rectangular object in a Mohr-Coulomb or Newtonian viscous matrix. (b) For the rectangular object in a power-law matrix with homogeneous properties, or with soft layers inserted in the matrix. (c) For the rectangular object in a power-law matrix with a soft layer around the object, and with unconstrained boundaries of the model. (d) For the square object. The slope of these graphs represents the rotation rate of the object,  $Z_A$  is the contrast between the constant  $A$  in the soft layers and the remainder of the matrix.

tions. This result is similar to that determined in experiments by Ten Brink (1996) with a Newtonian viscous matrix material.

Both strain distribution and rotation of the object are similar in experiments with a power-law viscous matrix ( $n = 3$ ) and with a Newtonian viscous matrix, indicating that an increase in the stress exponent does not change the behaviour of the object significantly. Similar findings were reported by Ferguson (1979), Bons et al. (1997) and Pennacchioni et al (2000).

### 6.3.1.2 Inhomogeneous viscous matrix

The strain distribution in the experiments with weaker zones in the matrix also is similar for experiments with a power-law and with a Newtonian viscous matrix rheology. In all experiments with an inhomogeneous matrix type I and type II the effect of the weaker zones is that the strain rate and finite strain is increased in the weak zones and more homogeneously distributed in the remainder of the matrix (Fig. 6.5), compared to the experiments with a homogeneous viscous matrix. The highest strain rates are observed in the weak zones next to the upper left and lower right corner of the object. Although the velocity of the sides of the model is constrained, the effect of the weaker zones is seen at a small distance from the sides of the model. Localisation is more pronounced if the difference between the strength of the soft layers and the remainder of the matrix is higher. In the experiments with inhomogeneous matrix type II the ratio of the strain rate in soft layers and in the remainder of the matrix is similar to the value of  $Z_A$ , the ratio between constant A in the matrix and in the weak zones. This means that for the experiments with matrix type II and with  $Z_A = 2$  as expected about 40% of the total strain is accommodated by the soft layers, for  $Z_A = 4$  about 57%, for  $Z_A = 10$  about 77%, and for  $Z_A = 25$  about 90% of the strain.

The effect of weaker zones in the matrix material on the rotation rate of the central object is generally a reduction of the rotation rate compared to a matrix with homogeneous properties (Fig. 6.4b). For the Newtonian viscous matrix with  $Z_A = 2$  the effect of two weak zones above and below the object (type I) is a reduction of 8.3% of the rotation rate of the rectangular object a viscous matrix with homogeneous properties. In the experiments with matrix type II the rotation rate is reduced 5.5%.

In the case of a power-law matrix there is also a reduction of the rotation rate due to the weaker zones in the matrix. Figure 6.6 shows the reduction of strain rate compared to the power-law matrix with homogeneous properties given as a function of the factor  $Z_A$ . This figure shows that the reduction of the rotation rate is higher for matrix type I then for matrix type II for low values of  $Z_A$  ( $Z_A < 4$ ). For higher values of  $Z_A$ , the effect of the inhomogeneous matrix on the rotation rate is higher for the model with matrix type II. The effect on the rotation rate for experiments with matrix type I does not increase significantly for values of  $Z_A > 4$ , but stays around  $\Omega_{rel} = 0.66$ . This indicates that in a matrix with only two weak zones above and below the object there is a limit to the influence of these zones on the rotation rate. In our experiments this limit was reached at a value of  $Z_A \approx 4$ .

## Power-law viscous matrix

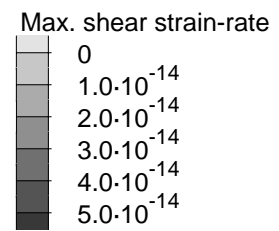
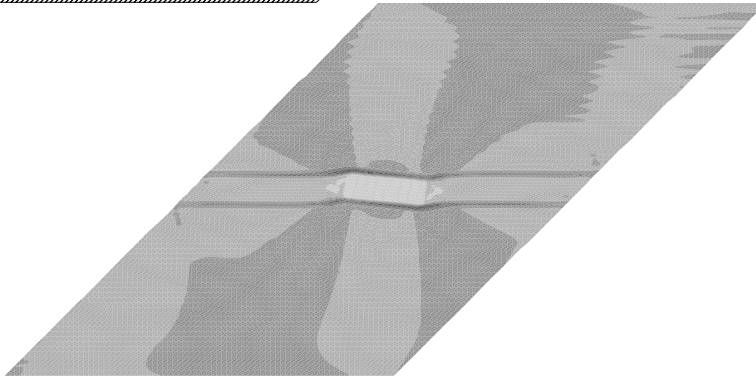
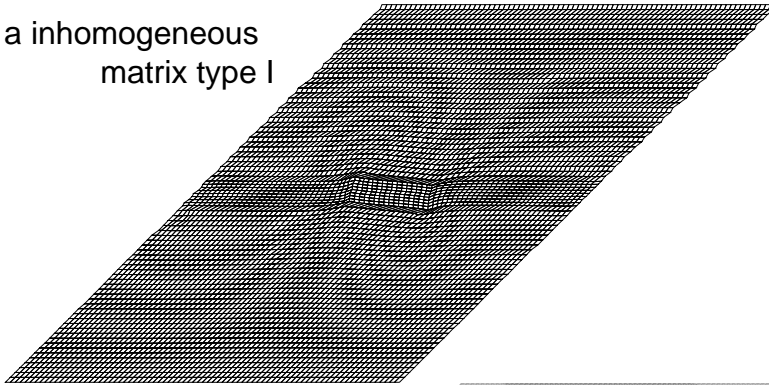
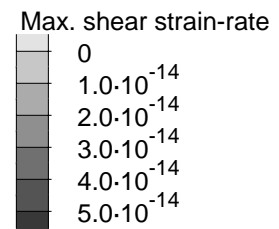
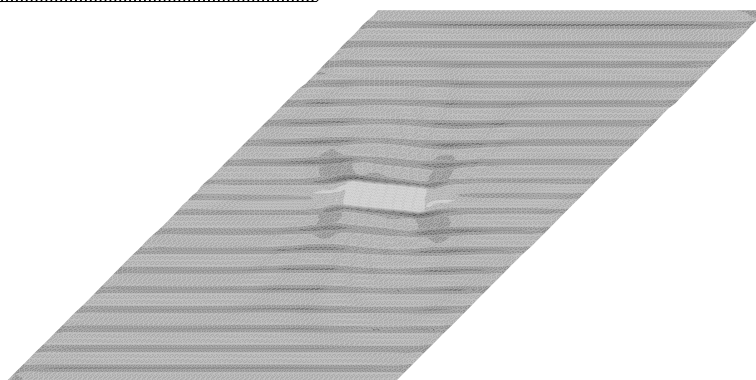
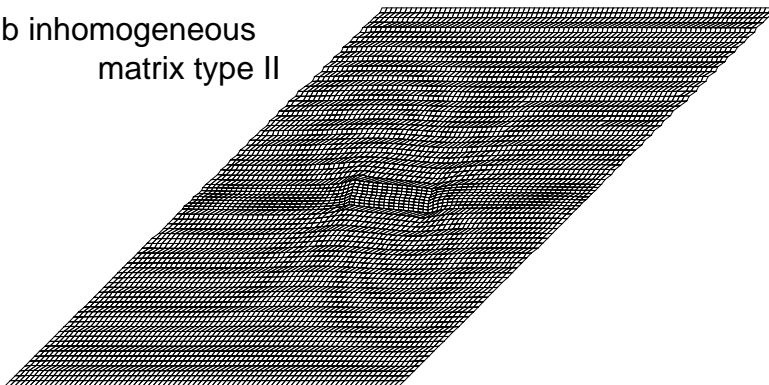
a inhomogeneous  
matrix type Ib inhomogeneous  
matrix type II

Figure 6.5. Deformed grid and distribution of the maximum strain rate after a finite strain of  $\gamma = 1$  for the experiments with a power-law viscous matrix material with soft layers inserted in the matrix and with a rectangular object. ( $Z_A = 2$ )



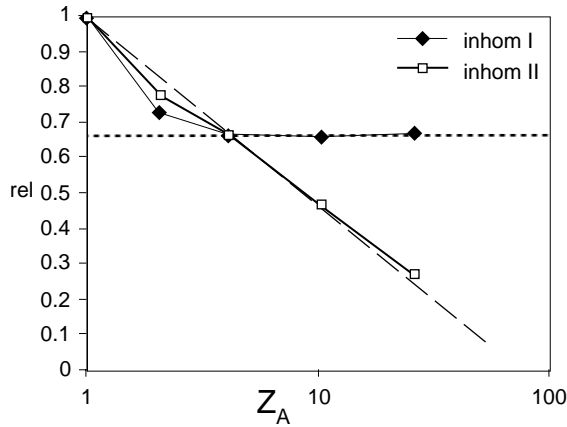


Figure 6.6. Graph of the reduction in rotation rate of the rectangular object in experiments with weaker zones in the matrix, compared to the rotation rate of the object in a homogeneous power-law matrix, as a function of the ratio of the constant  $A$  in the weak zones and the remainder of the matrix ( $Z_A$ ).

With matrix type II and a power-law viscous matrix the rotation rate of the object as a function of the factor  $Z_A$ , as shown in Figure 6.6, is described by the formula

$$\Omega_{\text{rel}} = (\Omega_{\text{hom}} - k \cdot \log(Z_A)) / \Omega_{\text{hom}} \quad (6.7)$$

where  $k$  is a constant and  $\Omega_{\text{hom}}$  is the rotation rate of the object in a homogeneous viscous matrix. In the experiments where 25% of the matrix consists of soft layers, the constant  $k$  was found to be  $k = 0.53$  for the rectangular object. If this formula is also valid for higher values of  $Z_A$ , this would mean that rotation rate is reduced to zero for an effective viscosity contrast between the matrix and the soft layers of  $Z_A \approx 80$ . The function for  $\Omega_{\text{rel}}$  is possibly valid for all experiments with shear bands distributed through the matrix. The constant  $k$  would in that case be a function of the amount and the width of the shear bands, and the stress exponent ( $n$ ) of the matrix material.

In figure 6.7 the principal stress tensor is plotted as crosses where bars indicate the magnitude and orientation of the principal stresses. Diagrams are given for experiments with a homogeneous matrix with power-law rheology and with an inhomogeneous matrix type I with  $Z_A = 10$ . This figure shows that stress is more homogeneously distributed in the matrix above and below the object in the experiments with the inhomogeneous matrix. At the side of the object there is no significant difference in stress distribution between the two experiments. The highest differential stresses ( $\sigma_1 - \sigma_3$ ) are found in the upper left and lower right corner of the object (Fig. 6.7) and lowest in the matrix besides the lower left and upper right corner of the object. Differential stress on upper and lower boundary of the object is low in the experiments with an inhomogeneous matrix, compared to the stress in the matrix with homogeneous properties (Fig 6.7). This probably causes the reduction in rotation rate of the object.

The stress and strain is localised in the upper left and lower right corners of the object in dextral simple shear, which indicates that these corners are potential areas for dynamic recrystallisation, and source areas for pressure solution. Sink areas for pressure solution would be the lower left and upper right corners of a rectangular object in dextral shear, where stress and strain rate are low.

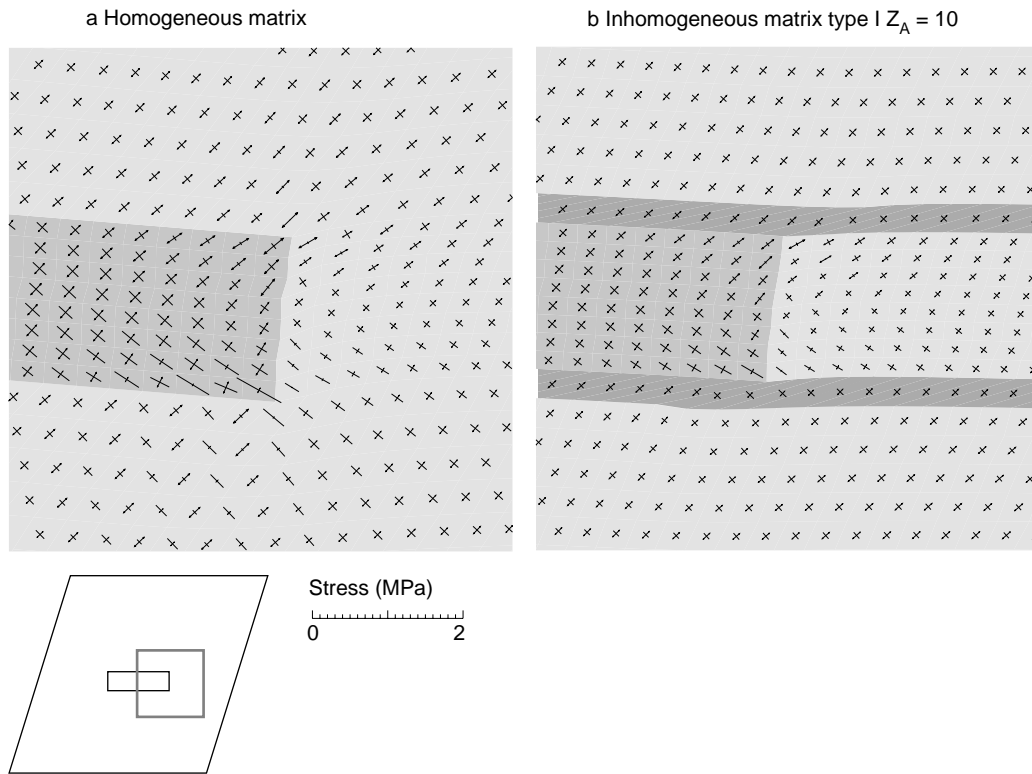


Figure 6.7. Plot of the principal stress tensor as crosses with magnitude and orientation of the principal stresses, for experiments with a homogeneous matrix with power-law rheology and with inhomogeneous matrix I with  $Z_A = 10$ .

### 6.3.1.3 Soft object-matrix boundary

In the experiments with a soft object-matrix boundary high strain and strain rates are found on each side of the object (Fig. 6.8). This effect is more pronounced along the upper and lower boundary of the object and less on the sides of the object. Deformation in the remainder of the matrix is very homogeneous. The experiments with a soft object-matrix boundary also results in a reduction of the rotation rate compared to the homogeneous model (Fig. 6.4c), with  $\Omega_{\text{rel}} = 0.71$ . This rotation rate, for the model with  $Z_A = 10$ , is comparable to  $\Omega_{\text{rel}}$  in inhomogeneous matrix I or II with  $Z_A = 2$ .

The effect of slip on the object-matrix boundary has been studied in analogue experiments (Ildefonse and Mancktelow 1993) and in numerical experiments (Pennacchioni et al. 2000). The analogue experiments of Ildefonse and Mancktelow (1993) have shown a reduction of the rotation rate for rectangular rigid objects in simple shear deformation, compared to theoretical rotation rates. In our experiments the boundary between object and matrix has weak properties. Although slip on the boundary is not allowed, the effect on the rotation rate of the object is similar. Strain is localised at the boundaries of the object, especially the upper and lower boundary, leading to a value of  $\Omega_{\text{rel}} < 1$ .

#### 6.3.1.4 Mohr-Coulomb matrix

The results from the experiments with a homogeneous Mohr Coulomb matrix material show strong strain localisation in several, 1-2 unit wide shear bands in the model (Fig. 6.9). These shear bands largely accommodate the deformation, while the areas between these bands remain almost undeformed. Both in the model with a rectangular object and with a square object shear bands developed along the upper and lower boundary of the object. At the left and right side of the model folds developed, which is attributed to the boundary constraints. The length/width ratio of the model with a Mohr-Coulomb matrix is three, because strong strain localisation is only seen in a model with high length/width ratio. The zones of high finite strain are not always zones of high strain rate (Fig. 6.9), indicating that the distribution of the strain rate is not constant through time. In the Mohr-Coulomb matrix the square object and the rectangular object both hardly rotate, the object is orientated within  $0.12^\circ$  of its initial position for the rectangular object and  $0.51^\circ$  for the square object during the whole experiment. The rotation rate of the object in this matrix is not constant in value and in direction (Fig. 6.4a). The strong partitioning of the deformation probably prevents rotation of the object, similar to the model of Bell et al. (1992).

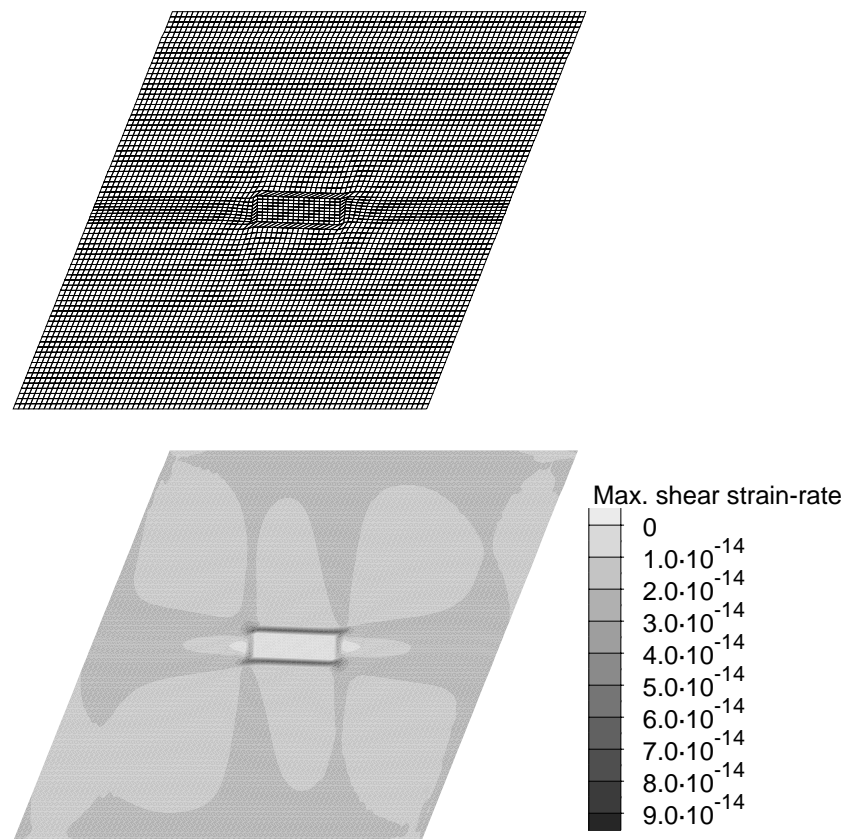


Figure 6.8. Deformed grid and distribution of the maximum strain rate after a finite strain of  $\gamma = 0.4$  for the experiments with a power-law viscous matrix material with a soft layer around the rectangular object.

## Mohr Coulomb

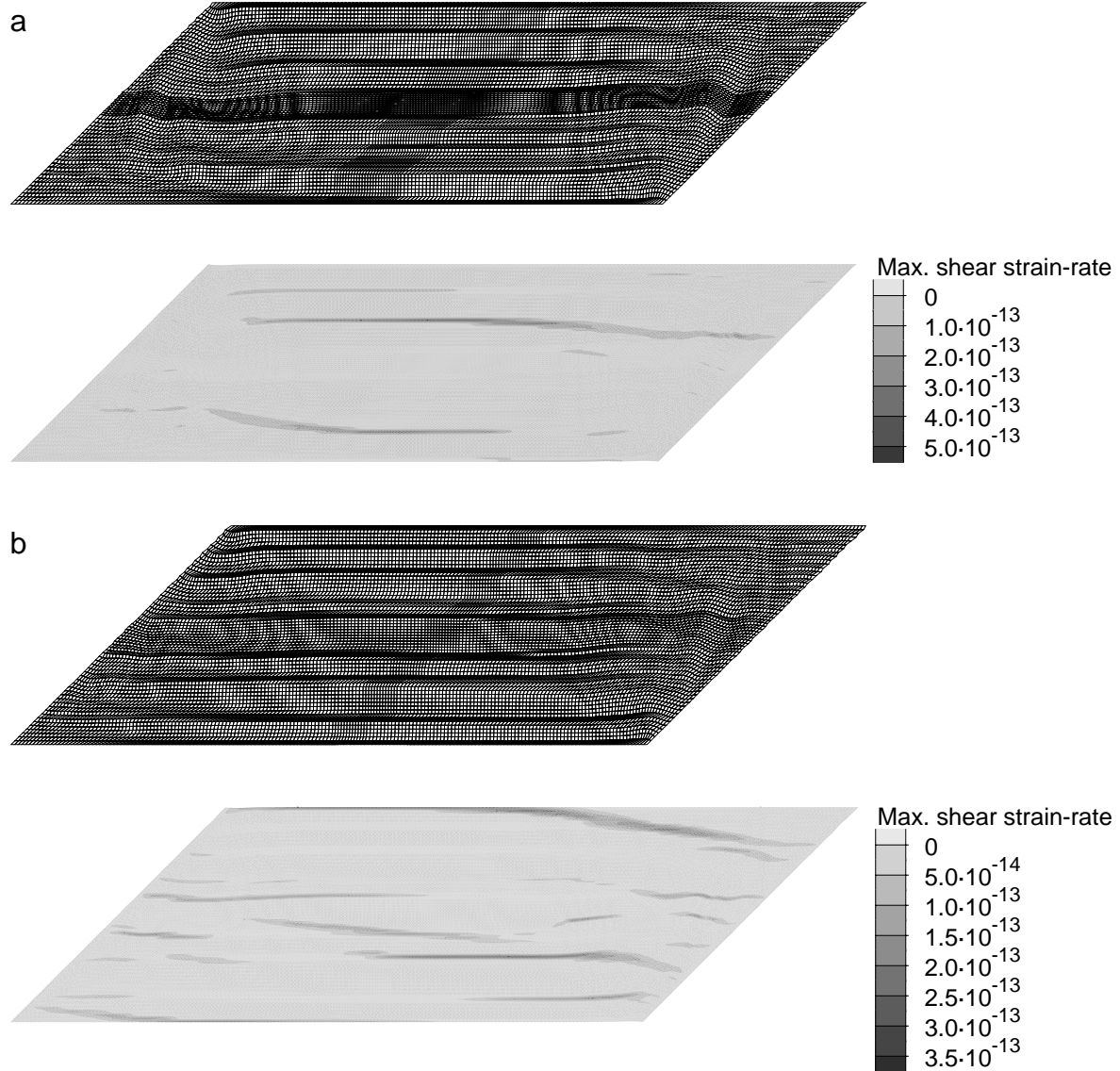


Figure 6.9. Deformed grid and distribution of the maximum strain rate after a finite strain of  $\gamma = 1$  for experiments with a Mohr-Coulomb matrix material with homogeneous properties and a rectangular object (a) and a square object (b). Notice that high finite strain and high strain rate zones only partly coincide.

### 6.3.2 Laterally unconstrained boundaries.

The effect of unconstrained velocity at the side of the boundary is tested for the power-law and Newtonian viscous matrix without and with two weaker zones and with a rectangular object. The results for the experiments with a power-law and a Newtonian viscous matrix are very similar (Fig. 6.10). The deformed grids resulting from these experiments show that there is a significant movement in the y-direction on the sides of the model, in the positive y-direction at the left and in the negative y-direction at the right side of the model (Fig. 6.10). The units at the side of the model do not change their shape significantly, except in the lower left and upper

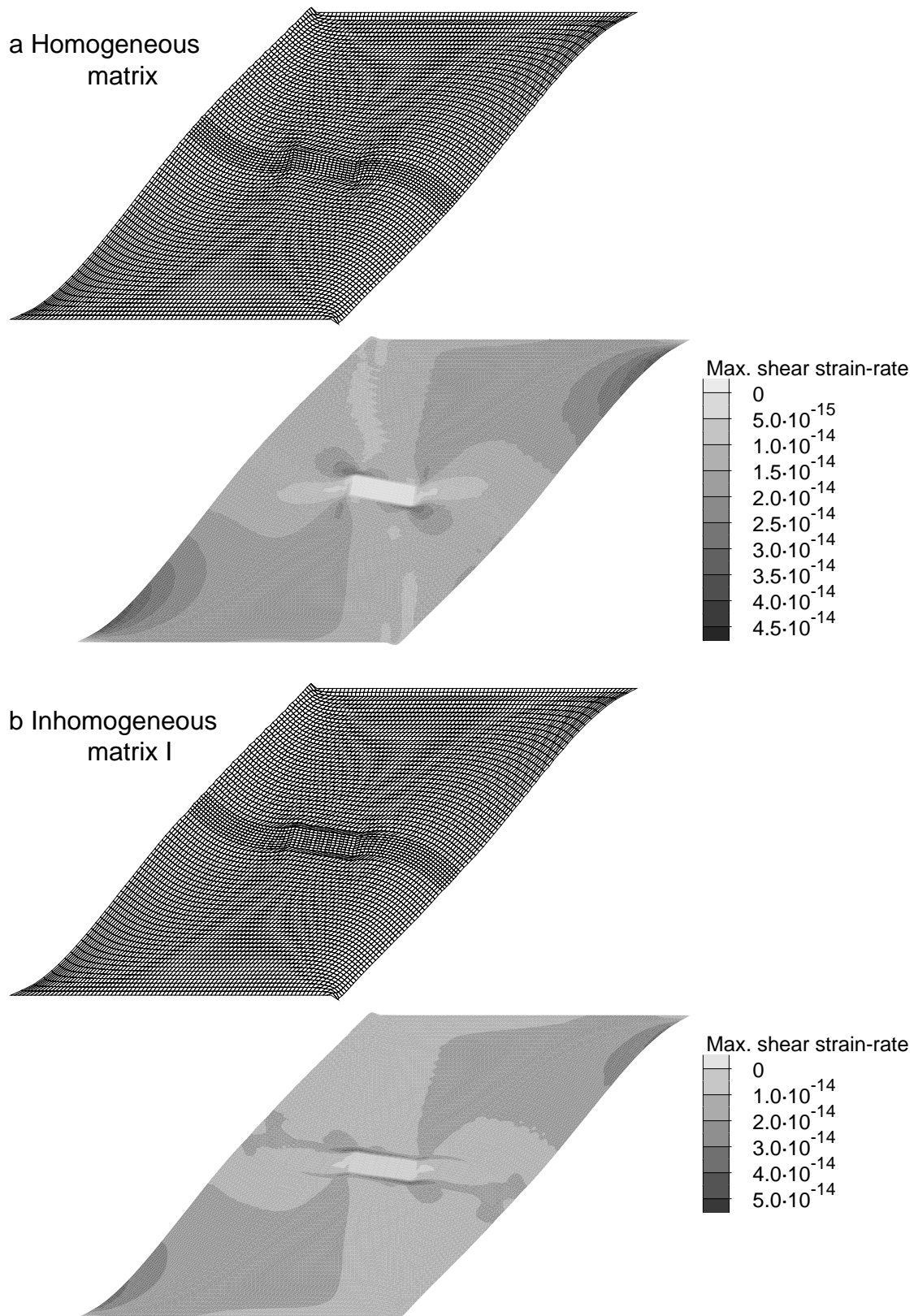


Figure 6.10. Deformed grid and distribution of the maximum strain rate after a finite strain of  $\gamma = 1$  for the experiments with a power-law viscous matrix material a rectangular object, with laterally unconstrained velocities and with homogeneous properties (a) or inhomogeneous properties (b).

right corner, but have a high rotational component compared to the rotation of the units in the models with constrained velocity at the sides of the model. The effect of the weak zones is reduced due to this rotation. Strong strain localisation in the weaker zones is only observed in the middle of the model.

The effect of unconstrained velocities at the sides of the model is a higher rotation rate of the rigid object. For the experiments with a Newtonian viscous matrix and a rectangular object, the rotation rate is about 60% higher compared to the experiments with constrained velocities at the side of the model (Fig. 6.4c). For the experiments with a power-law matrix the rotation rate is about 50% higher. The increase in rotation rate is similar for the experiments with homogeneous and with inhomogeneous matrix properties. For the experiments with a square object there is also an higher rotation rate compared to the model with constrained boundary conditions, but less significant: 15% for the Newtonian viscous model and 11% for the model with a power-law rheology.

Unconstrained velocities at the sides of the model resulting in deformation of the matrix material with a large velocity component in the y-direction at the sides of the model, does not seem like something realistic for a model of a natural mylonitic rock. However, in analogue experiments these boundary conditions can be realised, which would give wrong values for the rotation of objects.

## 6.4 Discussion

In this part the results from the numerical experiments are discussed and compared to microstructures of natural rocks with mica fish, presented in the previous chapters. The mylonites with mica fish (chapter 2) were deformed under greenschist facies conditions and consist of a quartz-rich matrix with single fish-shaped mica crystals and trails of fine-grained mica. The mica grains all have similar orientations with respect to the mylonitic foliation, which seems to be a stable orientation (Eisbacher 1970, Lister and Snoke 1984, Chapter 2 and 5). The quartz rich matrix is dynamically recrystallised and has a homogeneous shape and crystallographic preferred orientation, which suggests that the finite strain distribution is relatively homogeneous through the matrix. Mica trails that link boudinaged mica fishes may indicate strain localisation along discrete bands (C-planes, Lister and Snoke 1984), but could also be explained as boudin-necks connecting boudins (individual mica fish) formed by extension in relatively homogeneous flow. Quartz under greenschist conditions is thought to deform according to a power-law flow law (Poirier 1985, Kirby and Kronenberg 1987). However, numerical experiments presented here and those of Bons et al. (1997), and Pennacchioni et al. (2000) have shown that a homogeneous power-law matrix rheology alone cannot explain the rotational behaviour of the mica fish. Additional factors must play a role.

Results of the numerical experiments presented here have shown that an inhomogeneous (power-law) viscous matrix, or a Mohr-Coulomb matrix both lead to a reduction in the rotation rate of the object. An inhomogeneous matrix can be a matrix with soft layers in the matrix or with a soft layer around the object. Strain will be localised in the soft layers. The matrix in experiments with inhomogeneous matrix II also has characteristics of an anisotropic matrix.

The homogeneously distributed soft layers will give the matrix different properties in the x-direction and in the y-direction. In a Mohr-Coulomb matrix the strain is localised in discrete shear bands. These results indicate that elongated rectangular objects can have a stable orientation in a matrix where strain is localised.

In the mylonites discussed in chapter 2 there is no evidence for partitioning in low strain and high strain zones. A homogeneous crystallographic and shape preferred orientation of the quartz is observed everywhere in the matrix. Softening mechanisms are most likely at high differential stress and strain rate localities in natural mylonites (White et al. 1980). The experiments have shown that the highest differential stress and strain rate are at the object matrix interface, especially on the upper and lower boundary of an object. A reduction in matrix strength there will lead to a reduction in rotation rate of the object. In the case of mica fish, other processes like dynamic recrystallisation at the rim (Chapter 2) could also reduce the coherence between the object and the matrix and therefore reduce the rotation rate of the object (Passchier and Simpson 1986, Ildefonse and Mancktelow 1993).

These results indicate that the localisation needed to get a stable orientation of elongated objects in simple shear is not explained by a homogeneous power-law rheology of the matrix. This suggests that a single strain-independent power-law equation is insufficient to describe the behaviour of the matrix material in these rocks. The bulk rheology of the material can be described with a power-law flow behaviour (Poirier 1985, Kirby and Kronenberg 1989), but details of the microstructure in these rocks can not be explained with a power-law rheology of the matrix only. The stable orientation of mica fish in mylonitic rocks is probably the result of strain localisation around the object, anisotropy of the matrix and a reduced coherence on object-matrix boundary.

## 6.5 Conclusions

The effect of matrix rheology, the existence of inhomogeneties, boundary conditions and a soft layer around an object on strain distribution and on rotation rate of rigid objects is studied with numerical experiments. A reduction in the rotation rate of the object compared to the object in a homogeneous power-law matrix is observed when soft layers are introduced in the matrix, with a soft layer around the object and with a Mohr-Coulomb matrix rheology. In each of these cases strain is localised around the object. These results indicate that object can reach a stable orientation when strain is localised around the object, which suggests that minor parts of the rheology can have a significant effect on the microstructure. These results have consequences for the behaviour of rigid objects in mylonite zones, the preferred orientation of objects such as mica fish can not be explained with a homogeneous power-law viscous rheology of the matrix.





## Chapter 7

### General conclusions and suggestions for future research

#### 7.1 General conclusions

The aim of the project described in this thesis was to understand the development of mica fish, and to derive information about flow kinematics and rheological behaviour of mylonites from this microstructure. The following steps have been taken to achieve this: (a) field observations, (b) analogue modelling and (c) numerical modelling. The general conclusions are given in this section.

##### *7.1.1 Mechanisms for evolution of mica fish*

A large range of minerals with different physical properties can form fish-shaped structures. Study of fish-shaped structures that developed in different minerals and from different locations showed that they all have an asymmetrical shape and their long axis is consistently inclined with respect to the mylonitic foliation, which makes these structures reliable shear sense indicators. Mechanisms involved in the formation of mica and other mineral fish can be divided in two groups: (1) mechanisms to deform single crystals into a fish-shape, and (2) mechanisms to split a large crystal in smaller parts. The first group of mechanisms include intracrystalline deformation, rigid body rotation, bending and folding, dynamic recrystallisation at the rim of the crystal, and pressure solution accompanied by local growth (Lister and Snoke 1984, Mares and Kronenberg 1993, Passchier and Trouw 1996, Chapter 2). The importance of each mechanism depends mainly on the properties of the material. Most mechanisms are enhanced at the high normal stress side of the fish (the instantaneous shortening direction), which can be seen for example in K-feldspar with myrmekite (Simpson and Wintsch 1989) and also in tourmaline with dissolution at the corners of the crystal. For some minerals it seems that the fish-shape only represents a certain stage in their evolution, before the mineral fish is completely recrystallised, e.g. in the case of biotite (Passchier 1985), or destroyed by other grain size reducing mechanisms.

Mechanisms to split a large crystal in smaller ones are discussed in Chapter 2 and by Lister and Snoke (1984). Possible mechanisms include: development of micro-cracks usually parallel to the basal planes, followed by synthetic or antithetic sliding of the particles along each other; separation of a part from its parent by an antithetic listric fault; and isoclinal folding of the fish, followed by break off along the fold hinge and transport of the parts past each other. These mechanisms are all based on inhomogeneous flow in and around the mineral fish. Transport of fragments along the grain boundary of another mineral fish is only possible if there is a micro-shear zone along this boundary. The combination of splitting and mechanisms to deform single crystals give the fish-shaped minerals their characteristic geometry.

### 7.1.2 Preferred orientation of objects

Measurements of the long axis of mica and tourmaline fish have shown that on average the long axis of the fish has an angle of about 10-15° with the flow plane (Chapter 2, 5). This average orientation can not be explained with analytical equations of Jeffery (1922) and Ghosh and Ramberg (1976) for the rotation of rigid ellipsoids in viscous flow. According to these equations, rigid objects do not have a stable orientation in simple shear flow and minimum rotation rate is reached when the long axis of the object is parallel to the flow plane. In general flow ( $0 < W_k < 1$ ), a stable position is possible, but the orientation of elongate object is different from that of mica fish. Analogue and numerical experiments were performed to investigate which factors are important for the observed preferred orientation of mica fish.

Two different matrix materials were used in the analogue experiments, a Newtonian viscous (PDMS) and a Mohr-Coulomb material (tapioca pearls). Rigid parallelogram-shaped object were used as an analogue for the mineral fish. The kinematic vorticity number ( $W_k$ , Means 1980) and the aspect ratio of the object were varied. The results for the experiments with a PDMS matrix are similar to the analytical solutions of Jeffery (1922) and Ghosh and Ramberg (1976). In contrast, the objects rotated towards stable orientations in experiments with a matrix consisting of tapioca pearls. The stable orientations of the objects in simple shear deformation in tapioca pearls are similar to the data from natural mica fish (Fig 5.10). The orientation of the object is a function of its aspect ratio. The deformation in the Mohr-Coulomb matrix material is localised in discrete shear bands. The longest side of the object is parallel to these shear bands in the simple shear experiments. These results indicate that localisation of deformation in shear bands is probably a crucial factor for the orientation of mica fish and related structures in mylonites.

Experiments with the finite difference code FLAC were performed to investigate the role of matrix rheology on the strain distribution and object rotation in more detail. Experiments with different rheological models for the matrix and with inhomogeneous matrix properties were performed. A rigid rectangular or square object is initially parallel to the model boundaries. These experiments confirm that a homogeneous power-law matrix cannot explain the observed preferred orientation of mica fish. The existence of soft layers in a power-law matrix, in the form of layers parallel to the flow plane or of a soft layer around the object, reduce the rotation rate compared to the rotation rate of an object in a homogeneous power-law matrix. However, the existence of a soft layer around the object or of soft layers directly above and below the object has only limited influence on the rotation rate of the object. A homogeneous distribution of soft layers in the matrix, resembling an anisotropic matrix, has a mayor effect on the rotation rate. Contrary to the other matrix materials, objects in a Mohr-Coulomb matrix material do not rotate and finite strain in the matrix is partitioned in zones with high finite strain and zones with very low finite strain.

The results from the analogue and numerical experiments combined with the study of natural mica fish indicate that the stable orientation of mica fish in mylonitic rocks must be the result of a combination of strain localisation around the object, anisotropy of the matrix and reduced coherence on the object-matrix boundary.

### 7.1.3 Implications for rheology of mylonites.

The mechanisms to split mica fish in smaller parts, deduced from the microstructures observed in thin sections, imply that localisation of strain must occur on the mica fish-matrix boundary and on the trails of fine-grained mica forming the tails of the mica fish. The analogue and numerical experiments indicate that strain localisation is required to get a stable orientation for the rigid elongated objects in simple shear experiments. This is supported by the observation that the stable orientation of the objects in experiments with localisation in the matrix is similar to the orientation of mica fish in mylonitic rocks. Usually, a power-law rheology is assumed for mylonitic rocks (e.g. Poirier 1985, Kirby and Kronenberg 1987). However, the results of the analogue and numerical experiments indicate that the description of the rheology of a mylonitic rock by a single strain-independent power-law equation is inadequate to explain the formation of mica fish structures. There is localisation beyond that which can be explained by a time-independent power-law rheology. This localisation is probably the result of softening in high differential stress zones at the boundary of a rigid object. An additional factor is that the matrix in mylonites with mica fish is not isotropic, and this also has an effect on the rotation of the mica fish. It is therefore hard to tell to what extent power-law rheology is adequate to describe the rheology of mylonitic rocks. Flow laws are normally deduced in coaxial rock deformation experiments, where localisation is suppressed. Possibly, deformation experiments where localisation is possible would give different results. It is possible, however, that a power-law rheology is adequate to describe the bulk rheology of a mylonitic rock, but the rheology fluctuates on a smaller scale influencing details of the resulting microstructure, like the orientation of mica fish.

## 7.2 Suggestions for future research

The results described in this thesis have brought up a number of question and possibilities for future research.

1. Deformation mechanisms discussed in Chapter 2 are inferred from observations of structures in thin sections. For some of the processes experimental data are available, but especially the relative importance of each mechanism remains unclear. Deformation experiments with the different minerals are necessary to get a better understanding of the interaction between different mineral fish forming mechanisms.
2. The development of a new deformation apparatus for general flow and the use of tapioca pearls as a matrix material to model microstructures in mylonitic rocks have brought new possibilities for analogue experiments. The experiments described in this thesis are done with one rigid object in the matrix. Interacting rigid objects in either simple or pure shear in a viscous matrix have different rotation behaviour as single objects under similar conditions (Ildefonse et al. 1992, Ildefonse and Mancktelow 1993). Experiments with interacting objects in general shear or in a matrix of tapioca pearls will probably improve the understanding of the development of fabrics in mylonitic rocks.

3. The behaviour of rigid objects in the analogue experiments was a function of their aspect ratio, the matrix rheology, and also of the vorticity number of the deformation. The experiments presented in this thesis are not sufficient to give a complete model for vorticity analysis in rocks, because it was not yet fully clarified which factor determines the stable orientation of the objects in the experiments with tapioca pearls as a matrix material. More experiments, maybe with different matrix materials, and numerical simulations could help to establish what determined the stable orientation of these objects and this could lead to a model to determine the vorticity number of deformation in mylonitic rocks.
4. The results of the analogue and numerical experiments with rigid objects suggest that strain localisation around the object is crucial to explain the preferred orientation of mineral fish in mylonitic rocks. Deformation in a natural mylonite is by completely different mechanisms than deformation in the analogue materials. In the numerical models the inhomogeneous properties of the matrix were given prior to the deformation and were not changed during the experiment. Experiments with crystalline rock analogues or with computer models that model different deformation mechanisms, including softening processes (Jessell et al. 2001), are needed to gain a better understanding of the localisation processes in these rocks.
5. The experiments presented in this thesis have shown that the strain localisation needed to get a stable orientation for elongated objects cannot be explained with a homogeneous power-law rheology of the matrix. Usually rheological data for rocks are determined in coaxial deformation experiments with a limited amount of finite strain. In coaxial experiments, strain localisation is suppressed. Experiments with non-coaxial deformation and higher finite strain (e.g. Bos 2000, Paterson and Olgaard 2000) should be carried out and might give different results for the rheology of rocks.

## Appendix: Deformation apparatus

In this appendix, a detailed account on the programs written for the deformation apparatus described in Chapter 3 is given. The appendix includes a general introduction to the different types of transpressional regimes, a User Manual, technical specifications and settings used in experiments described in Chapter 3 and Chapter 5.

### A1 General Introduction

Transpression is broadly defined as a combination of perpendicular components of pure and simple shear. In three dimensions such a deformation can be described by the following deformation tensor under the assumption that shear occurs exclusively in the x-direction:

$$D = \begin{bmatrix} k_1 & \Gamma_{xy} & \Gamma_{xz} \\ 0 & k_2 & \Gamma_{yz} \\ 0 & 0 & k_3 \end{bmatrix}$$

Where  $k_1$ ,  $k_2$  and  $k_3$  represent extensions along the x, y, and z coordinate axes, respectively, and the off-diagonal terms represent elements of effective shear deformation (Tikoff and Fossen, 1993).

The 5 programs available right now model 5 different regimes of transpression assuming shear in the x direction and constant volume ( $k_1 * k_2 * k_3 = 1$ ;  $V_n = 1$  (Passchier 1998)). All programs except Program A model transpressional deformation where the relative components of pure and simple shear i. e. the vorticity number can be varied (e.g. Means et al. 1980, Passchier 1986, Bobyarchick 1986).

Program A (*A/ Simple shear.vi*):

Simple shear;  $k_1 = k_2 = k_3 = 1$ .

Program B (*Transpression B.vi*):

Transpression; extension along the z-axis and  $k_1 = 1$ .

Program C (*Transpression C.vi*):

Transpression; extension in the x and z direction and  $k_1 = k_3$ .

Program D (*Transpression D.vi*):

Transpression; plane strain deformation; no extension along the z-axis ( $k_3 = 1$ ).

Program E (*Transpression E.vi*):

Transpression; shortening along the y and z axis with  $k_2 = k_3$ .

For all five deformation types (Fig. A1) the movement of the 6 stepping motors of the apparatus (see Fig. 3.2) is calculated for each time step depending on the current dimensions of the deformation box and using dextral shear along the x-axis.

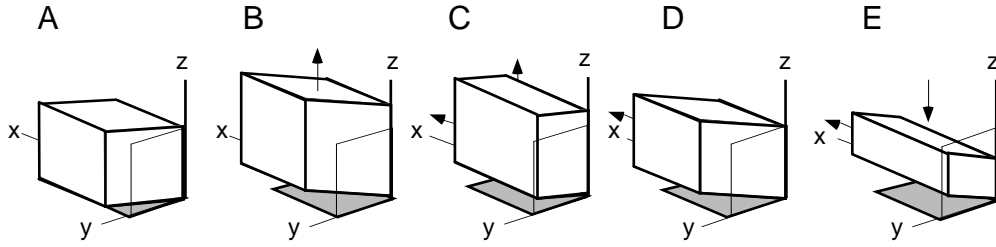


Figure A1. Schematic illustration of the 5 different types of transpressional regimes for which LabView programs exist.

#### Calculations:

Based on the deformation matrix given above for each of the programs the movement of the motors i.e. the movement along the x, y and z direction can be calculated. We adopt a similar approach as Tikoff and Fossen (1993) and base our calculation on the division of deformation in a pure and simple shear component as shown below. With this knowledge the extension or shortening along each of the 3 axis can be calculated for each time step. For a specific vorticity number the pure and simple shear components along the different axes must satisfy the following equation.

$$W_k = \frac{\sqrt{(\dot{\gamma}_{yz})^2 + (\dot{\gamma}_{xz})^2 + (\dot{\gamma}_{xy})^2}}{\sqrt{2\left[(\dot{\epsilon}_1)^2 + (\dot{\epsilon}_2)^2 + (\dot{\epsilon}_3)^2\right] + (\dot{\gamma}_{yz})^2 + (\dot{\gamma}_{xz})^2 + (\dot{\gamma}_{xy})^2}}$$

As it is assumed that shear only occurs along the x axis  $\dot{\gamma}_{xz}$  and  $\dot{\gamma}_{yz}$  are zero. For each of the programs this equation is modified to meet the definition of the 5 different deformation regimes (see above).

Program A:

Simple shear;  $W_k=1$ .

Program B:

$$W_k = \frac{\sqrt{(\dot{\gamma}_{yz})^2}}{\sqrt{2\left[(\dot{\epsilon}_2)^2 + (\dot{\epsilon}_3)^2\right] + (\dot{\gamma}_{yz})^2}}$$

Program C:

$$W_k = \frac{\sqrt{(\dot{\gamma}_{yz})^2}}{\sqrt{2\left[2 \cdot (\dot{\epsilon}_1)^2 + (\dot{\epsilon}_2)^2\right] + (\dot{\gamma}_{yz})^2}}$$

Program D:

$$W_k = \frac{\sqrt{(\dot{\gamma}_{yz})^2}}{\sqrt{2\left[(\dot{\epsilon}_1)^2 + (\dot{\epsilon}_2)^2\right] + (\dot{\gamma}_{yz})^2}}$$

Program E:

$$W_k = \frac{\sqrt{(\dot{\gamma}_{yz})^2}}{\sqrt{2\left[(\dot{\epsilon}_1)^2 + 2 \cdot (\dot{\epsilon}_2)^2\right] + (\dot{\gamma}_{yz})^2}}$$

## A2 User Manual

Open one of the 5 programs, located at folder LabView -> programmes for shearapparatus (e.g. *Transpression B.vi*). For each program the control panel shows five types of boxes (Fig. A2)

- 1) Green boxes are inputs concerning the initial dimensions of the deformation box,
- 2) yellow boxes specify the deformation rate, vorticity number and amount of final deformation,
- 3) red box characterizes the timing of a signal (e.g. to alert the user to take pictures),
- 4) orange boxes and diagram provide information about the deformation during the experiment, remaining time of the experiment and to next beep,
- 5) grey box specifies the slot for the hardware card (PCI-STEP-4OX).

The user should ONLY change values in the green, yellow and red boxes. If by accident the slot number is changed the motors will not respond. Resetting the slot number to 3 fixes the problem. Additionally, there is an emergency STOP button, which can be pressed (mouse click) if desired.

Once an experiment has finished or is stopped manually by the user (emergency STOP), open program *Back to 0.vi* (Fig. A3). This program will move the deformation box to its initial position. Here, the velocity of movement is given by the user.

Never quit LabView or turn off the computer before the deformation box is returned to its initial position, otherwise the true initial position of the box will not be “remembered” by the program. If for unforeseen reason this does happen, the program *Step Axis Control Simple* (Fig. 3) can be used to reposition the deformation box. The same program can be used to reposition the deformation box, e.g. if a different initial position is required. After repositioning, restart the computer so that the position is recognized by LabView as the new default zero position. Figure A4 shows axis numbers as used by the programs.

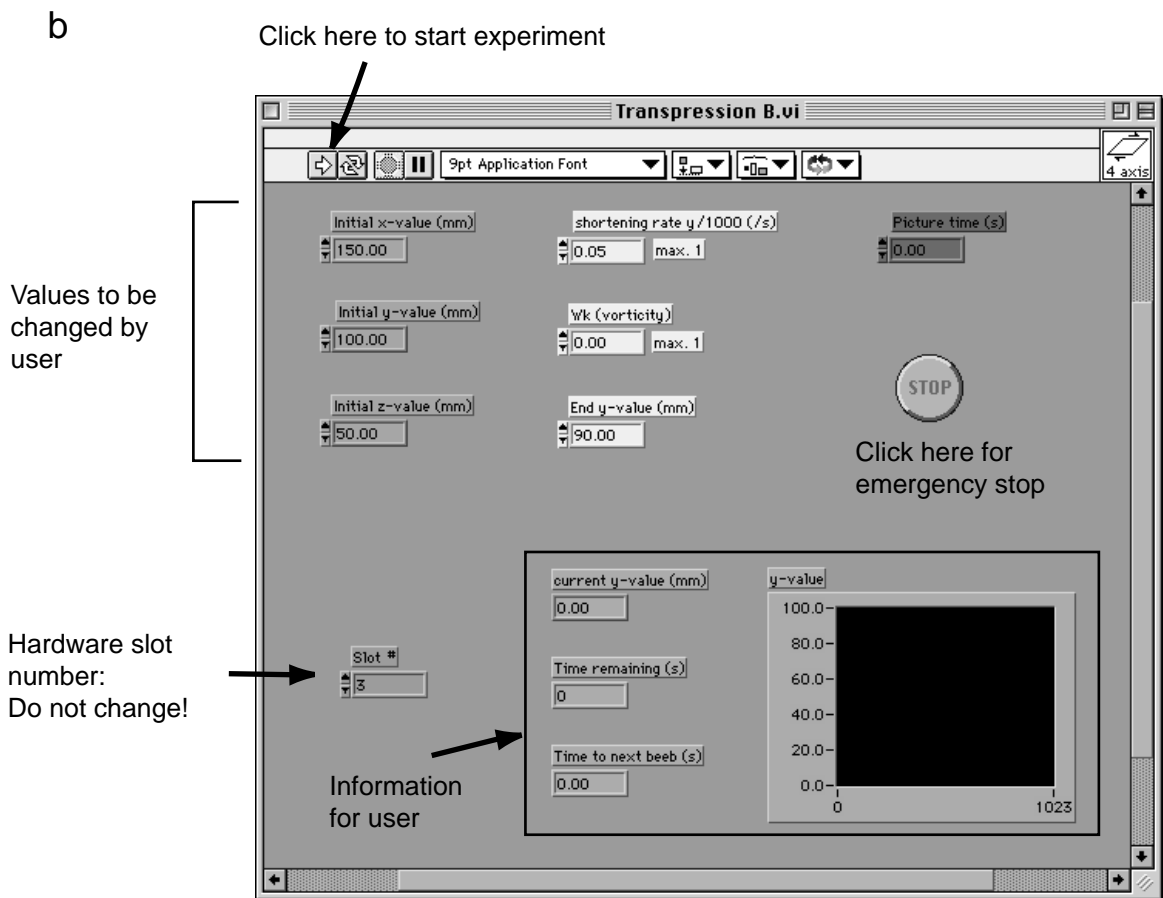
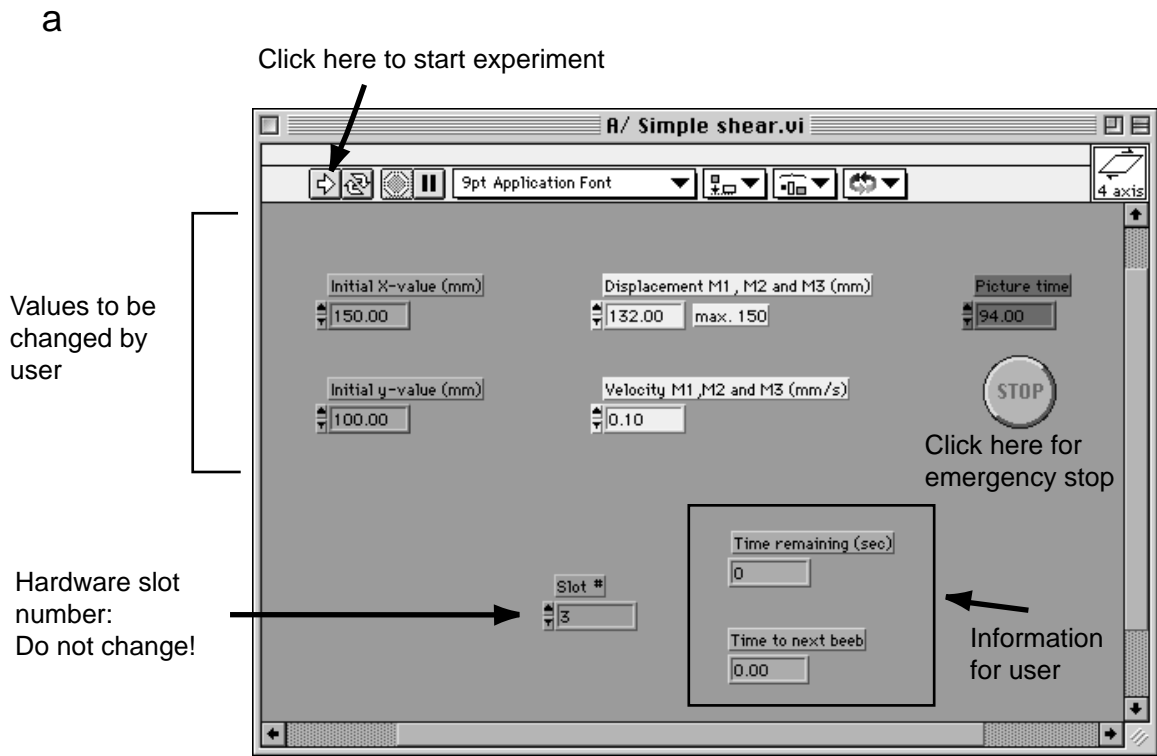


Figure A2. (a) Control panel of program A (A/Simple Shear.vi), (b) Control panel of program B (Transpression B.vi).



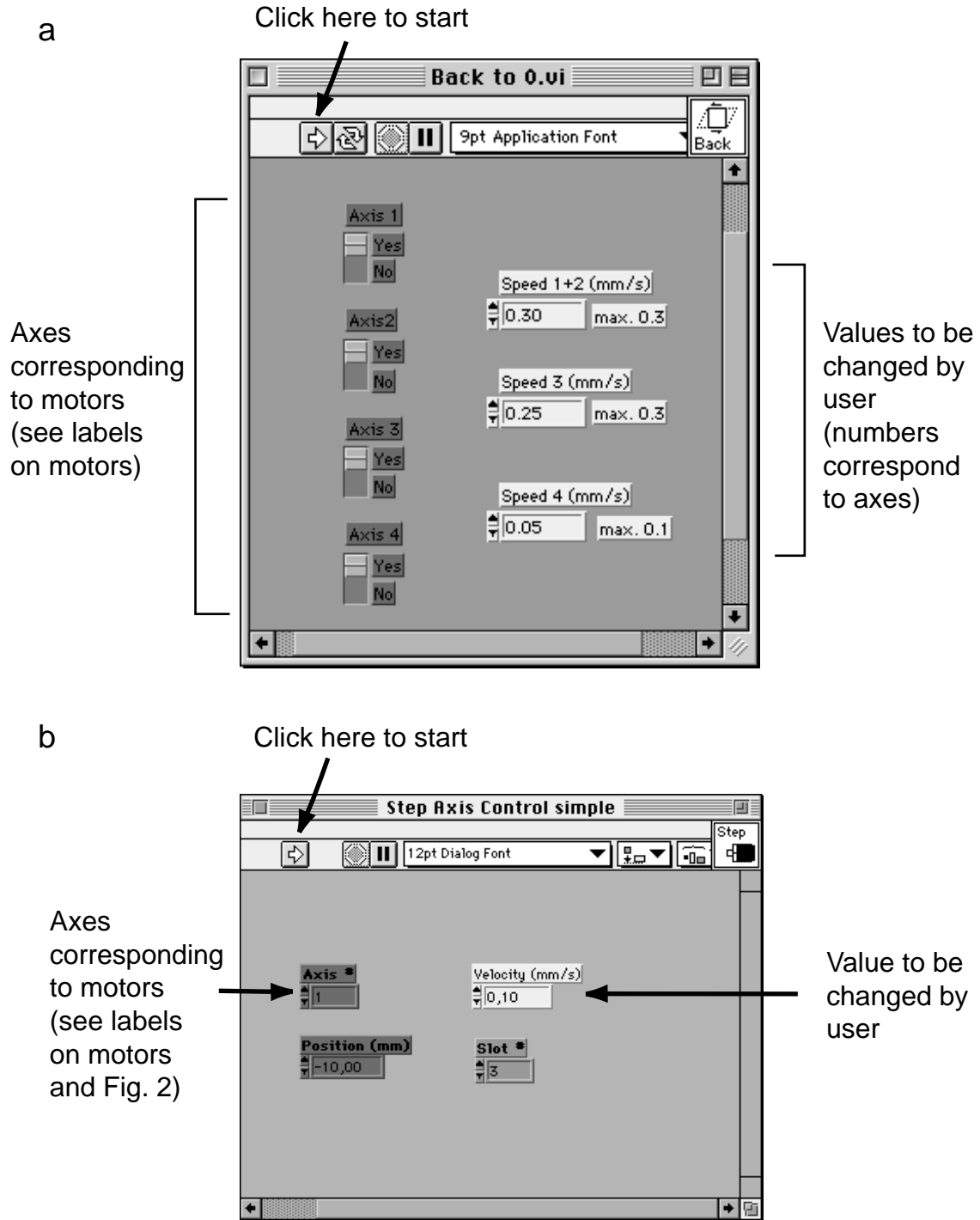


Figure A3. (a) Control panel of Back to 0.vi, (b) Control panel of Step Axis Control Simple

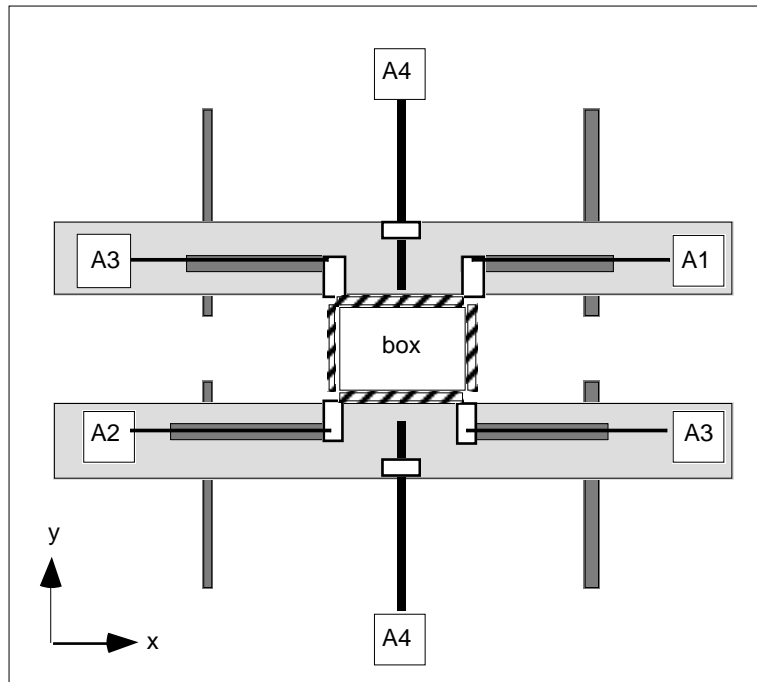


Figure A4. Diagram illustrating the axis numbers (e.g. A1) used by the LabView programs.

### A3 Technical specifications

Product	Description	Manufacturer
LabView 5.0	Graphical Programming for Instrumentation	National Instruments Germany GmbH Konrad-Celtis-Str. 79 81369 München 089-7413130
ValueMotion	Additional LabView library for stepping motors	National Instruments
PCI-STEP-4OX 4-Axis Open Loop Step controller for Macintosh	Hardware card to communicate with power device and computer	National Instruments
Power Device Connection block CB-50 + MTL-400/6 4 axis multiplier	Electronic link between personal computer and stepping motors	MovTec Stütz & Wacht GmbH Goldschmiedeschulstr.6 75173 Pforzheim movtex@t-online.de
Stepping Motors MTS-230-E80		MovTec
Carriages	Length 300 mm	Baumarkt, Mainz
PVC platelets and board	different thickness and length	Cadillac Plastic GmbH, Mainz-Kastel 06134-22036
Springs: Zugfeder 12/3/5 Zugfeder 11/5/2	Length $l_0$ 128 mm, R 0.11 N/mm Length $l_0$ 60.8 mm, R 0.09 N/mm	Federntechnik Knörzer GmbH Postfach 7282 72785 Pfullingen 07121-97840
Shaft 270-164	M6, messing	RS Components GmbH Hessenring 13b 64546 Mörfelden-Walldorf rs-gmbh@rs-components.com
Shaft joint 689-007	Shaft diameter 6 mm	RS Components GmbH
Latex sheet	Thickness 0.35 mm, Width $\pm 21$ cm, Length $\pm 28$ cm	Skintight, Netherlands linda@skintight.nl

**A4 Used set-up for experiments***Chapter 3, flow tests, flow pattern:*


---

Program type	D
Initial dimensions x, y, z [mm]	150, 100, 100
$W_k$	0.6 and 0.8
Shortening rate [ $s^{-1}$ ]	$3.3 \times 10^{-4}$
End x value [mm]	225
Matrix material	PDMS

---

*Chapter 3, flow tests, area of homogeneous deformation:*


---

Program type	D
Initial dimensions x, y, z [mm]	150, 100, 100
$W_k$	0.6 and 0.8
Shortening rate [ $s^{-1}$ ]	$2.0 \times 10^{-4}$ , $3.3 \times 10^{-4}$ , $4.7 \times 10^{-4}$
End x value [mm]	225
Matrix material	PDMS and Rhodorsil gomme

---

*Chapter 3, flow tests, rotation of sphere:*


---

Program type	A/ simple shear
Initial dimensions x, y, z [mm]	150, 100, 100
$W_k$	1
Strain rate [ $s^{-1}$ ]	$1.0 \times 10^{-3}$
Displacement along x-axis [mm]	100
Matrix material	PDMS
Object dimensions [mm]	Sphere $\varnothing$ 8 mm
Object material	Plexiglas

---

*Chapter 5, experiments with PDMS,  $W_k = 1$ .*


---

Program type	A/ simple shear
Initial dimensions x, y, z [mm]	210, 70, 100
$W_k$	1
Strain rate [ $s^{-1}$ ]	$2.0 \times 10^{-3}$
Displacement along x-axis [mm]	122.5
Matrix material	PDMS
Object dimensions [mm]	Different sizes
Object material	India rubber

---

*Chapter 5, experiments with PDMS,  $W_k = 0.8$ .*


---

Program type	D
Initial dimensions x, y, z [mm]	150, 100, 100
$W_k$	0.8
Shortening rate [ $s^{-1}$ ]	$3.3 \times 10^{-4}$
End x value [mm]	225
Matrix material	PDMS
Object dimensions [mm]	Different sizes
Object material	India rubber

---

*Chapter 5, experiments with Tapioca pearls,  $W_k = 1$ .*


---

Program type	A/ simple shear
Initial dimensions x, y, z [mm]	150, 100, 100
$W_k$	1
Strain rate [ $s^{-1}$ ]	$2.0 \times 10^{-3}$
Displacement along x-axis [mm]	150
Matrix material	Tapioca pearls
Object dimensions [mm]	Different sizes
Object material	India rubber

---

*Chapter 5, experiments with Tapioca pearls,  $W_k = 0.95, 0.8$  and  $0.6$ .*


---

Program type	D
Initial dimensions x, y, z [mm]	150, 100, 100
$W_k$	0.95, 0.8 and 0.6
Shortening rate [ $s^{-1}$ ]	$3.3 \times 10^{-4}$
End x value [mm]	225
Matrix material	Tapioca pearls
Object dimensions [mm]	Different sizes
Object material	India rubber

---

## References

- Abbassi, M.R. and Mancktelow, N.S. 1990. The effect of initial perturbation shape and symmetry on fold development. *Journal of Structural Geology* 15, 293-307.
- Anma, R. 1997. Oblique diapirism of the Yakushima granite in the Ryukyu arc, Japan. In: *Granite: From segregation of melt to emplacement fabrics*, edited by J.L. Bouchez, D.H.W. Hutton and W.E. Stephens, 295-318.
- Anma, R. and Sokoutis, D. 1997. Experimental pluton shapes and tracks above subduction zones. In: *Granite: From segregation of melt to emplacement fabrics*, edited by J.L. Bouchez, D.H.W. Hutton and W.E. Stephens, 319-334.
- Askeland, D.R. 1990. *The Science and Engineering of Materials*. Chapman and Hall, London.
- Azor, A., Ferando Simancas, J., Exposito, I., Gonzalez Lodeiro, F. and Martinez Poyatos, D.J. 1997. Deformation of garnets in a low-grade shear zone. *Journal of Structural Geology* 19, 1137-1148.
- Beam, E.C. and Fischer, D.M. 1999. An estimate of kinematic vorticity from rotated elongate porphyroblasts. *Journal of Structural Geology* 21, 1553-1559.
- Bell, T.H. 1981. Foliation development - the contribution, geometry and significance of progressive, bulk, inhomogeneous shortening. *Tectonophysics* 75, 273-296.
- Bell, T.H. and Etheridge, M.A. 1973. Microstructure of mylonites and their descriptive terminology. *Lithos* 6, 337-348.
- Bell, T.H. 1985. Deformation partitioning and porphyroblast rotation in metamorphic rocks: a radical reinterpretation. *Journal of Metamorphic Geology* 3, 109-118.
- Bell, T.H., Johnson, S.E., Davis, B., Forde, A., Hayward, N. and Wilkins, C. 1992. Porphyroblast inclusion-trail orientation data: eppure non son girate. *Journal of Metamorphic Geology* 10, 295-307.
- Berthé, D., Choukroune, P. and Jegouzo, P. 1979. Orthogneiss, mylonite and non-coaxial deformation of granites: the example of the South Armorican shear zone. *Journal of Structural Geology* 1, 31-42.
- Bestmann, M. 1999. Lattice diffusion creep as a possible deformation mechanism for quartz porphyroclasts within a calcite marble shear zone. Abstract volume deformation mechanisms, rheology, microstructures, 69.
- Bobyarchick, A.R. 1986. The eigenvalues of steady flow in Mohr space. *Tectonophysics* 122, 35-51.
- Bons, P.D. 1993. Experimental deformation of polyphase rock analogues. [Ph.D. thesis] *Geologica Ultraiectina* 110 Utrecht University.
- Bons, P.D. and Jessell, M.W. 1995. Strain analysis in deformation experiments with pattern matching or a stereoscope. *Journal of Structural Geology* 17, 917-921.
- Bons, P.D. and Jessell, M.W. 1999. Micro-shear zones in experimentally deformed octachloropropane. *Journal of Structural Geology* 21, 323-334.
- Bons, P.D. and Urai, J.L. 1995. An apparatus to experimentally model the dynamics of ductile shear zones. *Tectonophysics* 256, 145-164.
- Bons, P.D., Barr, T.D. and ten Brink, C.E. 1997. The development of  $\delta$ -clasts in non-linear viscous materials: a numerical approach. *Tectonophysics* 270, 29-41.
- Bos, B. 2000. *Faults, Fluids and Friction Effect of pressure solution and phyllosilicates on fault behaviour, with implications for crustal rheology* [Ph.D. thesis] *Geologica Ultraiectina* 197 Utrecht University.
- Bretherton, F.P. 1962. Slow viscous motion round a cylinder in a simple shear. *Journal of Fluid Mechanics* 12, 591-613.
- Brun, J.-P., Sokoutis D. and Van Den Driessche J. 1994. Analogue modeling of detachment fault systems and core complexes. *Geology* 22, 319-322.

- Chwang, A.T. and Wu, T.Y.-T. 1975. Hydromechanics of low-Reynolds-number flow. Part 2. Singularity method for Stokes Law. *Rheologica Acta* 25, 380-388.
- Clarck, M.K. and Royden, L.H. 2000. Topographic ooze: Building the eastern margin of Tibet by lower crustal flow. *Geology* 28, 703-706.
- Cruden, A. and Robin, P.-Y. 1999. Analogue models of ductile transpression zones. *Journal of Conference Abstracts* 4, 604.
- Cundall, P. and Board, M. 1988. A microcomputer program for modeling large-strain plasticity problems. In: Swoboda, C. (ed.) *Numerical methods in geomechanics. Proc. 6<sup>th</sup> Int. Conf. On Numerical Methods in Geomechanics*, Innsbruck, Austria, 2101-2108.
- Dealy, J.M. and Broadhead, T.O. 1993. Rheometry for Process Control. In: *Techniques in rheological measurement*, edited by Collyer, A. A., Chapman and Hall, Cambridge, 285-331.
- Den Brok, B. and Kruhl, J.H. 1996. Ductility of garnet as an indicator of extremely high temperature deformation: Discussion. *Journal of Structural Geology* 18, 1369-1373.
- Dewey, J., Holdsworth, R.E. and Strachan, R.A. 1998. Transpression and transtension zones. In: Holdsworth, R.E., Strachan, R.A. and Dewey, J.F. (eds) *Continental Transpressional and Transtensional Tectonics*. Geological Society of London, Special Publications 135, 1-14.
- Dixon, J.M. and Summers, J.M. 1985. Recent developments in centrifuge modelling of tectonic processes: equipment, model construction techniques and rheology of model materials. *Journal of Structural Geology* 7, 83-102.
- Dixon, J.M. and Summers, J.M. 1986. Another word on the rheology of silicone putty: Bingham. *Journal of Structural Geology* 8, 593-595.
- Donnadieu, F. and Merle, O. 1998. Experiments on the indentation process during crytpodome intrusions: New insights into Mount St. Helens deformation. *Geology* 26, 79-82.
- Druguet, E., Passchier, C.W., Carreras, J., Victor, P. and den Brok, S. 1997. Analysis of a complex high-strain zone at Cap de Creus, Spain. *Tectonophysics* 280, 31-45.
- Eisbacher, G.H. 1970. Deformation mechanisms of mylonitic rocks and fractured granulites in Cobequid Mountains, Nova Scotia, Canada. *Geological Society of America Bulletin* 81, 2009-2020.
- Echecopar, A. 1977. A plane kinematic model of progressive deformation in a polycrystalline aggregate. *Tectonophysics* 39, 121-139.
- Etheridge, M.A. and Hobbs, B.E. 1974. Chemical and deformation controls on recrystallisation of mica. *Contributions to Mineralogy and Petrology* 43, 111-124.
- Farver, J.R. and Yund, R.A. 1991. Oxygen diffusion in quartz: dependence on temperature and waterfugacity. *Chemical Geology* 90, 55-70.
- Ferguson, C.C. 1979. Rotations of elongated rigid particles in slow non-Newtonian flows. *Tectonophysics*, 60, 247-262.
- Fernandez, A., Feybesse, J.-L. and Mezure, J.-F. 1983. Theoretical and experimental study of fabrics developed by different shaped markers in two-dimensional simple shear. *Bulletin de la Societe Geologique de France* 3, 319-326.
- Fossen, H. and Tikoff, B. 1998. Extended models of transpression and transtension, and application to tectonic settings,. In: Holdsworth, R.E., Strachan, R.A., and Dewey, J.F. (eds) *Continental Transpressional and Transtensional Tectonics*. Geological Society of London, Special Publications 135, 15-33.
- Gay, N.C. 1968. Pure shear and simple shear deformation of inhomogeneous viscous fluids. 1. Theory. *Tectonophysics* 5, 211-234.
- Ghosh, S.K. and Ramberg, H. 1976. Reorientation of inclusions by combinations of pure and simple shear. *Tectonophysics* 34, 1-70.
- Ghosh S.K. and Sengupta S. 1973. Compression and simple shear of test models with rigid and deformable inclusions. *Tectonophysics* 17, 133-175.
- Giesekus, H. 1962. Strömungen mit konstantem Geschwindigkeitsgradienten und die Bewegung von darin suspendierten Teilchen, Teil II: Ebene Strömungen und eine experimentelle Anordnung zu ihrer Realisierung. *Rheologica Acta* 2, 112-122.

- Gohr, K., Pakula, T., Tsutsumi, K. and Schärtl, W. 1999. Dynamics of copolymer micelles in an entangled homopolymer matrix. *Macromolecules* 32, 7156-7165.
- Goodman, R.E. 1980. *Introduction to Rock Mechanics*. New York: John Wiley and Sons.
- Goodwin, L.B. and Wenk H.-R. 1995. Development of phyllonite from granodiorite: Mechanisms of grain-size reduction in the Santa Rosa mylonite zone, California. *Journal of Structural Geology* 17, 689-707.
- Griera, A. and Carreras, J. 1999. Mechanical instabilities associated to rod development: Preliminary results from analogue modelling. *Journal of Conference Abstracts* 4, 603.
- Grujic, D. 1993. The influence of initial fold geometry on Type 1 and Type 2 interference patterns: an experimental approach. *Journal of Structural Geology* 15, 293-307.
- Handy, M.R., Wissing, S.B. and Streit, L.E. 1999. Frictional-viscous flow in mylonite with varied biminerale composition and its effect on lithospheric strength. *Tectonophysics* 303, 175-191.
- Hanmer, S. 1984. The potential use of planar and elliptical structures as indicators of strain regime and kinematics of tectonic flow. *Geological Survey of Canada Paper* 84, 133-142.
- Hanmer, S. and Passchier, C.W. 1991. Shear sense indicators: a review. *Geological Survey of Canada Paper* 90, 1-71.
- Hobbs, B.E. and Ord, A. 1989. Numerical simulations of shear band formation in a frictional-dilatational material. *Ingenieur-Archiv* 59, 209-220.
- Hobbs, B.E., Means, W.D. and Williams, P.F. 1976. *An outline of structural geology*. Wiley, New York.
- Holdsworth, R.E., Butler, C.A. and Roberts, A.M. 1997. The recognition of reactivation during continental deformation. *Journal of Geological Society of London* 154, 73-78.
- Ildefonse, B. and Mancktelow, N.S. 1993. Deformation around rigid particles: the influence of slip at the particle/matrix interface. *Tectonophysics* 221, 345-359.
- Ildefonse, B., Sokoutis, D. and Mancktelow, N. S. 1992. Mechanical interactions between rigid particles in a deforming ductile matrix. Analogue experiments in simple shear flow. *Journal of Structural Geology* 14, 1253-1266.
- Imber, J., Holdsworth, R.E., Butler, C.A. and Lloyd, G.E. 1997. Fault-zone weakening processes along the reactivated Outer Hebrides Fault Zone, Scotland. *Journal of the Geological Society of London* 154, 105-109.
- Jeffery, G.B. 1922. The motion of ellipsoidal particles immersed in a viscous fluid. *Proceedings of the Royal Society of London, Series A* 102, 161-179.
- Jeffrey Giacomini, A. and Dealy, J.M. 1993. Large-amplitude oscillatory shear. In: *Techniques in rheological measurement*, edited by: Collyer, A. A., Chapman and Hall, Cambridge, 285-331.
- Jessell, M.W., Bons, P.D., Evans, L., Barr, T.D. and Stüwe, K. 2001. Elle: the numerical simulation of metamorphic and deformation microstructures. *Computers and Geosciences* 27, 17-30.
- Jezek, J., Saic, S., Segeth, K. and Schulman, K. 1999. Three-dimensional hydrodynamical modelling of viscous flow around a rotating ellipsoidal inclusion. *Computers and Geosciences* 25, 547-558.
- Jezek, J., Melka, R., Schulmann, K. and Venera, Z. 1994. The behaviour of rigid triaxial ellipsoidal particles in viscous flows - modeling of fabric evolution in a multiparticle system. *Tectonophysics* 229, 165-180.
- Jezek, J., Schulmann, K. and Segeth, K. 1996. Fabric evolution of rigid inclusions during mixed coaxial and simple shear flows. *Tectonophysics* 257, 203-221.
- Ji, S. and Martignole, J. 1994. Ductility of garnet as an indicator of extremely high temperature deformation. *Journal of Structural Geology* 16, 985-996.
- Jordan, P. 1988. The rheology of polymineralic rocks - an approach. *Geologische Rundschau* 77, 285-294.
- Kirby, S.H. and Kronenberg, A.K. 1987. Rheology of the lithosphere: selected topics. *Reviews of Geophysics* 25, 1219-1244.
- Kobberger, G. and Zulauf, G. 1995. Experimental folding and boudinage under pure constrictional conditions. *Journal of Structural Geology* 17, 1055-1063.

- Krabbendam, M. and Dewey, J.F. 1998. Exhumation of UHP rocks by transtension in the Western Gneiss Region, Scandinavian Caledonides. In: Holdsworth, R.E., Strachan, R.A. and Dewey, J.F. (eds) Continental Transpressional and Transtensional Tectonics. Geological Society of London, Special Publications 135, 159-181.
- Krantz, R.W. 1991. Measurements of friction coefficients and cohesion for faulting and fault reactivation in laboratory models using sand and sand mixtures. *Tectonophysics* 188, 203-207.
- Law, R.D., Knipe, R.J. and Dayan, H. 1984. Strain path partitioning within thrust sheets: microstructural and petrofabric evidence from the Moine thrust zone, NW Scotland. *Journal of Structural Geology* 6, 477-497.
- Lister, G.S. and Snoke, A.W. 1984. S-C Mylonites. *Journal of Structural Geology* 6, 617-638.
- Mares, V.M. and Kronenberg, A.K. 1993. Experimental deformation of muscovite. *Journal of Structural Geology* 15, 1061-1075.
- Masuda, T. and Mochizuki, S. 1989. Development of snowball structure: numerical simulation of inclusion trails during synkinematic porphyroblast growth in metamorphic rocks. *Tectonophysics* 170, 141-150.
- Masuda, T., Michibayashi, K. and Ohta., H. 1995. Shape preferred orientation of rigid particles in a viscous matrix: reevaluation to determine kinematic parameters of ductile deformation. *Journal of Structural Geology* 17, 115-129.
- McClay, K.R. 1976. The rheology of plasticine. *Tectonophysics* 33, T7-T15.
- Means, W.D., Hobbs, B.E., Lister, G.S. and Williams, P.F. 1980. Vorticity and non-coaxiality in progressive deformation. *Journal of Structural Geology* 2, 371-378.
- Means, W.D. 1981. The concept of steady-state foliation. *Tectonophysics* 78, 179-199.
- Nataf, H.-C., Hager, B.H. and Scott, R.F. 1984. Convection experiments in a centrifuge and the generation of plumes in a very viscous fluid. *Annales Geophysicae* 2, 303-310.
- Nelson, B.I. and Dealy, J.M. 1993. Dynamic mechanical analysis using complex waveforms. In: *Techniques in rheological measurement*, edited by Collyer, A.A., Chapman and Hall, Cambridge, 197-224.
- Oliver, D.H. and Goodge, J.W. 1996. Leucoxene fish as a micro-kinematic indicator. *Journal of Structural Geology* 18, 1493-1497.
- Ord, A. 1990. Mechanical controls on dilatant shear zones. In: Knipe, R.J. and Rutter, E.H. (eds) *Deformation mechanisms, Rheology and Tectonics*. Geological Society of London, Special Publication 54, 183-192.
- Ord, A. 1994. The fractal geometry of patterned structures in numerical models of rock deformation. In: *Fractals and dynamic systems*, ed. Kruhl, J.H., Springer Verlag, 131-155.
- Paciullo, F.V.P., Ribeiro, A. and Andreis, R.R. 1993. Reconstrução de uma bacia fragmentada: o caso do Ciclo Depositional Andrelândia. In: *Simpósio do Cráton do São Francisco 2*, Salvador, 1993, 224-226.
- Pakula, T., Geyler, S., Edling, T. and Boese, D. 1996. Relaxation and viscoelastic properties of complex polymer systems. *Rheologica Acta* 35, 631-644.
- Passchier, C.W. 1985. Water-deficient mylonite zones - An example from the Pyrenees. *Lithos* 18, 115-127.
- Passchier, C.W. 1986. Flow in natural shear zones - the consequences of spinning flow regimes. *Earth and Planetary Science Letters* 77, 70-80.
- Passchier, C.W. 1987. Stable positions of rigid objects in non-coaxial flow-a study in vorticity analysis. *Journal of Structural Geology* 16, 679-690.
- Passchier, C.W. 1991. The classification of dilatant flow types. *Journal of Structural Geology* 13, 101-104.
- Passchier, C.W. 1997. The fabric attractor. *Journal of Structural Geology* 19, 113-127.
- Passchier, C.W. 1998. Monoclinic model shear zones. *Journal of Structural Geology* 20, 1121-1137.
- Passchier, C.W. and Simpson, C. 1986. Porphyroblast systems as kinematic indicators. *Journal of Structural Geology* 15, 895-910.
- Passchier C.W. and Sokoutis, D. 1993. Experimental modeling of mantled porphyroclasts. *Journal of Structural Geology* 15, 895-909.



- Passchier, C.W. and Trouw, R.A.J. 1996. *Microtectonics*. Springer Verlag, Berlin, Heidelberg.
- Passchier, C.W., ten Brink, C.E. Bons, P.D. and Sokoutis, D. 1993. Delta-objects as a gauge for stress sensitivity of strain rate in mylonites. *Earth and Planetary Science Letters* 120, 239-245.
- Paterson, M.S. and Olgaard, D.L. 2000. Rock deformation tests to large shear strains in torsion. *Journal of Structural Geology* 22, 1341-1358.
- Pennacchioni, G., Fasolo, L., Morandi Cecchi, M. and Salasnich, L. 2000. Finite-element modelling of simple shear flow around a circular rigid particle. *Journal of Structural Geology* 22, 683-692.
- Pfiffner, O.A. and Ramsey, J.G. 1982. Constraints on geological strain rates: arguments from finite strain states of naturally deformed rocks. *Journal of Geophysical Research* 87, 311-321.
- Poirier, J.P. 1980. Shear localisation and shear instability in materials in the ductile field. *Journal of Structural Geology* 2, 135-142.
- Poirier, J.P. 1985. *Creep of Crystals*. Cambridge University Press.
- Price, G.P. and Torok, P.A. 1989. A new simple shear deformation apparatus for rocks and soils. *Tectonophysics* 158, 291-309.
- Ramberg, H. 1955. Natural and experimental boudinage and pinch-and-swell structures. *Journal of Geology* 63, 512-526.
- Ramberg, H. 1975. Particle paths, displacement and progressive strain applicable to rocks. *Tectonophysics* 28, 1-37.
- Ramsay, J.G. 1962. The geometry and mechanics of formation of 'similar' type folds. *Journal of Geology* 70, 309-327.
- Ramsay, J.G. 1980. Shear zone geometry: a review. *Journal of Structural Geology* 2, 83-101.
- Ribeiro, A., Trouw, R.A.J., Andreis, R.R. Paciullo, F.V.P. and Valença, J.G. 1995. Evolução das bacias Proterozóicas e o termo-tectonismo Brasileiro na margem sul do Cráton do São Francisco. *Revista Brasileira de Geociências* 25, 235-248.
- Robertson, C.R. and Acrivos, A. 1970. Low Reynolds number shear flow past a rotating circular cylinder. Part 1. Momentum transfer. *Journal of Fluid Mechanics* 40, 68-704.
- Robin, P.-Y.F. and Cruden, A.R. 1994. Strain and vorticity patterns in ideally ductile transpression zones. *Journal of Structural Geology* 16, 447-466.
- Roman-Berdiel, T., Gapai, D. and Brun, J. P. 1995. Analogue models of laccolith formation. *Journal of Structural Geology* 17, 1337-1346.
- Sanderson, D.J. and Marchini, W.R.D. 1984. Transpression. *Journal of Structural Geology* 6, 449-458.
- Sibson, R.H. 1977. Fault rocks and fault mechanisms. *Journal of the Geological Society of London* 133, 191-213.
- Simpson, C. 1984. Borrego Springs-Santa Rosa mylonite zone: a late cretaceous west-directed thrust in Southern California. *Geology* 12, 1-11.
- Simpson, C. and De Paor, D.G. 1993. Strain and kinematic analysis in general shear zones. *Journal of Structural Geology* 15, 1-20.
- Simpson, C. and Schmid, S.M. 1983. An evaluation of criteria to deduce the sense of movement in sheared rocks. *Geological Society of America Bulletin* 94, 1281-1288.
- Simpson, C. and Wintch, R.P. 1989. Evidence for deformation-induced K-feldspar replacement by myrmekite. *Journal of Metamorphic Geology* 7, 261-275.
- Sokoutis, D. 1987. Finite strain effects in experimental mullions. *Journal of Structural Geology* 9, 233-242.
- Ten Brink, C.E. 1996. Development of porphyroclast geometries during non-coaxial flow [Ph.D. thesis]. *Geologica Ultraiectina* 142 Utrecht University.
- Tikoff, B. and Greene, D. 1997. Stretching lineations in transpressional shear zones: an example from the Sierra Nevada Batholith, California. *Journal of Structural Geology* 19, 29-39.
- Tikoff, B. and Fossen, H. 1995. The limitations of three-dimensional kinematic vorticity analysis. *Journal of Structural Geology* 17, 1771-1784.
- Treagus, S.H. and Sokoutis, D. 1992. Laboratory modelling of strain variation across rheological boundaries. *Journal of Structural Geology* 14, 405-424.

- Trouw, R.A.J. and Passchier, C.W. 1997. A closer look at mica fish and similar structures in other minerals. VI Simpósio Nacional de Estudos Tectônicos, Brasília, 277-280.
- Trouw, R.A.J., Ribeiro, A. and Paciullo, F.V. 1983. Geologia estrutural dos grupos São João del Rei, Carrancas e Andrelândia, Sul de Minas Gerais. An. Acad. Brasil Ciênc. 55, 71-85.
- Tullis, J. and Yund, R. A. 1991. Diffusion creep in feldspar aggregates: experimental evidence. Journal of Structural Geology 13, 987-1000.
- Twiss, R.J. and Moores, E.M. 1992. Structural Geology. W.H. Freeman and Company, New York.
- Wallis, S. 1995. Vorticity analysis and recognition of ductile extension in the Sanbagawa belt, SW Japan. Journal of Structural Geology 17, 1077-1093.
- Weijermars, R. 1986. Flow behaviour and physical chemistry of bouncing putties and related polymers in view of tectonic laboratory applications. Tectonophysics 124, 325-358.
- Weijermars, R. 1991. Progressive deformation in anisotropic rocks. Journal of Structural Geology 14, 723-742.
- Weijermars, R. 1993. Pulsating strains. Tectonophysics 220, 51-67.
- Weijermars, R. 1997. Pulsating oblate and prolate three-dimensional strains. Mathematical Geology 29, 17-41.
- Weijermars, R. 1998. Taylor-mill analogs for patterns of flow and deformation in rocks. Journal of Structural Geology 20, 77-92.
- Wenk, H.-R. and Pannetier, J. 1990. Texture development in deformed granodiorites from the Santa Rosa mylonite zone, southern California. Journal of Structural Geology 12, 177-184.
- White, S.H., Burrows, S.E., Carreras, J. Shaw, N.D. and Humphreys, F.J. 1980. On mylonites in ductile shear zones. Journal of Structural Geology 2, 175-187.
- Whitehead, J.A. and Luther, D.S. 1975. Dynamics of laboratory diapir and plume models. Journal of Geophysical Research 80, 705-717.
- Winter, H. H., Baumgärtel, M. and Soskey, P.R. 1993. A parsimonious model for viscoelastic liquids and solids. In: Techniques in rheological measurement., edited by Collyer, A.A., Chapman and Hall, Cambridge, 123-160.
- Zhang, Y. Hobbs, B.E., Ord, A. and Mühlhaus, H.B. 1996a. Computer simulation of single layer buckling. Journal of Structural Geology 18, 643-655.
- Zhang, Y. Jessell, M.W. and Hobbs, B.E. 1996b. Experimental and numerical studies of the accommodation of strain incompatibility on the grain scale. Journal of Structural Geology 18, 451-460.
- Zhang, Y. and Wilson, C.J.L. 1997. Lattice rotation in polycrystalline aggregates and single crystals with one slip system: a numerical and experimental approach. Journal of Structural Geology 19, 875-885.
- Zhang, Y. Mancktelow, N.S., Hobbs, B.E., Ord, A. and Mühlhaus, H.B. 2000. Numerical modelling of single-layer folding: clarification of an issue regarding the possible effect of computer codes and the influence of initial irregularities. Journal of Structural Geology 22, 1511-1522.

# Zusammenfassung

In der vorliegenden Arbeit wird die Verformung von Gesteinen in Scherzonen beschrieben. Ein Großteil der Verformung in der Erdkruste findet innerhalb solcher mikrometer- bis kilometerbreiten Zonen statt. Die allgemeine Rheologie dieser Scherzonen hängt von der Tiefe ab, in der sie sich befinden. Befindet sich eine Scherzone weniger als in 10 bis 20 Kilometer Tiefe, so verhält sie sich spröde, in einer größeren Tiefe jedoch duktil.

Ein Mylonit ist ein duktil verformtes Gestein mit einer deutlich ausgebildeten Foliation und meist auch Lineation. Häufig sind in Myloniten Porphyroklasten vorzufinden. Diese sind Rückstände von relativ harten Mineralen, die mindestens eine Größenordnung größer als die Körner der umgebenden Matrix sind. Glimmerfische, die aus linsen- bzw. parallelogrammförmigen Glimmerkristallen bestehen, stellen eine bestimmte Art von Porphyroklasten dar. Solche Glimmerfische werden genutzt, um die Bewegungsrichtung innerhalb von Scherzonen zu ermitteln. Hierzu können der relative Versatz der "Schwänze" der Glimmerfische, deren Orientierung im Bezug auf die Foliation, sowie ihre Assymetrie zur Hilfe genommen werden. Aufgrund dieser Eigenschaften sind Glimmerfische zuverlässige Indikatoren für die Bewegungsrichtung in Scherzonen. In dieser Arbeit wird die Entstehung von Glimmerfischen beschrieben und untersucht was diese Strukturen über die Verteilung von Verformung in Scherzonen aussagen.

In Kapitel 2 werden die Mikrostrukturen von natürlichen Glimmerfischen in Dünnschliffen beschrieben. Es werden die möglichen Verformungsmechanismen untersucht, die zur heutigen Form der Glimmerfische geführt haben. Zusätzlich werden Glimmerfische mit anderen ähnlich geformten Mineralen verglichen, wie z.B. Turmalin. Mögliche Verformungsmechanismen, die zu den verschiedenen Mineralfischen führen, können in zwei Gruppen eingeteilt werden: (a) Mechanismen, die direkt die Form eines Kristalls verändern, und (b) Mechanismen, die ein großes Mineral in mehrere kleine, fischförmige Kristalle aufspalten. Zu (a) gehören: intrakristalline Verformung, Kristallrotation, Biegung und Faltung, Drucklösung in Kombination mit Ausfällung und dynamische Rekristallisation am Rande des Kristalles. Welche dieser Mechanismen zur Form des "Fisches" beigetragen haben, hängt von den Eigenschaften des jeweiligen Minerals ab. Einige Minerale können nur bedingt eine Fischform ausbilden, weil sie dazu tendieren vollkommen zu rekristallisieren. Aufspaltung eines großen Kristalls erfolgt, indem sich ein Bruch entlang der basalen Kristallflächen entwickelt und Scherung entlang dieser Flächen stattfindet. Eine andere Möglichkeit ist die Faltung eines Kristalls und Bruch entlang der Faltenachsenfläche, wiederum gefolgt von Scherung entlang der entstandenen Bruchfläche. Diese Mechanismen basieren auf die inhomogene Deformationsverteilung in der direkten Umgebung des Kristalls. Ein Fragment kann nur entlang eines Kristalls transportiert werden, wenn sich zusätzlich eine Mikroscherzone entwickelt. Die assymetrische Form und Orientierung im Bezug auf die Foliation sind gemeinsame Merkmale der verschiedenen Mineralfische.

In Kapitel 3 bis 5 wird auf Analogexperimente eingegangen. In Kapitel 3 wird ein neues Verformungsgerät vorgestellt. Mit diesem Gerät können verschiedene Kombinationen von einfacher und reiner Scherung modelliert werden. In diesem Gerät können Materialien verformt werden, die ähnliche Eigenschaften wie Gesteine haben. Jedoch müssen sie nicht wie Gesteine hohen Druck und Temperatur ausgesetzt werden, um in kurzen Zeiträumen deformiert zu werden. Ein Beispiel für ein solches Material sind Polymere. In Kapitel 4 wird das rheologische Verhalten von mehreren Polymeren und verwandten Materialien beschrieben, welche mit dem beschriebenen Verformungsgerät benutzt werden können. Die Relevanz von Polymeren als Gesteinsanaloge wird diskutiert.

In Kapitel 5 werden Experimente mit fischförmigen Objekten in zwei verschiedenen Matrixmaterialien beschrieben. Das eine ist PDMS, ein homogenes, Newtonianisch viskoses Polymer, und das andere Tapioca Perlen. Diese Tapioca Perlen sind runde Körner mit einem Durchmesser von ungefähr 2 mm und weisen ein Mohr-Coulomb Verhalten auf. Die fischförmigen Objekte, die als Analoge für Glimmerfische dienen, sind nicht verformbar. Die Rotation von Objekten in Experimenten mit PDMS stimmt gut mit der theoretischen Rotationsrate für ellipsenförmige Objekte in einem homogenen, Newtonianischen Material überein. In einer Matrix von Tapioca Perlen nehmen die Objekte eine stabile Lage ein. Diese Orientierung ist vergleichbar mit der Orientierung von natürlichen Glimmer- und Turmalinfischen. Die Verformung in der Matrix von Tapioca Perlen ist nicht homogen, sondern konzentriert auf dünne Scherzonen. Diese Ergebnisse implizieren, daß die Verformung in natürlichen Gesteinen wahrscheinlich auch in dünnen Scherzonen konzentriert und nicht homogen verteilt ist.

In Kapitel 6 werden Computersimulationen beschrieben, mit denen der Einfluß der rheologischen Eigenschaften einer Matrix auf die Rotation von Objekten und Verteilung von Deformation untersucht wird. Mit diesen Experimenten wird gezeigt, daß die stabile Orientierung von Glimmerfischen nicht mit Verformung in einem homogenen, nicht linearen viskosen Material erklärt werden kann. Eine solche homogene, nicht lineare Rheologie wird jedoch im Allgemeinen für die Erdkruste angenommen. Die stabile Orientierung eines Objektes kann mit der Anwesenheit von weicheren Lagen in der Matrix erklärt werden.

Kapitel 7 beinhaltet die Schlußfolgerungen, die aus den beschriebenen Ergebnissen der Arbeit folgen. Zusätzlich werden Möglichkeiten zukünftige Untersuchungen gegeben.

## Samenvatting

In dit proefschrift wordt ingegaan op de vervorming van gesteentes in schuifzones. Deze enkele micrometer tot meerdere kilometers brede schuifzones zijn voor een groot deel verantwoordelijk voor de vervorming in de aardkorst. Het vervormingsgedrag van gesteentes in zulke schuifzones hangt van de diepte van de zone af. In ondiep gesitueerde schuifzones (minder dan 10 tot 20 kilometer) vertoont het gesteente bros gedrag, in diepere delen van de aardkorst ductiel- of vloeigedrag.

Een myloniet is een gesteente met duidelijke foliatie en meestal ook lineatie, dat vervormd is door ductiel gedrag. In mylonieten zijn meestal 'porfieroklasten' aanwezig. Dit zijn overblijfselen van relatief harde mineralen, die minimaal een orde van grootte groter zijn dan de korrels in de matrix. 'Mica vissen', lens- of parallelogramvormige mica kristallen, zijn een speciaal soort porfieroclast. Deze mica vissen worden vaak gebruikt om de bewegingsrichting in een schuif-zone te bepalen. Dit wordt gedaan met het verzet van de staarten van de mica vis aan beide zijden van de vis, de oriëntatie van de vis ten opzichte van de foliatie en met de asymmetrische vorm van de vis. Deze kenmerken maken van een mica vis een zeer betrouwbare indicator voor de bewegingsrichting. In dit proefschrift wordt beschreven hoe mica vissen ontstaan, en wat deze structuren vertellen over de richting en de verdeling van de vervorming in de schuifzone.

In hoofdstuk 2 worden de microstructuren van natuurlijke mica vissen in dunne doorsnedes beschreven. Er is gekeken welke vervormingsmechanismen mogelijk hebben bijgedragen aan de huidige vorm van de mica vissen. Bovendien worden mica vissen vergeleken met gelijkvormige structuren in andere mineralen. Mogelijke mechanismen die de vorm van de verschillende mineraalvissen veroorzaken zijn verdeeld in twee groepen: mechanismen die de vorm van een kristal veranderen en mechanismen die een groter kristal opsplitsen in verschillende kleinere. Tot de eerste groep behoren: intrakristallijne vervorming, rotatie van het kristal, ombuigen en plooien, dynamische rekristallisatie aan de rand van het kristal, en drukoplossing vergezeld van plaatselijke groei van het kristal. Welke van deze mechanismen bijgedragen heeft tot de vorm van de 'vis' hangt van de eigenschappen van het desbetreffende mineraal af. Voor enkele mineralen lijkt de visvorm een tijdelijk situatie, voordat het kristal volkomen gerekristalliseerd is. Opsplitsen van een groter kristal kan doordat een breuk zich ontwikkelt parallel aan de basale kristalvlakken, gevolgd door beweging van de twee ontstane delen langs elkaar. Een andere mogelijkheid is dat het kristal plooit en vervolgens afbreekt langs het assenvlak, wederom gevolgd door beweging van beide delen van het kristal langs elkaar. Deze mechanismen zijn gebaseerd op een inhomogene verdeling van de vervorming rond het kristal. Alleen als er een micro-schuifzone ontwikkeld is aan de rand van de mica vis kan een fragment

langs deze grens worden getransporteerd. De verschillende 'mineraal vissen' hebben met elkaar gemeen dat ze allemaal een asymmetrische vorm hebben en een vergelijkbare oriëntatie ten opzichte van de foliatie. Door deze eigenschappen zijn al deze structuren uitstekende indicatoren voor de bewegingsrichting in het gesteente.

Hoofdstuk 3 tot en met 5 zijn gewijd aan analoog experimenten. In hoofdstuk 3 wordt een nieuw vervormingsapparaat voorgesteld, dat ontwikkeld is in het kader van dit onderzoek. Met dit apparaat kunnen verschillende soorten vervorming worden gemodelleerd, variërend van samendrukken in een richting (pure shear) tot eenvoudige schuifbewegingen (simple shear) en combinaties van beide bewegingen. Materialen die vervormd kunnen worden met dit apparaat zijn zogenaamde gesteenteanalogen. Deze materialen hebben vergelijkbare eigenschappen als gesteentes bij hogere temperatuur en druk, maar zijn minder sterk, zodat experimenten in relatief korte tijd kunnen worden gedaan. Polymeren worden vaak gebruikt als gesteenteanaloog. In hoofdstuk 4 wordt het gedrag van enkele polymeren beschreven, die geschikt zijn om te gebruiken in combinatie met het apparaat uit hoofdstuk 3. Daarnaast wordt het gebruik van polymeren als gesteenteanaloog bediscussieerd.

In hoofdstuk 5 worden analoog experimenten beschreven met visvormige objecten in twee verschillende matrix materialen. Het eerste is PDMS, een homogeen Newtoniaans-visceus polymeer, en het tweede tapioca parels, ronde korrels met een doorsnede van ongeveer 2 mm met Mohr-Coulomb vervormingsgedrag. De visvormige objecten, die als analoog voor de mica vissen dienen, zijn niet vervormbaar. De rotatie van de objecten in experimenten met PDMS komen zeer goed overeen met de voorspelde rotatie volgens de theorie voor beweging van ellipsvormige objecten in een Newtoniaanse vloeistof. In een matrix van tapioca parels hebben de objecten een stabiele oriëntatie. Deze oriëntatie komt overeen met de data van natuurlijke mica- en toermalijn vissen. De vervorming in een matrix van tapioca parels is niet homogeen, maar geconcentreerd in dunne schuifzones. Deze resultaten impliceren dat de vervorming in natuurlijke gesteentes waarschijnlijk ook geconcentreerd is in dunne zones, en niet homogeen verdeeld over de matrix.

In hoofdstuk 6 zijn computereperimenten beschreven, die de rol van het vervormingsgedrag van de matrix en van inhomogene matrix eigenschappen op de rotatie van objecten en op de verdeling van de vervorming laten zien. In deze experimenten wordt duidelijk dat homogeen niet-lineair vloeigedrag, wat meestal wordt aangenomen voor de vervorming in de aardkorst, niet voldoende is om de oriëntatie van mica vissen in mylonieten te verklaren. De aanwezigheid van zachte lagen in de matrix of rondom het object kunnen een verklaring voor de stabiele oriëntatie van de mica vissen zijn.

In hoofdstuk 7 worden de belangrijkste conclusies gegeven die uit de beschreven resultaten volgen. Daarnaast worden mogelijkheden voor toekomstig onderzoek gegeven.

## Acknowledgements

On a warm summer day for 3 1/2 years, I bought a train ticket to a, for me, unknown destination somewhere in Germany: Mainz. Now, I have lived in this nice city along the Rhine for almost three years, wrote a thesis, and had I great time here. I want to thank everybody who helped and encouraged me to do research and to complete my thesis in this form.

First of all I want to thank my supervisors. It was a pleasure working with them and I learned a lot. I would also like to thank them for all the discussions and all their ideas.

I particularly want to thank my roommate for everything. The last three years would not have been the same without her. I would also like to thank all the other people at the Institute for Geosciences in Mainz for being great people and a nice working group. The students of the Graduierten Kolleg and associated students are thanked for the discussions and for all the good times we had. These people made me feel welcome when I arrived in Mainz.

Part of this project was made possible by a visit to Rio de Janeiro. I want to thank the people there for their support during this visit and also for providing several samples of mineral fish. The help with the microprobe investigations and during the development of the deformation apparatus is greatly acknowledged. Reviews helped to improve the manuscript for chapter 3. Discussions with several people about polymers are greatly acknowledged. Thanks to all the people for all the support and discussions.

I have always been given support by my friends in the Netherlands, thanks guys.

Finally I want to thank my family for all their support and love, and especially one person for his understanding and his constant support and love over the last three years.

This research was funded by the German Research foundations (GRK 392/1) and DAAD (415-br-probal).





## Curriculum Vitae

- Place and date of birth: Warnsveld, Netherlands, June 24, 1975
- Secondary education: 1987-1993: V.W.O. (Gymnasium) at the Isendoorn College, Warnsveld
- University education: 1993-1998: Geology , Institute of Earth sciences, Utrecht University. Main Subjects: Structural Geology and Earth Materials
- Postgradual experience: 1998-2000: PhD-research as "Graduierten Kolleg" student at the Tectonophysics Group, Institute of Geosciences, University of Mainz